Charles University in Prague

Faculty of Mathematics and Physics

DOCTORAL THESIS

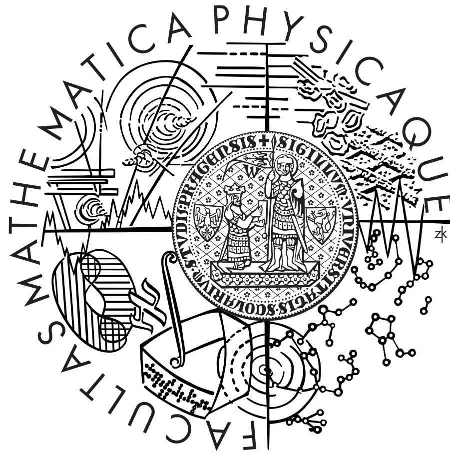

Václav Dědič

Influence of Deep Levels on Charge Transport in CdTe and CdZnTe

Institute of Physics of Charles University

Supervisor of the doctoral thesis: Prof. Ing. Jan Franc, DrSc.

Study programme: Physics

Specialization: Quantum Optics and Optoelectronics

Prague 2014

At this place I would like to thank all the people who were supporting me through my doctoral study. Without these people it would have been extremely difficult to finish my studies and this thesis as it is.

People from the Division of Semiconductors and Semiconductor Optoelectronics at Institute of Physics of Charles University formed a very nice and friendly working environment.

Foremost, I would like to thank my supervisor Prof. Jan Franc for his great guidance during the whole period of my master and doctoral studies. I appreciate much his suggestions, patience and knowledge during our frequent discussions that helped me in all the time during the research and writing this thesis. Special thanks belong to him for an encouragement to spend a part of my study abroad that was a great experience.

Beside my supervisor, I would like to acknowledge my advisor Assoc. Prof. Roman Grill and Assoc. Prof. Pavel Hlídek for their ideas and discussions about theoretical and experimental issues.

I thank Dr. Jan Kubát and Assoc. Prof. Hassan Elhadidy for close cooperation during the beginning of my doctoral study and for sharing their experiences. I also thank Assoc. Prof. Eduard Belas and Assoc. Prof. Pavel Moravec for sharing their experiences about the sample preparation.

I would like to acknowledge Assoc. Prof. Petr Praus, Mr. Jan Ulrych and Mr. Roman Šilha for their technical support. For their friendship and occasional assistance I also thank to my colleagues Jakub Zázvorka, Lukáš Šedivý and Jakub Pekárek.

Special thanks belong to Prof. Paul J. Sellin, Dr. Annika Lohstroh and Dr. Veeramani Perumal for their support during my stay at the University of Surrey.

I would like to thank people from Brookhaven National Laboratory, especially Dr. Ralph B. James, Dr. Aleksey Bolotnikov, Dr. Zheng Li, Giuseppe Camarda, Dr. Utpal N. Roy, Dr. Ge Yang, Dr. Anwar Hossain and Patty Lee for their support and kindness during my long term abroad stay.

I am very thankful to my mother, father and Lucie for their patience and encouragement during my studies.

I declare that I carried out this doctoral thesis independently, and only with the cited sources, literature and other professional sources.

I understand that my work relates to the rights and obligations under the Act No. 121/2000 Coll., the Copyright Act, as amended, in particular the fact that the Charles University in Prague has the right to conclude a license agreement on the use of this work as a school work pursuant to Section 60 paragraph 1 of the Copyright Act.

In Prague, date 27.3.2014 Václav Dědič

Název práce: Vliv hlubokých hladin na transport náboje v CdTe a CdZnTe

Autor: Václav Dědič

Katedra: Fyzikální ústav Univerzity Karlovy

Vedoucí disertační práce: prof. Ing. Jan Franc, DrSc., Fyzikální ústav Univerzity Karlovy (franc@karlov.mff.cuni.cz)

Abstrakt: CdTe a CdZnTe jsou perspektivní materiály pro detektory Rentgenového a gama záření pracující za pokojové teploty. Akumulace prostorového náboje na hlubokých energetických hladinách způsobená zahnutím pásu u kontaktu s Schottkyho bariérou a zachycením fotogenerovaného náboje může vést k časově závislé změně efektivity sběru náboje v CdTe a CdZnTe detektorech známé jako polarizační jev. Tato práce se zabývá především studiem profilů elektrických polí v detektorech za tmy a za vysokých fotonových toků simulujících provoz detektoru pomocí metody zkřížených polarizátorů využívající elektro-optický (Pockelsův) jev. Dále se práce zabývá studiem hlubokých hladin zodpovědných za polarizaci a vlivem kontaktních kovů na akumulaci náboje. Některé experimentální výsledky jsou podpořeny teoretickými simulacemi. Měření byla provedena na třech sadách vzorků opatřených různými kontaktními kovy (Au, In) připravených ze tří různých n-typových materiálů CdTe a CdZnTe. Energetické hladiny byly detekovány za použití metod založených na Pockelsově jevu a měření vybíjecích proudů. Detailní studium vnitřních elektrických polí ukazuje na zásadní vliv energetických hladin poblíž středu zakázaného pásu souvisejících s krystalovými poruchami a kontaktních kovů na polarizaci v polovodičových detektorech za vysokých toků záření.

Klíčová slova: CdTe, CdZnTe, polovodičové detektory Rentgenova a gama záření, polarizace v detektoru, hluboké energetické hladiny, kontaktní kovy, Pockelsův jev

Title: Influence of Deep Levels on Charge Transport in CdTe and CdZnTe

Author: Václav Dědič

Department: Institute of Physics of Charles University

Supervisor: prof. Ing. Jan Franc, DrSc., Institute of Physics of Charles University (franc@karlov.mff.cuni.cz)

Abstract: CdTe and CdZnTe are promising materials for room temperature semiconductor X-ray and gamma ray detectors. The accumulation of a space charge at deep energy levels due to a band bending at contacts with Schottky barriers and due to trapped photogenerated charge may result in time dependent change of charge collection efficiency in CdTe and CdZnTe detectors known as polarization effect. This thesis is mainly focused on a study of electric field profiles in detectors under dark and high photon flux conditions simulating detector operation using crossed polarizers technique exploiting the electro-optic (Pockels) effect. It also deals with a study of deep levels responsible for the polarization and influence of contact metals on charge accumulation. Several experimental results are supported by theoretical simulations. The measurements were performed on three sets of samples equipped with different contact metals (Au, In) cut from three different n-type CdTe and CdZnTe materials. Energy levels were detected using methods based on the Pockels effect and discharge current measurements. Detailed study of internal electric field profiles has revealed a fundamental influence of near midgap energy levels related to crystal defects and contact metals on the polarization in semiconductor detectors under high radiation fluxes.

Keywords: CdTe, CdZnTe, semiconductor X-ray and gamma-ray detectors, polarization in detector, deep energy levels, contact metals, Pockels effect

Table of Contents

1 Introduction **1**
1.1 Motivation . . . 1
1.2 Basic properties of CdTe and $Cd_xZn_{1-x}Te$ . . . 2
1.3 Semiconductor radiation detector . . . 4
1.4 Crystal defects and energy levels . . . 5
1.4.1 Undoped (CdZn)Te . . . 5
1.4.2 Doped (CdZn)Te . . . 6
1.4.3 Compensation of shallow defects . . . 6
1.5 The goal of this thesis . . . 9

2 Theory **10**
2.1 Hall-Shockley-Read model . . . 10
2.2 Metal-Semiconductor interface (contacts) . . . 12
2.3 Poisson's equation . . . 13
2.4 Drift-diffusion equation . . . 14
2.5 Processes in the sample after illumination . . . 15
2.6 Numerical simulations . . . 16
2.7 Polarization in detectors . . . 19
2.8 Electro-optic effect and crossed polarizers technique . . . 20
2.8.1 Wave retarder between two crossed linear polarizers . . . 20
2.8.2 Pockels effect . . . 21
2.8.3 Electric field reconstruction . . . 27
2.9 Thermal emission of charge carriers from defect levels into bands . 28
2.9.1 De-trapping and the electric field . . . 29
2.9.2 Deep level parameters . . . 30

3 Experimental **32**
3.1 Pockels effect . . . 32
3.1.1 Advanced setup . . . 35
3.1.2 Data acquisition and analysis . . . 36
3.2 Photoconductivity measurements . . . 39
3.2.1 Experimental setup . . . 40

3.2.2 Lux-Ampere characteristics 41
3.3 Discharge current measurements 42
3.3.1 Experimental setup 42
3.3.2 Analysis 43
3.4 Samples 44
3.4.1 VGF CdTe:In - samples no.1 & 2 44
3.4.2 HPB CdZnTe - samples no.3 & 4 44
3.4.3 VGF CdZnTe - sample no.5 45
3.5 Discussion: Pockels effect measurements 46

4 Results I: Pockels effect measurements 48
4.1 Basic measurements 48
4.1.1 Au/CdTe/In structure (Sample no.1) 48
4.2 Temporal and temperature evolution of the electric field 51
4.2.1 Au/CdTe/In structure (Sample no.1) 51
4.2.2 Polarization study in n-type CdZnTe (Sample no.5) 56
4.2.3 Au/CdZnTe/In structure (Sample no.3) 61
4.2.4 Comparison of steady state electric field profiles 62
4.3 X-ray and laser irradiation 62
4.3.1 Au/CdTe/In structure (Sample no.1 & 2) 62
4.3.2 Au/CdZnTe/In structure (Sample no.3) 67
4.4 Laser excitation with IR spectral scanning 73
4.4.1 Au/CdZnTe/In structure (Sample no.3) 74
4.4.2 Au/CdTe/In structure (Sample no.1) 78

5 Results II: Discharge current measurements 82
5.1 N-type CdZnTe (sample no.5) 82
5.2 Semiinsulating CdZnTe (samples no.3 & 4) 84
5.3 Discussion: capture cross-sections 85

6 Results III: Summary of observed energy levels 87

7 Summary and conclusions 90

References 92

Appendix 100
A.1 List of tables 100
A.2 List of figures 100
A.3 List of abbreviations 102

Chapter 1

Introduction

1.1 Motivation

At the present time there is an increased need of large area radiation detectors in medical diagnostics and in non-destructive testing. These applications require detector materials with high absorption, efficiency, good spatial resolution and stable performance under high flux X-ray radiation.

CdTe and CdZnTe compounds are materials of choice for room temperature semiconductor high energy X-ray and gamma ray detectors due to their high atomic number Z and bandgap energy E_g. A low dark current and high mobility-lifetime product ($\mu\tau$) of charge carriers are necessary prerequisites of a high quality radiation detector. The required parameters of these materials can be achieved at room temperature. High resistivity material can be relatively easily prepared by suitable doping of the material with impurities, that form deep energy levels that pin the Fermi level E_f close to the midgap [1]. However, the deep level acts also as a recombination or trap center. It usually decreases the lifetime of carriers and can lead to their accumulation, which finally results in the deformation of the internal electric field.

The accumulation of space charge at deep levels may result in time dependent change of charge collection efficiency in CdTe and CdZnTe X-ray and gamma ray semiconductor detectors known as polarization that has been in the focus of research for a long time [2–7]. It has been recently reviewed in ref. [8]. This effect is a result of screening of the electric field by space charge formed due to a band bending at contacts with Schottky barriers and is therefore observed even without any radiation. In order to understand the phenomenon it is necessary to determine the levels at which carriers can be trapped and form the space charge. Most of the work published on polarization so far was done on p-type CdTe commercial detector material doped with Cl fabricated by Acrorad Japan [6, 9, 10], where In is applied as the hole blocking Schottky barrier contact and it decreases this way the dark current. The ionization of the deep acceptor by

hole de-trapping from a deep acceptor level at ~ 0.6 eV above the valence band and induced space charge buildup was reported as a responsible mechanism for polarization phenomena in p-type CdTe material [11].

In CdZnTe the intrinsic resistivity can achieve $\sim 10^{10}$ Ωcm due to a higher bandgap energy. Application of blocking Schottky contacts is not necessary. The polarization due to band banding is therefore in CdZnTe present less frequently. Nevertheless it was observed that relatively small decrease of temperature can lead to a transition of an originally ohmic contact to a Schottky one and this results to a strong deformation of the internal electric field [12].

Another reasons of polarization are the high flux[1] conditions during the operation of the detector when the photogenerated space charge is accumulated at deep levels. This effect can be called radiation induced polarization. Polarization at high fluxes has come to the focus of interest relatively recently [13–17]. Bale and Szeles [17] revealed the nature of polarization of CdZnTe at high fluxes of X-ray radiation. Prokesch et al. [16] studied the possibility to optically manipulate the occupation of deep levels in semi-insulating CdZnTe using an IR LED diode in order to control the delayed temporal response of high-flux X-ray detectors to changing photon fluxes. A postgrowth manipulation of the internal electric field using subbandgap illumination was studied in [13] using several types of LED diodes. No information about the energy of the levels at which the carriers are trapped at high fluxes is available so far.

Study of deep levels and their influence on polarization in detectors is thus highly relevant in order to increase the quality of detector materials by choosing proper dopant, processing conditions optimizing crystal growth and post-growth conditions. It is obvious that one of the important issues for the CdTe and CdZnTe sensors is the optimization of their electrodes because the internal electric field in the detector is affected by the band bending at metal-semiconductor (M-S) interface.

To summarize, there is a practical importance to increase the understanding of fundamentals of polarization phenomena in (CdZn)Te. Specifically it is desirable to find out which energy levels can accumulate space charge in the temperature range at which normally (CdZn)Te detectors are operated (~ 300 K) and to study the role of contact metals on the band bending at M-S interface.

1.2 Basic properties of CdTe and $Cd_xZn_{1-x}Te$

CdTe is II-VI direct bandgap semiconductor. It has been developed as a detector material through 35 years [18]. Ternary compound $Cd_xZn_{1-x}Te$ has been used

[1] The term "high flux" signifies a flux that changes the quasi-Fermi levels and the electric field profiles, while the "low flux" does not.

as a substrate for infrared HgCdTe detectors [19]. The first study on CdZnTe detector material was published in 1992 ([20] and [21]). It is possible to prepare not-intentionally doped $Cd_{0.9}Zn_{0.1}Te$ with the resistivity up to 10^{11} Ωcm. The fundamental material properties of CdZnTe and CdTe are shown in table 1.1 and the dependence of absorption coefficient α of CdTe on photon energy close to the bandgap energy E_g is presented on fig.1.1 [22].

In addition to the preparation of radiation detectors, CdTe based compounds are widely used in a number of other applications. CdTe is important material in photovoltaics. The recent values (2013) of the efficiency of CdTe thin-film solar cells are 16% for industrial modules and efficiency 19.6% has been achieved under laboratory conditions [23]. (CdZn)Te shows linear electro-optic (Pockels) effect due to its zinc-blende crystalline structure (with $\bar{4}3m$ symmetry) [24] and it is commonly used for infra red phase modulation in electro-optic devices (e.g. [25] and [26]). This property is exploited to study the polarization in detectors in this thesis.

Material	$Cd_{0.9}Zn_{0.1}Te$	CdTe
Avg. atomic n. Z	49.1	50
Density $\left(\mathrm{g\cdot cm^{-3}}\right)$	5.78	5.85
Band gap E_g (eV)	1.572	1.5
Resistivity (Ωcm)	3×10^{10}	10^9
Electron mobility μ_n $(\mathrm{cm^2V^{-1}s^{-1}})$	1000	1150
Hole mobility μ_p $(\mathrm{cm^2V^{-1}s^{-1}})$	50	110
$(\mu\tau)_n$ $\left(\mathrm{cm^2V^{-1}}\right)$	$(3-10)\times10^{-3}$	3.3×10^{-3}
$(\mu\tau)_p$ $\left(\mathrm{cm^2V^{-1}}\right)$	5×10^{-5}	2×10^{-4}

Table 1.1: Several material properties of CdZnTe and CdTe at 300 K (according to [27] and [18]).

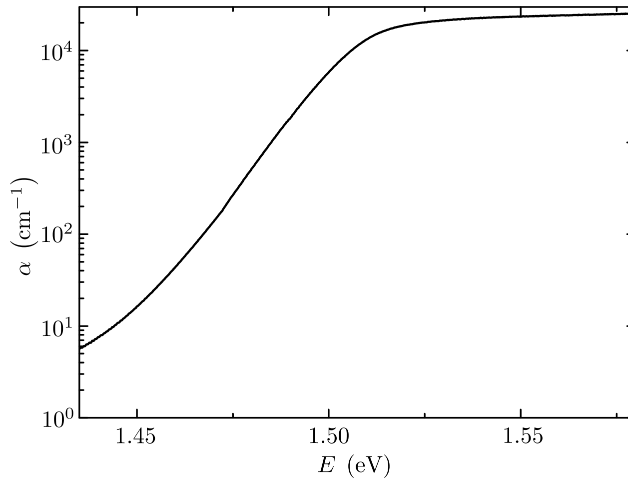

Figure 1.1: Absorption coefficient α of CdTe dependency on photon energy $E = h\nu$ around the bandgap energy E_g, $T = 300K$. [22]

1.3 Semiconductor radiation detector

In its simplest form the detector consists of a bulk semiconductor equipped with two planar electrodes. Absorbed high energy X-ray or gamma ray photons coming from an external source generate electron-hole pairs. Photogenerated electrons and holes are drifting towards the anode and the cathode, respectively in the applied electric field. The quality of the detector decreases with charge loss in the detector caused by charge trapping or recombination.

The detector quality can be described by the mobility-lifetime ($\mu\tau$) product. Good detector satisfies the following condition

$$t_d \ll \tau, \tag{1.1}$$

where t_d is the drift time of carriers and τ is their lifetime described by Hall-Shockley-Read model (see section 2.1). The drift velocity $\mathbf{v_d}$ ($v_d \sim t_d^{-1}$) depends on the carrier mobility μ and the applied electric field $\mathbf{E}$

$$\mathbf{v_d} = \mu\mathbf{E}. \tag{1.2}$$

The mean free path of electrons (holes) $\lambda_{n(p)}$ is[2]

$$\lambda_{n(p)} = (\mu\tau)_{n(p)}\,\mathcal{E}. \tag{1.3}$$

Charge collection efficiency (CCE) of the detector is a ratio of the collected charge Q and the photogenerated charge Q_0 and is described by the Hecht equation [28]

$$CCE = \frac{Q}{Q_0} = \frac{\lambda_n}{d}\left(1 - \mathrm{e}^{-\frac{d-x}{\lambda_n}}\right) + \frac{\lambda_p}{d}\left(1 - \mathrm{e}^{-\frac{x}{\lambda_p}}\right), \tag{1.4}$$

where d is detector thickness (distance between the electrodes) and x is the distance between the cathode and the position within the detector where electron-hole pairs are generated.

Reduced capturing and recombination of charge carriers lead to the higher $\mu\tau$ product of the detector material. The properties of several semiconductor detector materials are shown in table 1.2. It is well known that $(\mu\tau)_p$ for CdTe and CdZnTe is more than ten times lower than $(\mu\tau)_n$. So the contribution of the hole current must be fully (or mostly) suppressed in detectors with required higher spectral resolution [29–31].

Semi-insulating CdTe and CdZnTe can operate at room temperature due to

[2] $\mathcal{E} = |\mathbf{E}|$

Material	$Cd_{0.9}Zn_{0.1}Te$	CdTe	Ge	Si	GaAs
Avg. atomic n. Z	49.1	50	32	14	32
Density $(g \cdot cm^{-3})$	5.78	5.85	5.33	2.33	5.32
Band gap E_g (eV)	1.572	1.5	0.67	1.12	1.43
Resistivity Ωcm	3×10^{10}	10^9	50	$< 10^4$	10^7
$(\mu\tau)_n$ (cm^2V^{-1})	$(3-10) \times 10^{-3}$	3.3×10^{-3}	> 1	> 1	8×10^{-5}
$(\mu\tau)_p$ (cm^2V^{-1})	5×10^{-5}	2×10^{-4}	> 1	> 1	4×10^{-6}

Table 1.2: Several semiconductor material properties at 300 K (according to [27]).

their relatively high bandgap energy E_g causing the suppression of dark current and increase of the signal to noise ratio. On the contrary, Ge having a lower bandgap, must be cooled down during operation to achieve a good performance.

Probability of photoelectric absorption of high energy photons strongly depends on an atomic number Z of detector material as $\sim Z^{4-5}$ [32]. Thus Si shows $150 - 600$ times lower probability of absorption than CdTe.

Low thermal noise is associated with high resistivity of materials ($\rho \geq 10^9$ Ωcm) that is reached by compensation of impurities and fixing the Fermi level E_f at mid-gap during crystal growth. If it is necessary, that dark current can be further reduced by the use of blocking contacts [33]. Currently, the most of CdTe based detectors are made of semi-insulating CdTe and CdZnTe crystals equipped with electrodes (Au, Pt, In) forming Schottky barriers [34].

CdTe and CdZnTe satisfy prerequisites of good room temperature high energy detector material due to a wide energy band gap E_g and high probability of absorption due to the high average atomic number Z.

1.4 Crystal defects and energy levels

Microscopic crystal defects play an important role in electrical properties of semiconductors and those properties can be controlled by proper doping and crystal growth. Point defects are discussed in this section. An influence of line, planar and bulk defects is out of the focus of this thesis.

1.4.1 Undoped (CdZn)Te

Several energy levels related to native point defects have been observed in undoped (CdZn)Te. Undoped CdTe is usually a low resistivity material. Theoretical studies have shown that under Te rich conditions, CdTe is p-type with cadmium vacancy V_{Cd} acting as a dominant acceptor [35], while under Cd rich conditions, CdTe is n-type with interstitial Cd_I acting as a dominant donor [36]. The high resistivity of undoped CdTe is caused by relatively low concentration of electrically active impurities.

1.4.2 Doped (CdZn)Te

In order to get high resistivity, it is necessary to introduce in the material more defects and impurities that compensate native defects . It has been proven that it is convenient to dope material with transition elements or the elements from groups I, III, IV and VII [37].

Dopants of transition metals occupy the Cd site and form near midgap donor levels [38]. High resistivity states can be reached by doping with vanadium or copper. Although copper doping increases the resistivity of the material, it reduces carriers lifetimes [39].

Elements from groups I, II, III and VII introduce shallow energy levels (< 0.2 eV) due to their low ionization energies, while elements from group IV, especially Ge and Sn [40] introduce deep levels.

Group I elements on Cd sites act as acceptors, while they act as donors on interstitial sites [41]. Group III elements on Cd sites and group VII elements on Te sites form donor levels. Doping by these elements compensates impurities and native defects in undoped materials.

A detailed overview of the impact of dopants on detector material properties can be found in ref. [42]. Table 1.3 shows several energy levels and their origins in doped and undoped (CdZn)Te found in the literature.

1.4.3 Compensation of shallow defects

Due to a presence of native cadmium vacancies (V_{Cd}) and tellurium interstitials (Te_I) acting as shallow acceptors and donors, respectively, the resistivity of undoped (CdZn)Te is therefore usually low. The high resistivity of the material can be reached introducing a deep energy level (i.e. by doping). Based on the so called three levels compensation model [43] we can explain why the presence of the deep level is necessary for high resistivity of the material.

Let us consider the presence of shallow acceptors and donors with energies E_a and E_d and concentrations N_a and N_d, respectively. If $N_a > N_d$, electrons released from donors recombine with acceptor holes. Acceptors are partly ionized (fig.1.2a) and therefore the material is p-type with a low resistivity.

Adding a deep donor level E_t close to the midgap (fig.1.2b) with concentration N_t and if $N_t \gg N_a - N_d$, the deep level is partly ionized emitting electrons that recombine with holes from the shallow acceptor. Now the Fermi level E_f is pinned close to the midgap and the material shows high resistivity.

The compensation described above is valid if the deep level is associated with a dopant (i.e. Ge, Sn). In this case the mobility-lifetime product of electrons is low. Instead of using dopants that introduce deep levels, it is necessary to implement shallow donors in undoped crystals in order to compensate cadmium vacancies

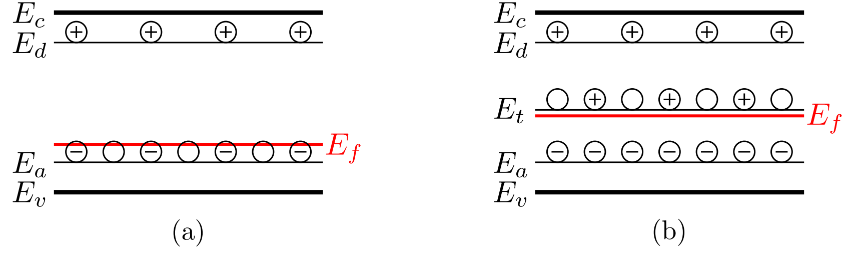

Figure 1.2: Three levels compensation model. (a) Partly ionized shallow acceptor, (b) partly ionized deep donor.

V_{Cd} (acceptor) and partially the deep level present in the crystal whose origin is unknown. It was experimentally proven, that doping with In or Cl increases material resistivity [39]. Indium and chlorine form shallow donors In_{Cd} [44] and Cl_{Te} [45], respectively. This doping is accompanied by the formation of donor-V_{Cd} complexes called A-centers and self-compensation processes.

E_A (eV)	Type	σ (cm^2)	Origin	Method†	Ref.
0.014	donor		Al	PL	[46]
0.014	donor		Cl	EPR	[47]
0.014	donor		F	PL	[46]
0.014	donor		Ga	PL	[46]
0.014	donor		In	PL	[46]
0.015	donor		Cl	PL	[46]
0.05	donor		Mn	Hall	[48]
0.056	acceptor		N	PL	[49]
0.058	acceptor		Li	PL	[50]
0.059	acceptor		Na	PL	[50]
0.068	acceptor		P	PL	[49]
0.092	acceptor		As	PL	[49]
0.1	acceptor		V_{Cd}	DLTS, PICTS	[51]
0.1	acceptor	(6.4-8.4)$\times 10^{-16}$	V_{Cd}	TEES	[52]
0.108	acceptor		Ag	PL	[53]
0.12	acceptor		Cl-V_{Cd}	PL, ODMR	[45]
0.146	acceptor		Cu	PL	[54]
0.15	acceptor		Fe	SPS	[55]
0.2	acceptor		Fe	CPM	[56]
0.21	acceptor		V_{Cd}	TEES	[57]
0.21	acceptor	5×10^{-14}	In, undop.	DLTS	[58]
0.22	acceptor	8.6×10^{-13}	In	DLTS	[58]
0.23	acceptor	2×10^{-15}	In	QTS	[59]
0.23	acceptor	3-4$\times 10^{-13}$	In		[60]
0.23-0.25	acceptor	(1.8-9)$\times 10^{-16}$	V_{Cd}	TEES	[52]
0.24		2-6$\times 10^{-17}$	unknown	DLTS	[58]
0.25		2-3$\times 10^{-19}$	unknown		[61]
0.263	acceptor		Au	PL	[50]
0.28	acceptor	2×10^{-13}	In		[60]

Table 1.3: Overview of energy levels in (CdZn)Te. (Continue on the following page)
†) See the last caption.

E_A (eV)	Type	σ (cm^2)	Origin	Method†	Ref.
0.28	acceptor	6.5×10^{-13}	In, undop.	DLTS	[58]
0.32	acceptor	2×10^{-14}	In	QTS	[59]
0.34	acceptor	1-5.5$\times10^{-13}$	In	DLTS	[46]
0.34	acceptor	1×10^{-13}	In		[60]
0.35	acceptor		Fe	EPR, ODMR, PL	[62]
0.36	acceptor		Cu	PICTS	[63]
0.37	acceptor		Cu	PICTS	[64]
0.38	acceptor	4.9×10^{-14}	In		[60]
0.38	acceptor	3×10^{-9}	In, undop.	DLTS	[58]
0.38	acceptor	0.9×10^{-13}	Sn	QTS	[59]
0.39-0.43	donor	(2.3-4.9)$\times10^{-13}$	Te_{Cd}	TEES	[52]
0.4	acceptor		V_{Cd}	DLTS, PICTS	[51]
0.4	donor		V_{Te}	theory	[35]
0.43	acceptor		V_{Cd}	TEES	[65]
0.43	donor	4×10^{-14}	Sn	QTS	[59]
0.43	acceptor		Fe	TSC	[56]
0.43-0.49	acceptor	1.1×10^{-14}	Te_{Cd}-2V_{Cd}	TEES	[52]
0.46	acceptor	4×10^{-14}	In, undop.	DLTS	[58]
0.47	acceptor	2×10^{-15}	In		[60]
0.5	donor	1×10^{-16}	V_{Te}	theory	[61,66]
0.51	acceptor	1×10^{-14}	Sn	QTS	[59]
0.51	acceptor		V	TSC	[56]
0.54	donor		Cd_I	PICTS	[64]
0.55	acceptor		Sn	TEES	[67]
0.58	acceptor	2×10^{-15}	In	DLTS	[58]
0.64	donor	4×10^{-12}	Cd_I	DLTS, PICTS	[51,59]
0.67	donor		V	Photo-EPR	[68]
0.68	acceptor	3×10^{-13}	In	DLTS	[58]
0.69-0.71	acceptor	(1.8-4.7)$\times10^{-14}$	Te_{Cd}-2V_{Cd}	TEES	[52]
0.73	donor		V_{Cd}	TEES	[57]
0.73	acceptor		V_{Cd}	TEES	[67,69]
0.73	acceptor		Ge	Photo-EPR	[49]
0.73	donor		Mn	Hall	[48]
0.73	donor		Ti	PL	[53]
0.73-0.85	acceptor	1.58×10^{-12}	Te_{Cd}-V_{Cd}	TEES	[52]
0.74	donor		Te_{Cd}	TEES	[67,69]
0.74	acceptor	1-6$\times10^{-14}$	In, undop.		[60]
0.74	acceptor		V	theory	[70]
0.76	acceptor		V_{Cd}	DLTS, PICTS	[51]
0.76	donor		Ni	CPM	[56]
0.78	acceptor	4×10^{-13}	V_{Cd}	PICTS	[39,59]
0.8	acceptor	5×10^{-13}	In	QTS	[59]
0.83	donor		Ti	DLTS	[71]
0.85	donor		Sn	Photo-EPR	[62]
0.86	acceptor	2×10^{-12}	In, undop.	DLTS	[58]
0.88		1.2×10^{-12}	unknown		[61]
0.89	donor	5×10^{-12}	Sn	QTS	[59]
0.9	donor		Sn	DLTS	[72]
0.92	acceptor		Ni	EPR, ODMR, PL	[56]

Table 1.3: Overview of energy levels in (CdZn)Te. (Continue on the following page)
†) See the last caption.

E_A (eV)	Type	σ (cm^2)	Origin	Method†	Ref.
0.95	donor		Ge	Photo-EPR	[62]
0.95	donor		V	DLTS	[73]
1.1	donor		V_{Te}	DLTS,PICTS	[51]
1.25	acceptor		Co	EPR, ODMR, PL	[74]
1.28	donor		Pb	Photo-EPR	[75]
1.34	acceptor		Cr	EPR, ODMR, PL	[76]
1.4	donor		V_{Te}	Photo-EPR	[77]
1.45	donor		Fe	Photo-EPR	[78]

Table 1.3: Overview of energy levels in (CdZn)Te. (Continued from the previous page)
†) CPM... Constant photocurrent method, DLTS... Deep level transient spectroscopy, EPR... Electron paramagnetic resonance, Photo-EPR... Photo electron paramagnetic resonance, Hall... Hall measurements, ODMR... Optically detected magnetic resonance, PICTS... Photo induced current transient spectroscopy, PL... Photoluminescence, QTS... Charge transient spectroscopy, SPS... Surface plasmon spectroscopy, TEES... Thermal emission electron spectroscopy, TSC... Thermally stimulated current spectroscopy.

1.5 The goal of this thesis

This thesis is mainly focused on a study of electric field profiles in detectors under dark and high flux conditions simulating detector operation. It also deals with a study of deep levels responsible for the polarization and influence of contact metals on charge accumulation.

Used electric field measurements based on crossed polarizers technique exploiting Pockels effect on (CdZn)Te have been studied by many groups since late 1990's [12, 79–82]. This strong universal method and its modifications allow us to study internal processes including the accumulation of a space charge and influence of contact metals on the band bending at a metal-semiconductor interface in detectors. The Pockels effect method is supported by photoconductivity measurements. Several experimental results are accompanied by theoretical simulations. A new method of deep level spectroscopy was developed during the work on this thesis. It is based on a modified setup of the Pockels effect measurement exploiting infrared spectral scanning. We also implemented temperature dependent measurement of discharged currents to study a trapping of electric charge at deep levels.

The measurements were performed on three sets of samples cut from three different n-type CdTe and CdZnTe materials equipped with different contact metals (Au, In).

Chapter 2

Theory

The band structure of an ideal semiconductor crystal consists of the conduction band (E_c) and the valence band (E_v) divided by a bandgap of forbidden energies (E_g). For a crystal with defects there are discreet energy states with levels E_t inside the bandgap that act as generation and recombination centers for charge carriers. Origins of the defects are natural defects of crystal matrix and impurities of atoms of other elements and their combinations.

2.1 Hall-Shockley-Read model

Generation and recombination of electrons and holes in a semiconductor with one generation-recombination level E_t with concentration N_t can be statistically described by the Hall-Shockley-Read model [83], [84]. Generation and recombination processes between energy bands and the energy level within the bandgap are schematically shown on fig.2.1.

Free charge carriers are described by concentrations n and p of electrons and holes in conduction and valence bands, respectively and thermal velocities

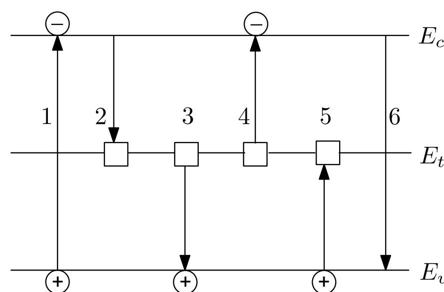

Figure 2.1: The scheme of energy band structure used in the Hall-Shockley-Read model. Basic processes on the generation-recombination center with energy E_t: 1-interband generation of electron-hole pair, 2-capture of electron, 3-capture of hole, 4-generation of free electron, 5-generation of free hole, 6-interband recombination.

v_{th}^e and v_{th}^h for electrons and holes, respectively. Parameters of the generation-recombination center (capture cross-sections σ_n and σ_p for electrons and holes, respectively and N_t) are independent on the surrounding system and correspond to the steady state. All kinds of transitions shown on fig.2.1 are considered to be immediate.

Concentrations n_t and p_t of electrons and holes on the center give its total concentration N_t:

$$N_t = n_t + p_t. \tag{2.1}$$

Energy levels can be divided on the following types based on the ratio of their electron and hole capture cross-sections

- $\sigma_n \approx \sigma_p$ ... recombination center
- $\sigma_n > \sigma_p$ ... electron trap
- $\sigma_n < \sigma_p$ ... hole trap

Equilibrium (dark condition) life times τ_n and τ_p of free electrons and holes, respectively with respect to a trapping at the level are

$$\begin{aligned} \tau_n &= \frac{1}{c_n\left(N_t - n_t\right)}, \\ \tau_p &= \frac{1}{c_p\left(N_t - n_t\right)}. \end{aligned} \tag{2.2}$$

where $c_n = \sigma_n v_{th}^e$ and $c_p = \sigma_p v_{th}^h$ are capture coefficients for electrons and holes, respectively.

Time changes of non-equilibrium concentrations n, p and n_t are described with the following kinetic equations

$$\begin{aligned} \frac{dn}{dt} &= \mathcal{G} - c_n\left(N_t - n_t\right) + c_n n_1 n_t, \\ \frac{dp}{dt} &= \mathcal{G} - c_p p n_t + c_p p_1 (N_t - n_t), \\ \frac{dn_t}{dt} &= c_n n\left(N_t - n_t\right) - c_n n_1 n_t - c_p p n_t + c_p p_1\left(N_t - n_t\right), \end{aligned} \tag{2.3}$$

where $\mathcal{G}$ is the rate of charge carriers generation, n_1 and p_1 equilibrium concentrations of electrons and holes, respectively if $E_f = E_t$, where E_f is the Fermi level[1].

[1] The second term of the first equation of eqs.2.3 is associated with electron trapping descri-

Now it is possible to derive the simplified model for the case of electron-hole pair generation (illumination) with conditions

$$n = n_0 + \Delta n, \quad p = p_0 + \Delta p \text{ and } N_t \ll n_0, p_0, \tag{2.4}$$

where n_0 and p_0 are equilibrium concentration and $\Delta n = \Delta p$ is photogenerated deviation of concentrations of electrons and holes, respectively. Solving eqs.2.3 with respect to eq.2.4 we get the simplified Hall-Shockley-Read model for carriers lifetime

$$\tau = \tau_n = \tau_p = \frac{\tau_{n0}\left(p_0 + p_1 + \Delta n\right) + \tau_{p0}\left(n_0 + n_1 + \Delta n\right)}{n_0 + p_0 + \Delta n}, \tag{2.5}$$

where τ_{n0} resp. τ_{p0} are carriers lifetimes from eq.2.2 if $n_t = 0$.

Carrier recombination rate $\mathcal{R}$ according to this model is [84]:

$$\mathcal{R} = \frac{c_n c_p N_t\left(pn - p_1 n_1\right)}{c_n(n + n_1) + c_p(p + p_1)}. \tag{2.6}$$

2.2 Metal-Semiconductor interface (contacts)

An influence of contact metals on the band bending at metal-semiconductor (M-S) interface based on the standard model of the difference of work functions between metal and semiconductor is described in this section.

Let us consider CdZnTe/Au interface. The work function of gold Φ_{Au} is 5.3 eV [85], while the work function in semi-insulating CdZnTe Φ_{CdZnTe} ranges from 5.25 − 5.45 eV, depending on the position of the Fermi level E_f in the near-midgap region (fig.2.2a). Fig.2.2b depicts the band scheme of Au and semi-insulating CdZnTe with 10% Zn content for the case $\Phi_{CdZnTe} < \Phi_{Au}$. Here, CdZnTe is slightly n-type, the bands at the interface are oriented upwards.

Using the model based on the work functions differences we can determine the boundary conditions of carriers density n and p at M-S interface. Without loss of generality, let us consider symmetric Au/CdZnTe/Au structure with a thickness d. The boundary conditions are set by the Fermi energy of semiconductor pinned to the E_f in the metal, which yields band bending at the surface:

$$E_{cs} - E_c = E_{vs} - E_v = \Phi_{Au} - \Phi_{CdZnTe}, \tag{2.7}$$

where E_{cs} and E_{vs} represent the energy of the conduction and the valence band at the M-S interface, respectively (fig.2.2b). This fixes the surface-carrier density [86]

bed by eq.2.2 and the third term is associated with electron re-trapping from the level E_t into the conduction band etc.

as

$$n(0) = n(d) = n_0 \exp\left(\frac{\Phi_{CdZnTe} - \Phi_{Au}}{k_B T}\right),$$
$$p(0) = p(d) = p_0 \exp\left(\frac{\Phi_{Au} - \Phi_{CdZnTe}}{k_B T}\right), \tag{2.8}$$

where n_0 and p_0 are equilibrium electron and hole densities, respectively.

The same approach is suitable for other contact metals. While gold can form an Ohmic, slightly blocking or slightly injecting contact on semi-insulating CdTe depending on the actual position of the Fermi level in CdTe and the voltage polarity, indium having a much smaller work function ($\Phi_{In} \sim 4.1$ eV) is a clear candidate for a hole blocking contact (bands bent downwards) when used as an anode. However, surface dipoles can substantially modify the expected values as derived from the simple work function difference model.

2.3 Poisson's equation

The internal electric field $\mathbf{E_{in}}$ induced by a space charge is described by the Gauss law

$$\nabla \cdot \mathbf{E_{in}}(\mathbf{r}) = \frac{\varrho(\mathbf{r})}{\epsilon}, \tag{2.9}$$

where ϱ is the space charge density, ϵ is the permittivity of a medium and $\mathbf{r}$ is the directional vector.

The electrostatic potential φ is defined as

$$\mathbf{E}(\mathbf{r}) = -\nabla\varphi(\mathbf{r}) \tag{2.10}$$

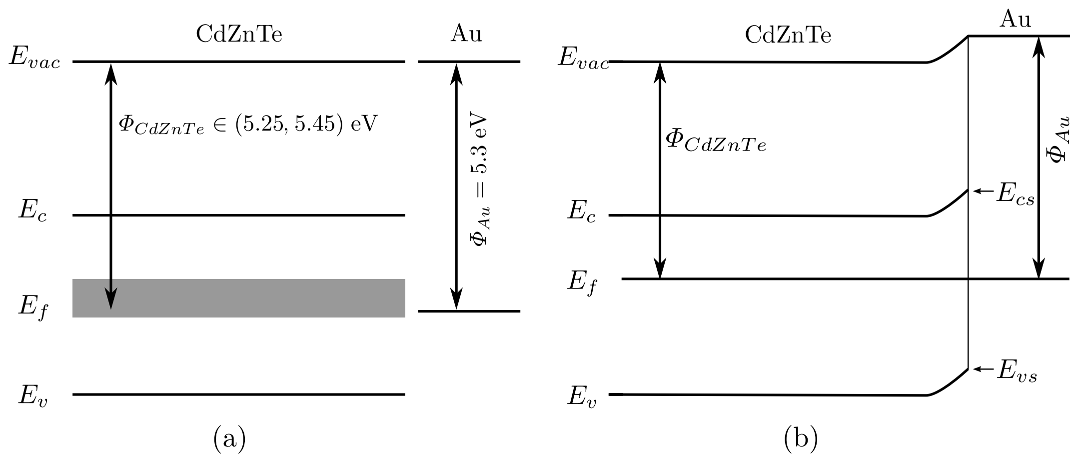

Figure 2.2: Band scheme of the M-S interface of CdZnTe/Au. (a) Comparison of work functions of CdZnTe and gold. (b) The case when $\Phi_{CdZnTe} < \Phi_{Au}$.

and the Poisson's equation is

$$\Delta\varphi(\mathbf{r}) = -\frac{\varrho(\mathbf{r})}{\epsilon}. \tag{2.11}$$

Total space charge

The total space charge Q_{tot} inside a semiconductor detector is a superposition of a space charge Q_{ph} of a photogenerated charge trapped at deep levels at high fluxes and the space charge Q_{ms} due to a charge accumulated due to the band bending at the metal-semiconductor interface:

$$Q_{tot} = Q_{ph} + Q_{ms}. \tag{2.12}$$

2.4 Drift-diffusion equation

A movement of charge carriers in solids is described by the drift-diffusion equation. Specifically, the electron[2] current density $\mathbf{j}_e$ is

$$\mathbf{j}_e = e\mu_e n\mathbf{E} + \mu_e k_B T\nabla n + \mu_e k_B n\nabla T, \tag{2.13}$$

where e is the elementary charge, $\mathbf{E}$ is the electric field, T is the temperature and μ_e is the electron mobility

$$\mu_e = \frac{e}{m_e^*}\tau_n, \tag{2.14}$$

where m_e^* is the electron effective mass. Analogous equations are valid for a case of the transport of holes.

The first term of eq.2.13 describes the drift of carriers caused by an external electric field, while the second term is associated with the motion of free carriers from a place with a higher concentration to a lower (diffusion) and the last term is associated with a diffusion from a position with a higher temperature to a lower. The last term equals to zero if the temperature is constant. Therefore eq.2.13 is reduced to

$$\mathbf{j}_e = e\mu_e n\mathbf{E} + \mu_e k_B T\nabla n. \tag{2.15}$$

[2] Equation 2.13 is also valid for holes after substitution of variables.

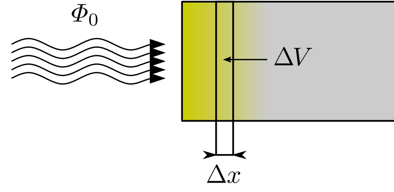

Figure 2.3: Absorption of the incident radiation within a small sample volume ΔV.

2.5 Processes in the sample after illumination

Processes in the detector samples after illumination are described in this section because the visible and the near infrared lights were exploited for the excitation of the samples during the measurements.

Absorption of materials is described by the Lambert-Beer law as

$$\Phi(x) = \Phi_0 \mathrm{e}^{-\alpha x}, \tag{2.16}$$

where Φ_0 is an incident light photon flux (or an intensity), $\Phi(x)$ is the photon flux at the distance x calculated from the surface inside the material with the absorption coefficient α.

The generation rate of charge carriers $\mathcal{G}$ can be expressed as a decrease $\Delta\Phi(x)$ of the incident flux Φ_0 absorbed within a very small sample volume ΔV along the distance Δx (see fig.2.3):

$$\mathcal{G} = -\lim_{\Delta x \to 0} \frac{\Delta\Phi(x)}{\Delta x} = \Phi_0 \alpha \mathrm{e}^{-\alpha x}. \tag{2.17}$$

There is an important consequence of the Lambert-Beer law (eq.2.16) and of the spectral dependence of the absorption coefficient presented on fig.2.4. It is possible to control the depth of a light penetration using its different wavelength. Using proper polarity of applied voltage on the sample and the depth of light penetration it is possible to distinguish, in the special case described in the next paragraph, between types of carriers (electrons or holes) participating on a photoelectric transport (fig.2.4a) or generate both types of carriers in a whole sample volume (fig.2.4b).

The case of high absorption ($h\nu > E_g$) is described in more details for electrons on fig.2.5. The situation would be similar for holes using an opposite polarity. The case of deeper penetration ($h\nu < E_g$) when both types of the space charge are created is more complex. This situation is discussed in section 4.3.2.

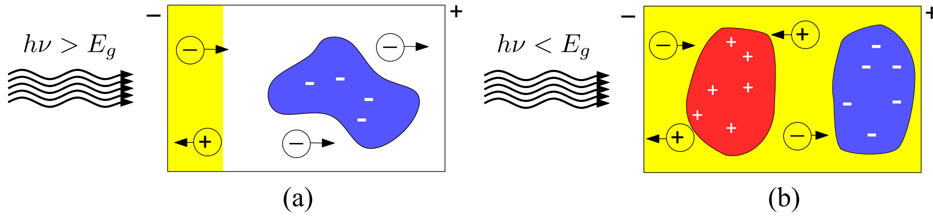

Figure 2.4: Two cases of the light penetration in a biased sample. The cathode is illuminated. a) Above bandgap radiation ($h\nu > E_g$) is absorbed within a thin (few μm) layer under the surface. Holes immediately recombine at the cathode and only electrons participate on photoelectric transport towards the anode. Trapped electrons form a negative space charge. b) Sub bandgap radiation ($h\nu < E_g$) can penetrate through the whole sample volume, where electron-hole pairs are generated. Both types of carriers participate on a photoelectric transport and both types of space charges can be formed.

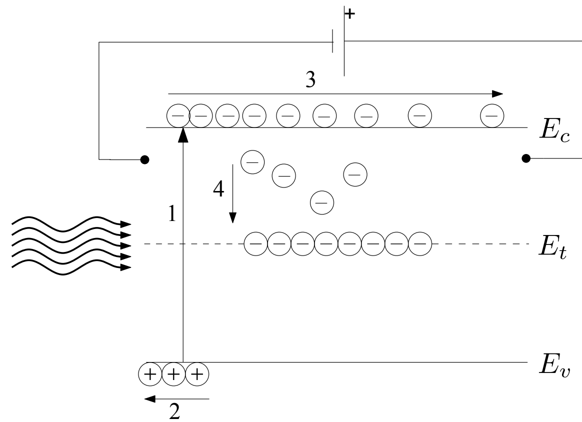

Figure 2.5: Illustration of processes in the sample after irradiation (above gap wavelength $h\nu > E_g$). (1) Electron-hole pair generation under the surface. (2) Holes immediately recombine at the cathode. (3) Electrons drift towards the anode and can be trapped at deep level E_t (4).

2.6 Numerical simulations

Several acquired experimental data were simulated using software developed at the Institute of Physics, Charles University by Assoc. prof. Roman Grill in order to analyze the results. The background of numeric simulations is described in this section. Steady state model is based on the simultaneous solution of the drift-diffusion (eq.2.15) and the Poisson (eq.2.11) equations of a system consisting of one deep level characterized by an ionization energy and electron and hole capture cross sections. The standard Shockley–Read model describes recombination through the level (eq.2.6). Charge carriers generation is described by eq.2.17. The boundary conditions are set by the Fermi energy pinned to the metal, which yields band bending at the surface (eq.2.8).

In this model we consider a planar detector sample with a thickness d equipped with electrodes. Direction of propagation of an incident radiation with a photon flux Φ_0 is parallel to the applied electric field $\mathbf{E}$ (fig.2.6). The sample is cha-

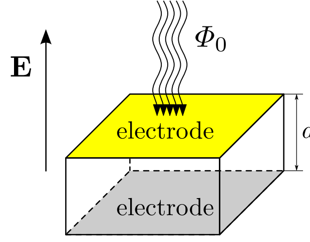

Figure 2.6: Scheme of a planar detector sample with a thickness d equipped with electrodes and the direction of propagation of an incident radiation with photon flux Φ_0 passing through the electrode.

racterized by its Fermi energy E_f and the deep level energy E_t with concentration N_t and its capture cross sections σ_n and σ_p of electrons and holes, respectively. An influence of shallow levels is neglected. Choosing appropriate deep level and band banding parameters we are able to fit experimental data (electric field profiles and photocurrent) and therefore get information about deep levels, contacts and internal processes in the sample.

Charge conservation in the sample is described by the continuity equation

$$\nabla \cdot \mathbf{j} + \frac{\partial \varrho}{\partial t} = 0, \tag{2.18}$$

where $\mathbf{j}$ and ϱ are the current density and the space charge density, respectively. The change of the space charge density can be expressed using the generation $\mathcal{G}$ and the recombination $\mathcal{R}$ rates as

$$\frac{\partial \varrho}{\partial t} = e\left(\mathcal{G} - \mathcal{R}\right). \tag{2.19}$$

Combining eqs.2.6, 2.15, 2.17 and 2.18 with respect to eq.2.19, we get the following equation describing equilibrium of electrons[3] in the material during the steady state photo-excitation:

$$0 = \Phi_0 \alpha \mathrm{e}^{-\alpha x} + \left[\frac{k_B T}{e}\frac{\partial^2 n}{\partial x^2} + \frac{\partial}{\partial x}\left(\mathcal{E} n\right)\right] - \frac{c_n c_p N_t \left(pn - p_1 n_1\right)}{c_n(n+n_1) + c_p(p+p_1)} \tag{2.20}$$

with boundary conditions described by eq.2.8 obtained from the band bending at the M-S interface.

The space charge density ϱ is given by the occupation of bands and of the deep level as

$$\varrho = e\left(p - p_0 - n + n_0 - n_t + n_{t0}\right), \tag{2.21}$$

[3] Analogous equation can be obtained for holes.

where n_t is the trap density derived from the last equation of eqs.2.3 if $dn_t/dt = 0$

$$n_t = \frac{N_t\left(c_n n + c_p p_1\right)}{c_n\left(n + n_1\right) + c_p\left(p + p_1\right)} \tag{2.22}$$

and n_{t0} is the equilibrium trap density

$$n_{t0} = \frac{N_t}{1 + \exp\left(\frac{E_t - E_f}{k_B T}\right)}. \tag{2.23}$$

The electric field distribution $\mathcal{E}(x)$ through the sample between electrodes is calculated through the electrostatic potential $\varphi(x)$ using one dimensional modification of eq.2.10

$$\mathcal{E}(x) = -\frac{\partial\varphi(x)}{\partial x} \tag{2.24}$$

and the electrostatic potential is solved from one dimensional modification of the Poisson's equation (eq.2.11)

$$\frac{\partial^2\varphi}{\partial x^2} = -\frac{\varrho}{\epsilon} \tag{2.25}$$

using boundary conditions $\varphi(0) = 0$ and $\varphi(d) = U$, where U is the voltage applied on the sample.

Both dark current density $j(x)$ and photocurrent density $j_{pc}(x)$ are constant and $j_{pc}(x)$ is

$$j_{pc} = e\mathcal{E}(x)\left[\mu_n n(x) + \mu_p p(x)\right] - \frac{eU}{d}\left(\mu_n n_0 + \mu_p p_0\right). \tag{2.26}$$

The simulation program solves the equation 2.20 and it runs on a standard PC. The simulation time of each run critically depends on the total space charge Q_{tot} accumulated in the sample. If Q_{tot} is small (low flux, small band bending), typical simulation time is several minutes. With increased screening (high flux, large band bending, and large Q_{tot}), it can extend to several hours. Large band bending also requires a higher density of calculation points with respect to the thickness, i.e., areas of large band bending must be calculated using more points than areas where the bands are flat and the physical parameters change slowly. Therefore, a non-equidistant division of intervals is used in the iterative method.

Typically, the complicated nonlinear character of the solved set of equations results in a slow convergence of the iterative method with a strong tendency to oscillate. As is usual in such situations, the oscillations are effectively damped by averaging successive iterations, when the new iteration is involved with only a weighting of several percent.

In principle, the findings from the simulation depend on the parameters of the deep levels; hence, it is important to work with parametric quantities representing the conditions present in state-of-the-art detectors. We used a model with one near-midgap deep level fixing the Fermi level. This is the most simple model because one level can simulate both acceptors and donors, and there is no need to complicate the model with more energy levels. Addition of other levels in the upper or bottom part of the band-gap will only increase trapping of the corresponding carriers and decrease the concentration of the midgap level needed to trap the same charge [86].

2.7 Polarization in detectors

A typical distribution of the electric field $\mathcal{E}$ through a polarized detector is shown on fig.2.7. Due to a screening of the external electric field by an internal space charge the internal electric field is deformed. In the case of strong screening the so called "dead layer"can be formed. Within this layer the electric field is very weak. The charge collection efficiency (CCE) of the detector decreases because there is a very slow drift of photogenerated charge carriers (see eqs.1.4 and 2.15)[4].

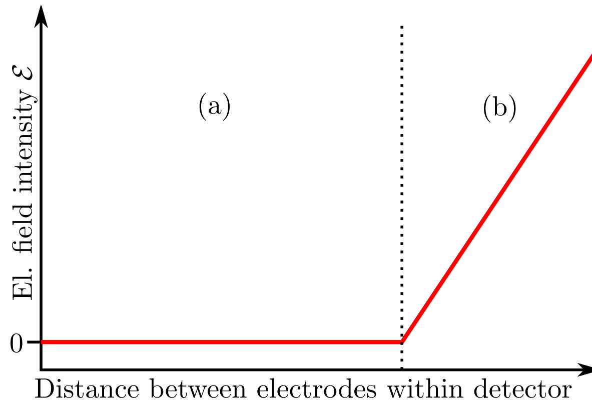

Figure 2.7: Typical distribution of the electric field within a strongly polarized detector due to the band bending at M-S interface or the combination of the band bending at the M-S interface and a space charge accumulated at a deep level. (a) is the area with a zero electric field ($\mathcal{E} = 0$) called *dead layer* and (b) is the area of an accumulated space charge ($\mathcal{E} \neq 0$) called *depletion layer*.

[4]The second (diffusion) term of eq.2.15 is negligible compared with the first one associated with the drift of carriers

2.8 Electro-optic effect and crossed polarizers technique

CdTe based compounds show electro-optic (Pockels) effect as it was mentioned in sec. 1.2. This property can be also exploited for a study of the distribution of the internal electric field through the samples that is useful to understand internal processes in the material after application of the voltage, irradiation and the band bending at metal-semiconductor interfaces.

Idea of the experiment is based on a transverse Pockels effect in which the biased sample acts as a dynamic wave retarder placed between two crossed linear polarizers (polarizer and analyzer) as described on fig.2.8. The intensity of a monochromatic testing light passing through this system varies due to the electric field distribution in the sample. The passed through light intensity is detected using CMOS camera and then the electric field distribution is reconstructed.

This section describes theoretically the principle of wave retarder placed between two crossed polarizers (section 2.8.1) and Pockels effect on CdTe based compounds (section 2.8.2). The evaluation of the internal electric field is concluded in section 2.8.2.

2.8.1 Wave retarder between two crossed linear polarizers

The Jones calculus is used for the description of the intensity transmittance $\mathcal{T}$ of the system consisting of a wave retarder placed between two crossed linear polarizers [87, chap. 6]. A monochromatic plane wave (testing light) with the wavelength λ_0 traveling in the y direction (see fig.2.8 for the spatial orientation) is described by the complex envelopes A_x and A_z of its electric field, so the Jones vector $\mathbf{J}$ of the wave can be written in the following form:

$$\mathbf{J} = \begin{bmatrix} A_x \\ A_z \end{bmatrix}. \tag{2.27}$$

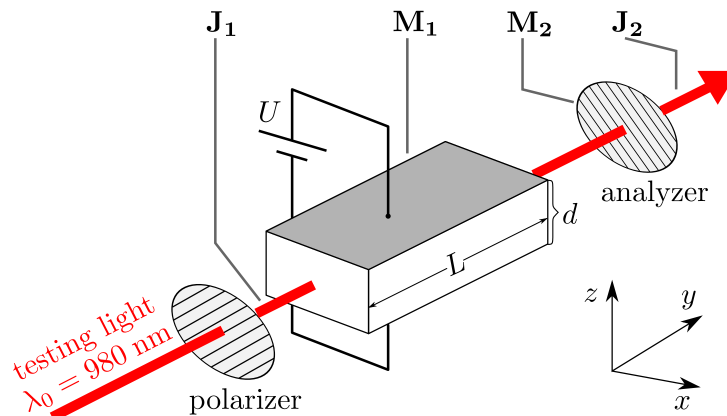

Figure 2.8: Sample acting as a dynamic wave retarder placed between two crossed linear polarizers

The polarization of the wave after passing the linear polarizer placed at 45° with respect to the x axis is described with the Jones vector $\mathbf{J_1}$ (eq.2.28):

$$\mathbf{J_1} = \begin{bmatrix} \cos 45^\circ \\ \sin 45^\circ \end{bmatrix} = \begin{bmatrix} \frac{\sqrt{2}}{2} \\ \\ \frac{\sqrt{2}}{2} \end{bmatrix}. \tag{2.28}$$

Without loss of generality, the wave retarder (sample) delays the A_z component of the testing light by a phase Γ, if the fast and the slow axis of the retarder are equal to the axis x and z, respectively this system is described by the Jones matrix $\mathbf{M_1}$ (eq.2.29):

$$\mathbf{M_1} = \begin{bmatrix} 1 & 0 \\ 0 & \mathrm{e}^{-i\Gamma} \end{bmatrix}. \tag{2.29}$$

The Jones matrix $\mathbf{M_2}$ of the analyzer (second polarizer) placed at $-45°$ with respect to the x axis is

$$\mathbf{M_2} = \begin{bmatrix} \cos^2(-45^\circ) & \sin(-45^\circ)\cos(-45^\circ) \\ \sin(-45^\circ)\cos(-45^\circ) & \sin^2(-45^\circ) \end{bmatrix} = \frac{1}{2}\begin{bmatrix} 1 & -1 \\ -1 & 1 \end{bmatrix}. \tag{2.30}$$

The polarization state of the output beam $\mathbf{J_2}$ after passing the analyzer is calculated as:

$$\mathbf{J_2} = \mathbf{M_2}\mathbf{M_1}\mathbf{J_1} = \frac{1}{8}\begin{bmatrix} 1 - \mathrm{e}^{-i\Gamma} \\ -1 + \mathrm{e}^{-i\Gamma} \end{bmatrix} \tag{2.31}$$

and the unitary intensity transmittance $\mathcal{T}$ of the system of the wave retarder between two crossed linear polarizers is

$$\mathcal{T} = A_x A_x^* + A_z A_z^* = \frac{1}{4}\left(1 - \mathrm{e}^{-i\Gamma}\right)\left(1 - \mathrm{e}^{i\Gamma}\right) = \sin^2 \frac{\Gamma}{2}. \tag{2.32}$$

2.8.2 Pockels effect

The refractive index $\mathfrak{n}$ of an electro-optic material is a function of an applied electric field $\mathcal{E}$ and it can be written as

$$\mathfrak{n}(\mathcal{E}) = \mathfrak{n}_0 + \Delta\mathfrak{n}(\mathcal{E}), \tag{2.33}$$

where $\mathfrak{n}_0 = \mathfrak{n}(0)$ and $\Delta\mathfrak{n}(\mathcal{E})$ is a small increment of the refractive index dependent on the electric field $\mathcal{E}$. $\mathfrak{n}(\mathcal{E})$ can be expanded in a Taylor's series about $\mathcal{E} = 0$ and eq.2.33 can be written [87, chap. 18] as

$$\mathfrak{n}(\mathcal{E}) = \mathfrak{n}_0 - \frac{1}{2} r \mathfrak{n}_0^3 \mathcal{E} + \ldots, \tag{2.34}$$

where r is a linear electro-optic (or so-called Pockels) coefficient[5]. If the material shows linear electro-optic effect the third and higher order terms of the series can be neglected.

It is convenient to define the dielectric impermeability $\eta(\mathcal{E})$ as

$$\eta(\mathcal{E}) = \frac{\epsilon_0}{\epsilon(\mathcal{E})} = \frac{1}{\mathfrak{n}^2(\mathcal{E})}. \tag{2.35}$$

Using eqs.2.33, 2.34 and 2.35 and the change of $\Delta\eta(\mathcal{E}) = [d\eta(\mathcal{E})/d\mathfrak{n}(\mathcal{E})]\Delta\mathfrak{n}$ it is possible to write the dielectric impermeability $\eta(\mathcal{E})$ as

$$\eta(\mathcal{E}) = \eta + r\mathcal{E}, \tag{2.36}$$

where $\eta = \eta(0)$.

Eq. 2.36 describes only the one dimensional problem. To describe the Pockels effect in a real electro-optic crystal under the applied external electric field $\mathbf{E} = [\mathcal{E}_1, \mathcal{E}_2, \mathcal{E}_3]$ it is necessary to use the dielectric impermeability tensor $\eta_{ij}(\mathbf{E})$:

$$\eta_{ij}(\mathbf{E}) = \eta_{ij} + \sum_k r_{ijk}\mathcal{E}_k, \quad \text{where } i, j, k = 1, 2, 3, \tag{2.37}$$

$\eta_{ij} = \eta_{ij}(0)$ and r_{ijk} is a third-rank tensor of Pockels coefficients.

Due to the fact, that the dielectric impermeability tensor is symmetric[6] ($\eta_{ij} = \eta_{ji}$), it is possible to reduce indices i and j of the Pockels coefficients to one index I according to the table 2.1:

ij	11	22	33	23, 32	13, 31	12, 21
I	1	2	3	4	5	6

Table 2.1: Indices reduction in r_{ijk}

Now the difference of the dielectric impermeability tensor $\Delta\eta_{ij} = \sum_k r_{Ik}\mathcal{E}_k$ can be written as

[5] The value of the linear electro-optic coefficient r_{41} for CdTe is very low ($r_{41} = 5.5 \times 10^{-12}$cm/V at the wavelength 1$\mu$m, see [88]) with respect to its refractive index $\mathfrak{n}_0 = 2.9$ [89] and applied electric field E (typically $\mathcal{E} \leq 10^4$V/cm) so it is possible to justify the use of Taylor's series for $\mathfrak{n}(\mathcal{E})$ about $\mathcal{E} = (0)$.

[6] The symmetry of η_{ij} directly corresponds to the symmetry of the tensor of dielectric permittivity $\epsilon_{ij} = \epsilon_{ji}$. This equality can be proven using Poynting's theorem (see [90, p. 240]).

$$\begin{bmatrix} \Delta\eta_{11} \\ \Delta\eta_{22} \\ \Delta\eta_{33} \\ \Delta\eta_{23} \\ \Delta\eta_{31} \\ \Delta\eta_{12} \end{bmatrix} = \begin{bmatrix} r_{11} & r_{12} & r_{13} \\ r_{21} & r_{22} & r_{23} \\ r_{31} & r_{32} & r_{33} \\ r_{41} & r_{42} & r_{43} \\ r_{51} & r_{52} & r_{53} \\ r_{61} & r_{62} & r_{63} \end{bmatrix} \begin{bmatrix} \mathcal{E}_1 \\ \mathcal{E}_2 \\ \mathcal{E}_3 \end{bmatrix}. \qquad (2.38)$$

The matrix r_{Ik} of Pockels coefficients for zinc-blende structure (cubic $\bar{4}3m$ symmetry) is reduced due to a crystal symmetry and only the coefficients $r_{41} = r_{52} = r_{63}$ are non-zero [91, chap. 8] and the dielectric impermeability tensor $\Delta\eta_{ij}$ under the applied electric field $\mathbf{E}$ can be rewritten as

$$\begin{bmatrix} \Delta\eta_{11} \\ \Delta\eta_{22} \\ \Delta\eta_{33} \\ \Delta\eta_{23} \\ \Delta\eta_{31} \\ \Delta\eta_{12} \end{bmatrix} = \begin{bmatrix} 0 & 0 & 0 \\ 0 & 0 & 0 \\ 0 & 0 & 0 \\ r_{41} & 0 & 0 \\ 0 & r_{41} & 0 \\ 0 & 0 & r_{41} \end{bmatrix} \begin{bmatrix} \mathcal{E}_1 \\ \mathcal{E}_2 \\ \mathcal{E}_3 \end{bmatrix}. \qquad (2.39)$$

The modified index ellipsoid for a general crystal under arbitrary electric field $\mathbf{E}$ can be written as

$$\sum_{ij} \eta_{ij}(\mathbf{E}) x_i x_j = 1. \qquad (2.40)$$

For $\bar{4}3m$ crystals $\eta_{11} = \eta_{22} = \eta_{33} = 1/n_0^2$ because if $\mathbf{E} = 0$, the crystal is isotropic. So the eq.2.40 is reduced using eq.2.39 to

$$\frac{x_1^2 + x_2^2 + x_3^2}{n_0^2} + 2r_{41}(\mathcal{E}_1 x_2 x_3 + \mathcal{E}_2 x_3 x_1 + \mathcal{E}_3 x_1 x_2) = 1. \qquad (2.41)$$

Eq.2.41 is the index ellipsoid of $\bar{4}3m$ crystals under the electric field applied in a general direction. Components $\mathcal{E}_1, \mathcal{E}_2$ and $\mathcal{E}_3$ are parallel to the directions of the three crystallographic axes.

Now let us consider the homogenous electric field $\mathbf{E}$ applied in the direction perpendicular to the (111) plane *(This situation corresponds to the most of the measurements described later in this thesis)*. The projection of the electric field into the x_1, x_2 and x_3 axes is

$$\mathbf{E} = \frac{\mathcal{E}}{\sqrt{3}} [1, 1, 1] \qquad (2.42)$$

and eq.2.41 can be rewritten as

$$\frac{x_1^2 + x_2^2 + x_3^2}{n_0^2} + \frac{2}{\sqrt{3}} r_{41} \mathcal{E} (x_2 x_3 + x_3 x_1 + x_1 x_2) = 1. \tag{2.43}$$

The principal axes of index ellipsoid (eq.2.43) can be found by diagonalizing the matrix $\eta_{ij}(\mathbf{E})$

$$\eta_{ij}(\mathbf{E}) = \begin{pmatrix} \frac{1}{\mathfrak{n}_0^2} & \frac{r_{41}\mathcal{E}}{\sqrt{3}} & \frac{r_{41}\mathcal{E}}{\sqrt{3}} \\ \frac{r_{41}\mathcal{E}}{\sqrt{3}} & \frac{1}{\mathfrak{n}_0^2} & \frac{r_{41}\mathcal{E}}{\sqrt{3}} \\ \frac{r_{41}\mathcal{E}}{\sqrt{3}} & \frac{r_{41}\mathcal{E}}{\sqrt{3}} & \frac{1}{\mathfrak{n}_0^2} \end{pmatrix}. \tag{2.44}$$

The diagonalized matrix $\eta'_{ij}(\mathbf{E})$ is

$$\eta'_{ij}(\mathcal{E}) = \begin{pmatrix} \frac{1}{\mathfrak{n}_0^2} - \frac{r_{41}\mathcal{E}}{\sqrt{3}} & 0 & 0 \\ 0 & \frac{1}{\mathfrak{n}_0^2} - \frac{r_{41}\mathcal{E}}{\sqrt{3}} & 0 \\ 0 & 0 & \frac{1}{\mathfrak{n}_0^2} + \frac{2r_{41}\mathcal{E}}{\sqrt{3}} \end{pmatrix}, \tag{2.45}$$

where the diagonal entries are eigenvalues of $\eta_{ij}(\mathbf{E})$ that correspond to refractive indices for new coordinate axes x'_1, x'_2 and x'_3 as written in eq.2.46:

$$\begin{array}{ll} \text{Direction} & \text{Refractive index} \\ x'_1 & \frac{1}{\mathfrak{n}^2_{x'_1}(\mathcal{E})} = \frac{1}{\mathfrak{n}_0^2} - \frac{1}{\sqrt{3}} r_{41}\mathcal{E}, \\ x'_2 & \frac{1}{\mathfrak{n}^2_{x'_2}(\mathcal{E})} = \frac{1}{\mathfrak{n}_0^2} - \frac{1}{\sqrt{3}} r_{41}\mathcal{E}, \\ x'_3 & \frac{1}{\mathfrak{n}^2_{x'_3}(\mathcal{E})} = \frac{1}{\mathfrak{n}_0^2} + \frac{2}{\sqrt{3}} r_{41}\mathcal{E}. \end{array} \tag{2.46}$$

The change of refractive indices under the electric field is very low. Using the approximation $(1+\Delta)^{-\frac{1}{2}} \approx 1 - \frac{1}{2}\Delta$ we get

$$\mathfrak{n}_{x'_1}(\mathcal{E}) = \mathfrak{n}_{x'_2}(\mathcal{E}) = \mathfrak{n}_0 + \frac{1}{2\sqrt{3}} r_{41}\mathfrak{n}_0^3\mathcal{E},$$
$$\mathfrak{n}_{x'_3}(\mathcal{E}) = \mathfrak{n}_0 - \frac{1}{\sqrt{3}} r_{41}\mathfrak{n}_0^3\mathcal{E}, \tag{2.47}$$

so the originally isotropic crystal has turned into the uniaxial one under the applied electric field. In the other words, the index ellipsoid has turned from the sphere into the rotational ellipsoid with the main (optic) axis parallel to the electric field vector $\mathbf{E} = \mathcal{E}\sqrt{3}\,[1,1,1]$ (fig.2.9). Both refractive indices are independent on the direction of a wave vector in $x'_1 x'_2$ plane perpendicular to the main axis x'_3. Eq.2.41 describes a non-rotational ellipsoid with three principal axis that correspond to three main values of refractive indices. In general, it is a biaxial ellipsoid and it turns to the uniaxial if the electric field is perpendicular to the plane (111).

The alternative way how to get the same change of the refractive index $\Delta\mathfrak{n} = \Delta\mathfrak{n}(\alpha_1,\alpha_2,\alpha_3;\mathcal{E}_1,\mathcal{E}_2,\mathcal{E}_3)$ as described in eq.2.47 from the index ellipsoid (eq.2.41) is to use the direction cosines [92] $\alpha_i = a_i/|\mathbf{a}|$ of the allowed polarization for given direction of propagation $\mathbf{a} = [a_1,a_2,a_3]$ and the specified electric field $\mathbf{E} = \mathcal{E}\,[\beta_1,\beta_2,\beta_3]$. Using $x_i = (\mathfrak{n}_0 + \Delta\mathfrak{n})\,\alpha_i$, normalizing conditions $\sum_i \alpha_i\alpha_i = 1$, $\sum_i \beta_i\beta_i = 1$ and neglecting small values of $(\Delta\mathfrak{n})^2$ and $r_{41}\Delta\mathfrak{n}$, the index ellipsoid from eq.2.41 is rewritten as

$$\left(\mathfrak{n}_0^2 + 2\mathfrak{n}_0\Delta\mathfrak{n}\right)\left[\frac{1}{\mathfrak{n}_0^2} + 2r_{41}\mathcal{E}\left(\beta_1\alpha_2\alpha_3 + \beta_2\alpha_3\alpha_1 + \beta_3\alpha_1\alpha_2\right)\right] \approx 1, \tag{2.48}$$

so that change of the refractive index $\Delta\mathfrak{n}$ is

$$\Delta n \approx -\mathfrak{n}_0^3 r_{41}\mathcal{E}\left(\beta_1\alpha_2\alpha_3 + \beta_2\alpha_3\alpha_1 + \beta_3\alpha_1\alpha_2\right). \tag{2.49}$$

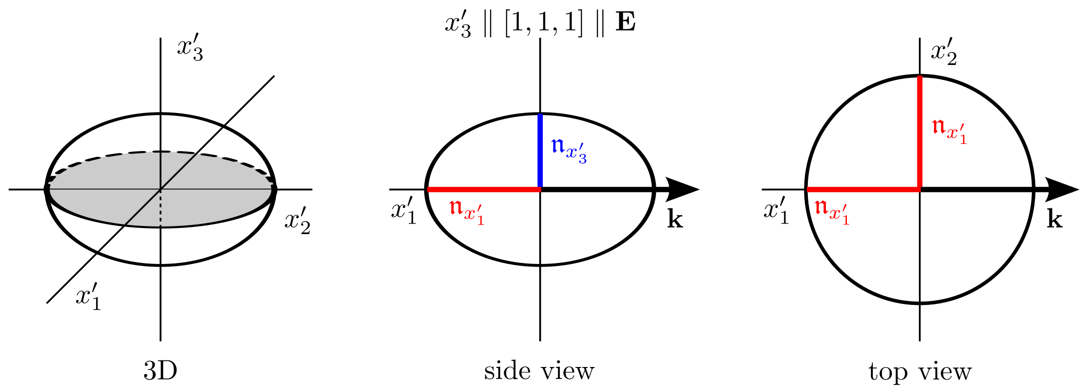

Figure 2.9: Rotational index ellipsoid with the main (optic) axis parallel to the electric field vector $\mathbf{E} = \mathcal{E}\sqrt{3}\,[1,1,1]$.

Now let usconsider the polarization $\mathbf{a}_{\|} = 1/\sqrt{3}[1,1,1]$ parallel to the electric field $\mathbf{E} = \mathcal{E}\sqrt{3}\,[1,1,1]$ (see fig.2.10a). Using eq.2.49, the change of the refractive index $\Delta\mathfrak{n}_{\|}$ is then

$$\Delta\mathfrak{n}_{\|} = -\frac{1}{\sqrt{3}} r_{41}\mathfrak{n}_0^3\mathcal{E}, \tag{2.50}$$

that corresponds to the change of the refractive index in the x'_3 direction from eq.2.47.

Now it will be shown how to get the change of the refractive index $\Delta\mathfrak{n}_{\perp}$ for the polarization $\mathbf{a}_{\perp}$ perpendicular to the applied electric field $\mathbf{E} = \mathcal{E}\sqrt{3}\,[1,1,1]$ (see fig.2.10b) and proof that $\Delta\mathfrak{n}_{\perp}$ is independent on the direction of propagation (wave vector) $\mathbf{k}$ of the plane wave that is perpendicular to $\mathbf{E}$.

From spatial arrangement of vectors $\mathbf{E}$, $\mathbf{k}$ and $\mathbf{a}_{\perp}$ as described above and using the condition $a_{\perp 1} \equiv 1$, one can get the following

$$\begin{aligned}
\mathbf{k}\cdot\mathbf{E} = 0 \quad &\Rightarrow \quad \mathbf{k} = \left[k_1, k_2, -(k_1+k_2)\right], \\
\mathbf{a}_{\perp}\cdot\mathbf{E} = 0 \quad &\Rightarrow \quad \mathbf{a}_{\perp} = \left[a_1, a_2, -(a_1+a_2)\right], \\
\mathbf{a}_{\perp}\cdot\mathbf{k} = 0 \quad &\Rightarrow \quad \mathbf{a}_{\perp} = \left[1, -(2k_1+k_2), \frac{k_1-k_2}{k_1+2k_2}\right], \\
|\mathbf{a}_{\perp}| &= 6\cdot\frac{k_1^2+k_1k_2+k_2^2}{k_1^2+4k_1k_2+4k_2^2}.
\end{aligned} \tag{2.51}$$

Direction cosines of the polarization $\alpha_{\perp i}$ are

$$\begin{aligned}
\alpha_{\perp 1} &= \frac{1}{|\mathbf{a}_{\perp}|}, \\
\alpha_{\perp 2} &= \frac{-1}{|\mathbf{a}_{\perp}|}\cdot\frac{2k_1+k_2}{k_1+2k_2}, \\
\alpha_{\perp 3} &= \frac{1}{|\mathbf{a}_{\perp}|}\cdot\frac{k_1-k_2}{k_1+2k_2}.
\end{aligned} \tag{2.52}$$

Using eqs.2.49 and 2.52, the change of the refractive index $\Delta\mathfrak{n}_{\perp}$ is

$$\Delta\mathfrak{n}_{\perp} = \frac{1}{2\sqrt{3}} r_{41}\mathfrak{n}_0^3\mathcal{E}, \tag{2.53}$$

that corresponds to the change of the refractive index in the x'_1 and x'_2 directions in eq.2.47 and it is independent on the direction of $\mathbf{k}$ if $\mathbf{k}\perp\mathbf{E}$.

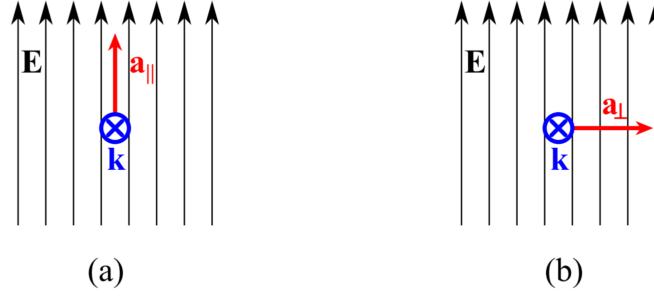

Figure 2.10: Spatial arrangement of vectors **E**, **a** and **k**.

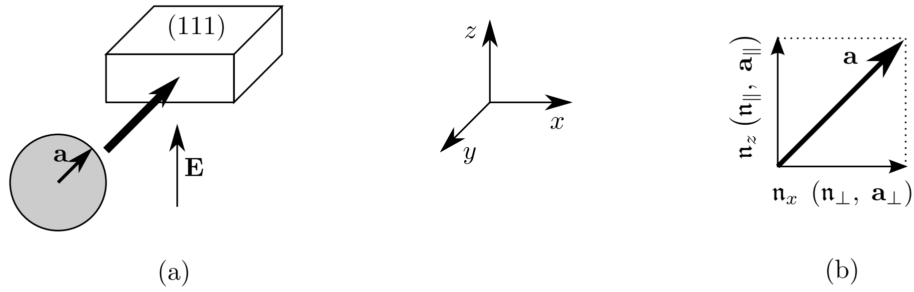

Figure 2.11: Schematics of the direction of the linearly polarized light incident into the crystal (a) and the decomposition of the linearly polarized beam into two modes (b).

2.8.3 Electric field reconstruction

For an easier notation and consistency with section 2.8.1 we can rename x'_1, x'_2 and x'_3 axes (from previous section 2.8.2) to x, y and z respectively.

Now let us consider the electric field **E** applied in the z-direction perpendicular to the (111) plane of the crystal. The linearly polarized light beam passes through the crystal in the y-direction and the direction of the polarization **a** rotated 45° about the z axis as shown on fig.2.11a. It is possible to decompose the incident polarization **a** into two independent modes corresponding to the x and z directions (fig.2.11b). Using eq.2.47, the mutual phase shift Γ of these modes is

$$\Gamma = k_0 \left[\mathfrak{n}_x(\mathcal{E}) - \mathfrak{n}_z(\mathcal{E})\right] L = \frac{2\pi}{\lambda_0}\frac{\sqrt{3}}{2} r_{41}\mathfrak{n}_0^3\mathcal{E}L, \tag{2.54}$$

where L is the optical path length.

The transmittance $\mathcal{T}$ of the system consisting of the crystal under the applied electric field placed between two crossed polarizers using eqs.2.32 and 2.54 is

$$\mathcal{T} = \sin^2\left(\frac{\sqrt{3}}{2}\frac{\pi r_{41}\mathfrak{n}_0^3\mathcal{E}L}{\lambda_0}\right). \tag{2.55}$$

Finally, the electric field distribution[7] $\mathcal{E}(x,z)$ can be written as a function of the transmittance[8] $\mathcal{T}(x,z)$ as

$$\mathcal{E}(x,z) = \frac{2}{\sqrt{3}} \frac{\lambda_0}{\pi r_{41} \mathfrak{n}_0^3 L} \arcsin \sqrt{\mathcal{T}(x,z)}. \tag{2.56}$$

Note: It is convenient for further calculations to rewrite both constant parameters and optical path length L from eqs.2.55 and 2.56 into the parameter α_P characterizing the particular sample in the following way

$$\alpha_P = \frac{\sqrt{3}}{2} \frac{\pi r_{41} \mathfrak{n}_0^3 L}{\lambda_0}, \tag{2.57}$$

so eqs.2.55 and 2.56 can be rewritten in a simple way as

$$\mathcal{T}(x,z) = \sin^2 \left[\alpha_P \mathcal{E}(x,z)\right] \tag{2.58}$$

and

$$\mathcal{E}(x,z) = \frac{\arcsin \sqrt{\mathcal{T}(x,z)}}{\alpha_P} \tag{2.59}$$

respectively.

2.9 Thermal emission of charge carriers from defect levels into bands

Thermal emission rates of electrons $e_n(T)$ and holes $e_p(T)$ from a level E_t into the conduction and the valence band, respectively are written as

$$\begin{aligned} e_n(T) = \tau_e^{-1}(T) = \sigma_n v_e^{th} N_c \, \mathrm{e}^{-\frac{E_c - E_t}{k_B T}}, \\ e_p(T) = \tau_h^{-1}(T) = \sigma_p v_h^{th} N_v \, \mathrm{e}^{-\frac{E_t - E_v}{k_B T}}, \end{aligned} \tag{2.60}$$

[7] The distribution of the electric field through the samples is generally non-uniform in directions, so that it is more correct to use its spatial distribution $\mathcal{E}(x,z)$ instead of the simple $\mathcal{E}$. The same reason is for the transmittance $\mathcal{T}(x,z)$. It is impossible to study the electric field distribution in the y direction due to the nature of the experiment, but if the electric field lines are parallel to the z axis with the presumption that the crystal is homogeneous, the electric field should be uniform in both x and y directions.

[8] In the real experiment, the maximal transmittance $\mathcal{T}$ of the described system is smaller than the unity because of the reflection, absorption, scattering and misalignments [87]. These aspects are discussed later in experimental part (section 3.5).

where τ_e and τ_h are the time constants of emissions of electrons and holes (also called de-trapping times[9]), respectively. The effective density of states for electrons in the conduction band N_c and for holes in the valence band N_v is

$$N_{c(v)} = 2\left(\frac{2\pi m^*_{e(h)} k_B T}{h^2}\right)^{3/2} \tag{2.61}$$

and the thermal velocities are

$$v^{th}_{e(h)} = \sqrt{\frac{8k_B T}{\pi m^*_{e(h)}}}, \tag{2.62}$$

where m^*_e and m^*_h are the effective masses[10]of electrons and holes, respectively.

2.9.1 De-trapping and the electric field

Now let us consider the applied bias to an n-type CdZnTe with contacts bending bands upwards. Electrons are de-trapping from the deep donor level near the cathode within depletion width L_d. In this process, the deep level is positively ionized with a de-trapping time τ_e described by eq.2.60.

When the bias is applied at the time $t = 0$, the concentration of the ionized deep donor n_t^+ ($n_t^+ = N_t - n_t$) grows as

$$\Delta n_t^+(t) = N_t\left(1 - \mathrm{e}^{-\frac{t}{\tau_e}}\right). \tag{2.63}$$

The electrostatic potential $\varphi(x,t)$ can be obtained by solving the one-dimensional Poisson's equation (eq.2.10) as

$$\frac{d^2\varphi(x,t)}{dx^2} = \frac{e\Delta n_t^+(t)}{\epsilon} = \frac{eN_t}{\epsilon}\left(1 - \mathrm{e}^{-\frac{t}{\tau_e}}\right), \tag{2.64}$$

where x is the distance from the M-S interface (cathode).

According to the conventional polarization models [2, 6, 11, 94–96] the bias was considered to be developed across the whole sample between electrodes. It is supposed in this work, that almost all the bias voltage develops across the depletion layer L_d. Therefore, the distribution of the electric field $\mathcal{E}(x,t) = -d\varphi/dx$ within the depletion region can be obtained by solving eq.2.64 with the following boundary conditions

$$\begin{aligned} \varphi(0) &= U \\ \varphi(L_d) &= U_{12}, \end{aligned} \tag{2.65}$$

[9] Do not confuse carriers de-trapping time $\tau_{e(h)}$ with their life-time $\tau_{n(p)}$.

[10] $\frac{m^*_e}{m_e} = 0.096$ and $\frac{m^*_h}{m_e} = 0.83$ according to [93].

where U_{12} is the part of the external applied voltage that develops across the bulk semiconductor and the forward bias contact (anode) and $U_{12} \ll U$ [97]. Then

$$\mathcal{E}(x,t) = \begin{cases} \frac{eN_t}{\epsilon}\left(1-\mathrm{e}^{-\frac{t}{\tau_e}}\right)(L_d - x) + \mathcal{E}_0 & 0 \le x \le L_d, \\ \mathcal{E}_{12} + \mathcal{E}_0 & x > L_d, \end{cases} \tag{2.66}$$

where $\mathcal{E}_0$ is the initial electric field at the M-S interface due to the contact potential V_{bi} ($V_{bi} = \Phi_{metal} - \Phi_{semicond.}$) and $\mathcal{E}_{12} = U_{12}/(d - L_d)$, where d is the sample thickness. The depletion width L_d is given by

$$L_d = \sqrt{\frac{2\epsilon U}{eN_t\left(1-\mathrm{e}^{-\frac{t}{\tau_e}}\right)}}. \tag{2.67}$$

Using equations 2.66 and 2.67 we get

$$\begin{aligned} \mathcal{E}(x,t) &= \sqrt{2\gamma U} - \gamma x + \mathcal{E}_0 \qquad 0 \le x \le L_d, \\ \text{where} \qquad \gamma &= \frac{eN_t}{\epsilon}\left(1-\mathrm{e}^{-\frac{t}{\tau_e}}\right). \end{aligned} \tag{2.68}$$

The electric field profile linearly decreases with the distance from the cathode. Eq.2.68 at $x = 0$ (just below the cathode) gives

$$\mathcal{E}(0,t) = \sqrt{2\gamma U} + \mathcal{E}_0. \tag{2.69}$$

2.9.2 Deep level parameters

Using a standard approach of the Arrhenius analysis of time constants by linearization of eq.2.60 we get[11]

$$\ln\left(\tau_{e(h)}T^2\right) = \frac{E_A}{k_B T} - \ln\left(\sigma_{n(p)}A_{e(h)}\right), \tag{2.70}$$

where

$$A_{e(h)} = \frac{16\pi m^*_{e(h)}k_B^2}{h^3}. \tag{2.71}$$

Arrhenius plot of $\ln\left(\tau_{e(h)}T^2\right)$ versus $1/(k_B T)$ creates a straight line with the *slope* equal to the activation energy E_A and the *intersection* with the "$\ln\left(\tau_{e(h)}T^2\right)$" axis can be used for the calculation of capture cross-sections $\sigma_{n(p)}$:

[11] $E_c - E_t$ and $E_t - E_v$ from eq.2.60 are interchanged with activation energy E_A.

$$E_A = slope,$$
$$\sigma_{n(p)} = \frac{\mathrm{e}^{-intersection}}{A_{e(h)}}. \tag{2.72}$$

The type of the trap (electron or hole) can be determined based on the knowledge of the band bending at M-S interface that is discussed in chapter 5.

The dependence of the electric field on $\sqrt{U}$ at any point x within the depletion region ($0 \leq x \leq L_d$) should be a straight line with the slope $\sqrt{2\gamma}$ (see eq.2.68). Therefore, the deep level concentration N_t can be determined.

The electric field under the cathode may be properly assessed by the measurements of current transients. Assuming the standard diffusion model of contacts [97], where the free carrier density n is given by the Schottky barrier that is independent on the bias and the constant electron mobility μ_n, the electric current density j is

$$j = e\mu_n n\mathcal{E}(0,t). \tag{2.73}$$

Therefore, the current increase with time is a consequence of the increase of the electric field at the cathode $\mathcal{E}(0,t)$. The time domains of j and $\mathcal{E}(0,t)$ should be correlated.

Chapter 3

Experimental

3.1 Pockels effect

Experimental setup used for Pockels effect measurements (see fig.3.1) consists of the source of collimated light beam (tungsten lamp and lenses), bandpass filter with a central wavelength at 980 nm, two NIR polarizers, closed-cycle cryostat `Leybold` (equipped with `SQ1` quartz glass windows) acting as a holder and electromagnetic shield and 256-bit NIR InGaAs CMOS camera `Xenics Xeva` equipped with 10x zoom lens. Sourcemeter `Keithley 2400` is used to apply the voltage on the samples[1].

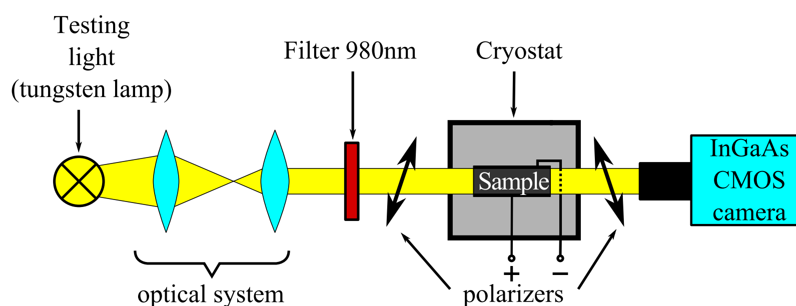

Figure 3.1: Experimental setup for Pockels effect measurements.

The following information about the samples, applied voltage and any other variable parameters are general. Individual parameters are discussed later in chapter 4.

In general, the sample thickness d is in the range of $1-2.5$ mm and the area varies between $5\times5-10\times10$ mm^2. Contact metals (electrodes) were deposited

[1]The similar setup, but with different devices (i.e. 8-bit Si CCD camera, `Ortec` voltage source, etc.), was used in 2010 for the electric field measurements under hi-flux X-rays at Department of Physics, University of Surrey. According that setup, the new one was built at Charles University. In this section only the setup which is presented at Charles University is described.

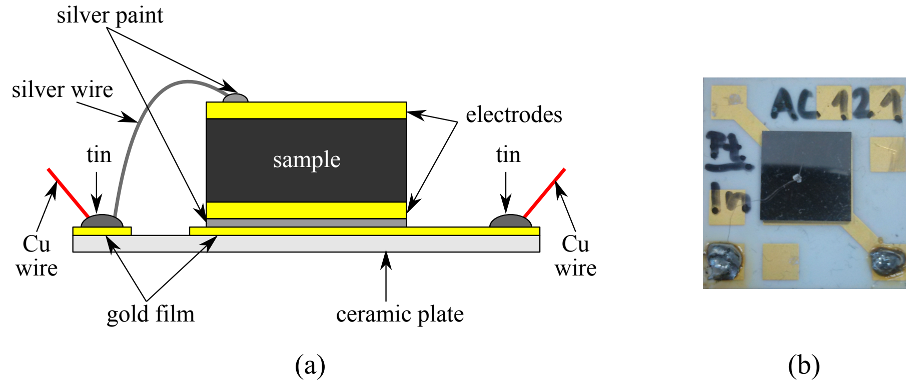

Figure 3.2: (a) Sample holder schematics (not in scale). Copper wires lead to the BNC cable which leads to the sourcemeter. (b) Top view of ceramic plate (area 24×24 mm^2) with mounted sample (area 10×10 mm^2) without copper wires.

by evaporation (Au, In) on large sample surfaces that correspond to the plane (111).

The sample holder is shown on fig.3.2. The sample is fixed with its bottom contact to a gold film of a thermoconductive ceramic plate using a silver paint. A silver wire with a thickness 0.05 mm is also fixed by the silver paint to the top contact of the sample and leads to another separated gold film where it is fixed by a soldering by tin. Two copper wires are soldered to both gold films and lead to a `BNC` cable and then to the `Keithley 2400` sourcemeter. The sample holder is mounted to a copper coldfinger of the closed-cycle cryostat by a thermoconductive paste.

Thermoelectric cooler (TEC) was used for temperature dependent measurements and to avoid the shaking during cold helium pumping in the closed-cycle cryostat. This shaking has a negative influence on the quality of images acquired during Pockels effect measurements. Standard TEC for CPU was controlled by `Eurotherm 3504` thermoregulator. The range of measuring temperatures was of approx. 285 and 320 K.

The bandpass filter with central wavelength[2] at $\lambda_0 = 980$ nm is used to obtain a quasi-monochromatic light. Transmission spectrum of the filter is shown on fig.3.3. The studied material shows a good transparency, low photocurrent and the quantum efficiency of InGaAs CMOS camera is relatively high (about 60%) at the wavelength of 980 nm.

Camera `Xenics Xeva` equipped with InGaAs chip with resolution 320×256 sq. pixels and three-stage Peltier cooling (down to about 220 K to avoid camera dark noise) was used for capturing the images of the transmitted light intensity through the sample placed between two crossed polarizers. The window of the program `X-Control` used for controlling the camera and saving the images is

[2]The bandpass filter with the same wavelength was used during similar Pockels effect measurements at the University of Surrey.

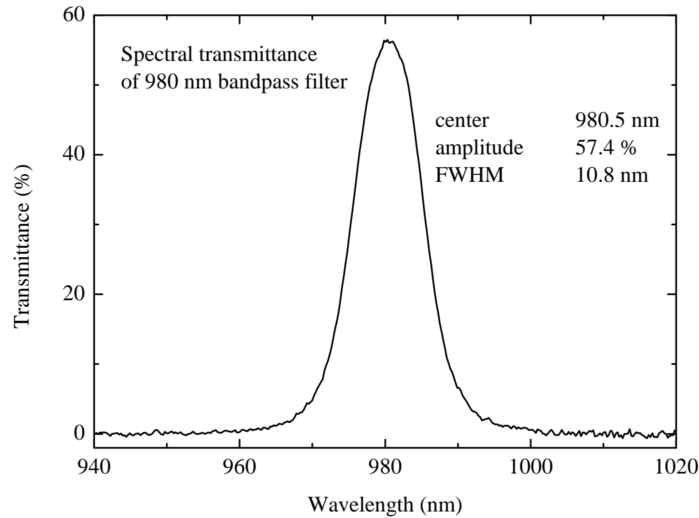

Figure 3.3: Transmission spectrum of bandpass filter with central wavelength at 980 nm measured by spectrometer `Ocean Optics HR4000`.

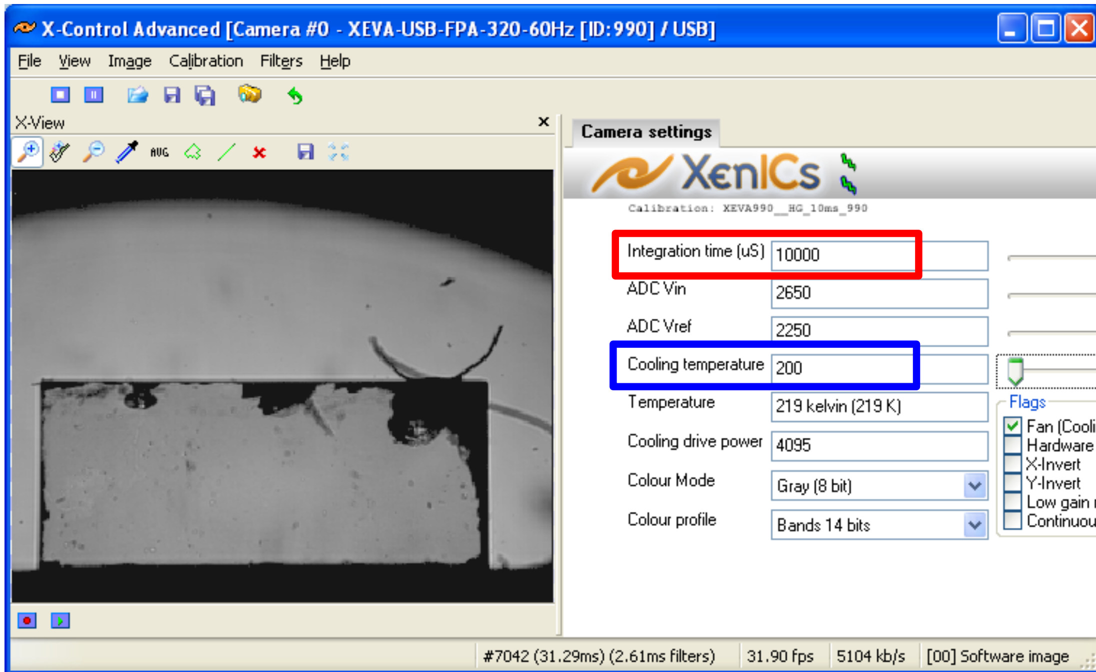

Figure 3.4: `X-Control` program window for capturing the images from camera. Typical front-side view of the sample (rectangle in the left image window) without applied voltage if the polarizers are parallel (maximum transmitted intensity). Dark regions on the right and upper parts of the sample are caused by damaged surface of the sample. Integration time and camera chip cooling temperature settings are highlighted in red and blue boxes respectively.

shown on fig.3.4. It is sometimes necessary to change the integration time of the camera due to the different intensity of pictures so it was also necessary to check the linear dependency of brightness of acquired pictures on different conditions for further data analysis. The measured linearity of the intensity acquired by

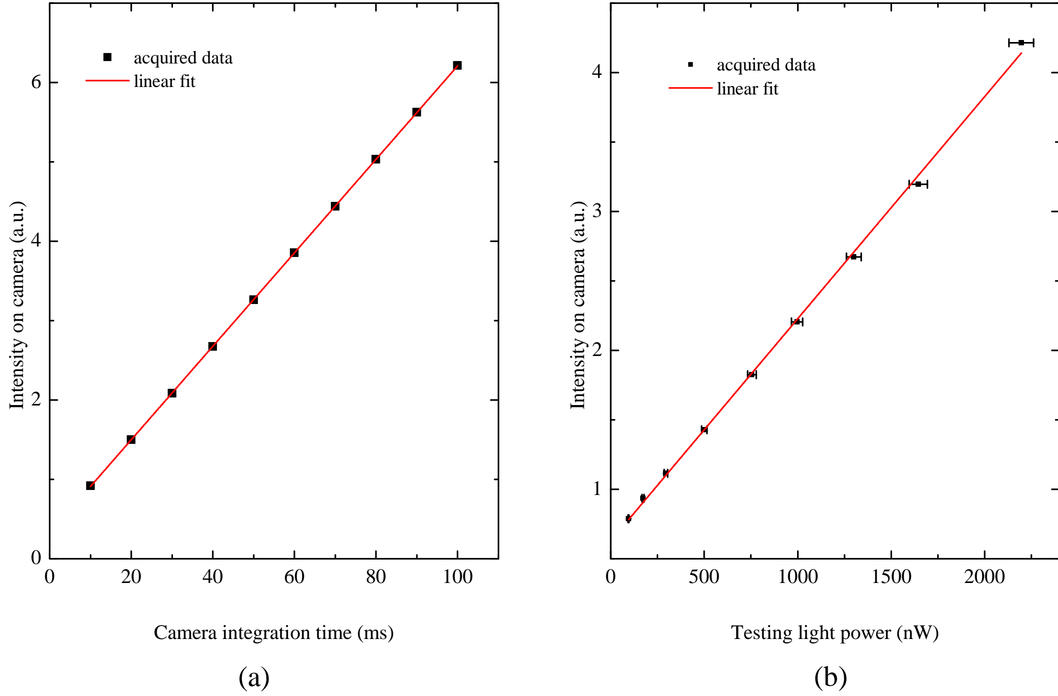

Figure 3.5: Linearity of the sensitivity of InGaAs camera. Light intensity acquired by camera (intensity on camera) was calculated as an averaged number of counts from 50×50 pixels area. Errors of the camera integration time and the recorded intensity are negligible. (a) Intensity recorded by the camera dependent on the integration time. (b) Recorded intensity dependent on the testing light power at the integration time 50 ms. The relative error of the testing light power ($\lambda_0 = 980$ nm) measured by the power meter `Ophir vega` was estimated to be 3%.

camera against the integration time[3] is shown on fig.3.5a. The dependence of the intensity acquired by camera on the incident light intensity shown on fig.3.5b is also linear.

3.1.1 Advanced setup

X-ray tube and tunable laser were used to study internal processes in CdTe based detector samples under high-flux conditions during Pockels effect measurements (fig. 3.6). Ag-target X-ray tube powered up to 50 kV/500 μA was used as high-flux X-rays source for the sample excitation at University of Surrey. Incident X-ray radiation was mostly absorbed by the samples [34]. Tunable Titanium:Sapphire CW Laser (`Newport corp. 3900S`) pumped with 532 nm diode-pumped Nd: YAG laser was used as a high-flux well defined light source at Charles University. The range of used wavelengths was of 700 and 1000 nm and it was possible to change the depth of penetration due to the different absorption coefficient (see fig.1.1). Laser output intensity was controlled by the power meter `Ophir Vega` equipped with a silicon photo diode.

The near infra-red monochromatic beam was used in addition to excitation

[3] The used range of camera integration times during the measurements was of 10 and 70 ms.

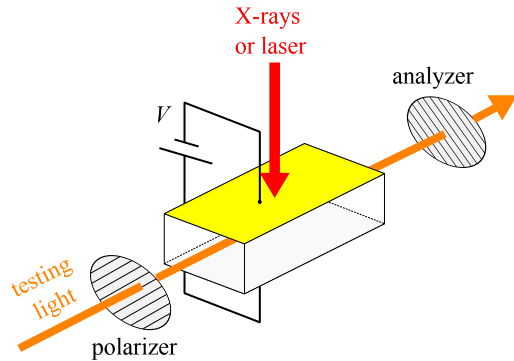

Figure 3.6: Setup configuration for X-ray or laser excitation.

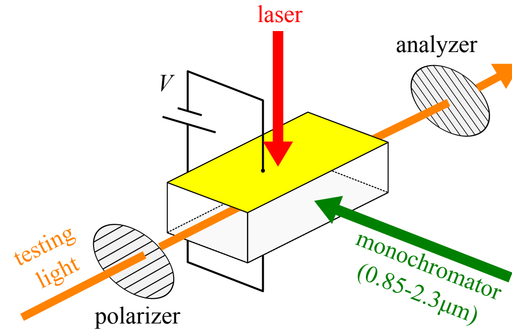

Figure 3.7: Setup configuration for laser excitation and perpendicular infrared beam of monochromator.

beam for study the dependency of the electric field on changes of an occupation of the deep levels. 50 W halogen lamp and monochromator `Karl-Zeiss SPM2` equipped with lithium fluoride optical prism was used for generation of infrared radiation with wavelengths in the range of 850 and 2300 nm. The beam from the monochromator illuminated the sample perpendicular with respect to the applied electric field and the testing light (fig. 3.7).

3.1.2 Data acquisition and analysis

To analyze the electric field distribution $\mathcal{E}(x, z)$ through the sample it is necessary to find the correct distribution of the transmittance $\mathcal{T}(x, z)$ (see eq.2.59) of the biased sample placed between two crossed polarizers. The intensity of transmitted testing light distributions $\mathcal{I}(x, z)$ was taken by the camera for different conditions that are described in the table 3.1.

Intesity	Polarizers	Voltage	Light	Int. time	Fig.3.8b
$\mathcal{I}^{\times}_{bias}(x, z)$	crossed (CP)	non-zero	ON	$t_i^{\times}$	4, 5
$\mathcal{I}^{\times}_{bcg}(x, z)$	crossed (CP)	zero	ON	$t_i^{\times}$	3
$\mathcal{I}^{\parallel}_{0}(x, z)$	parallel (PP)	zero	ON	$t_i^{\parallel}$	1
$\mathcal{I}^{\parallel}_{bcg}(x, z)$	parallel (PP)	zero	OFF	$t_i^{\parallel}$	2

Table 3.1: Description and conditions of measured intensity distributions of the light passing through the sample placed between two crossed polarizers. $t_i^{\times}$ and $t_i^{\parallel}$ are the integration times set on the camera for crossed and parallel polarizers modes, respectively.

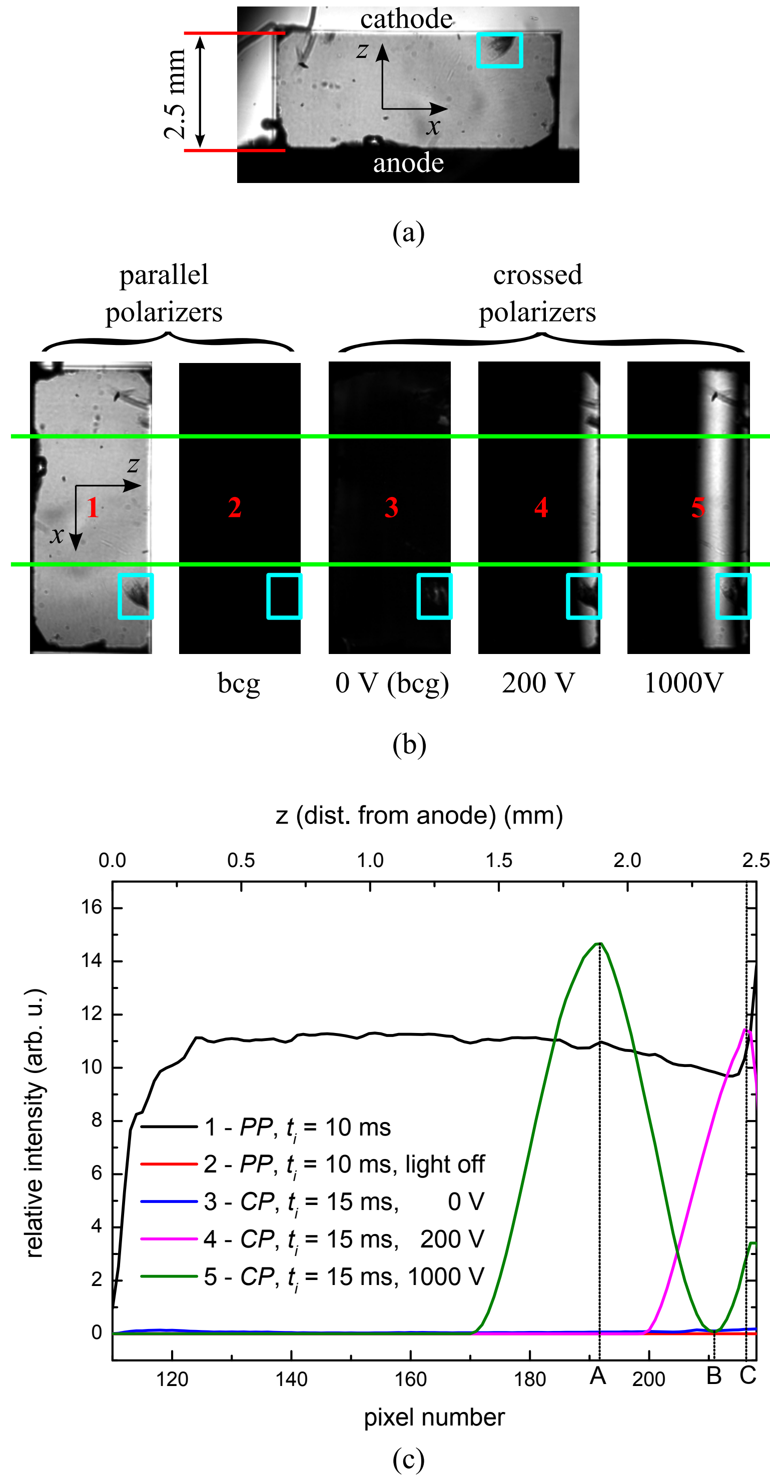

Figure 3.8: Outline of data analysis. (a) Image of 2.5 mm thick sample, camera integration time $t_i = 10$ ms, parallel polarizers (PP). (b) Cropped (sample area only) and clockwise turned (about 90°) images of the sample at following conditions: 1 - PP, $t_i = 10$ ms and zero voltage. 2 - PP, $t_i = 10$ ms, zero voltage and the testing light turned off. 3 - crossed polarizers (CP), $t_i = 15$ ms and zero voltage. 4 - CP, $t_i = 15$ ms and voltage 200 V. 5 - CP, $t_i = 15$ ms and voltage 1000 V. Cyan boxes show the area of one of the surface defects. Average of the distribution of transmitted light intensity between electrodes $\mathcal{I}(z)$ was taken from the area between two green lines. (c) Distribution of the average light intensity through the sample between electrodes for all cases mentioned in (b). Intensity is nearly zero for "2"and "3". "A"and "B"points are the positions of the maximum and the minimum of transmitted intensity for applied voltage 1000V respectively. Between point "C"and the cathode the quality of acquired signal is very low due to the bad surface of the sample. Thickness of this layer is estimated to 50 μm and varies due to the particular sample. So for this part of the sample it is impossible to calculate the electric field properly. Similar situation appears also under the anode.

It is obvious[4] that the transmittance distribution $\mathcal{T}(x,z)$ is calculated as

$$\mathcal{T}(x,z) = \frac{\left[\mathcal{I}^{\times}_{bias}(x,z) - \mathcal{I}^{\times}_{bcg}(x,z)\right] t_i^{\times}}{\left[\mathcal{I}^{\|}_{0}(x,z) - \mathcal{I}^{\|}_{bcg}(x,z)\right] t_i^{\|}}. \tag{3.1}$$

With the presumption that the crystal is homogeneous and the electric field lines are parallel to the z-axis (as described in section 2.8.3), $\mathcal{T}(x,z)$ becomes $\mathcal{T}(z)$ and it is possible to average the intensity in the x direction. Images acquired by the camera are saved to a `.bmp` file, that is converted to a data file in which each pixel is recorded with its intensity in 24-bit gray scale. The area of the averaging is shown on fig. 3.8b between two green lines and the part of the sample with no or very few surface defects is usually chosen.

For the case of highly polarized samples[5] it can quite easily happen that the electric field is sufficiently high that the argument of sinus from eq.2.58 reaches value $\pi/2$ (corresponding electric field $\mathcal{E}_{\frac{\pi}{2}}$) and the transmittance $\mathcal{T}(z)$ (also $\mathcal{I}^{\|}_{0}(z)$) reaches its maximum and then it is decreasing until the argument equals to π (corresponding electric field $\mathcal{E}_{\pi}$). Then the transmittance is again increasing and so on as described on fig.3.9. The described situation corresponds to the measured intensity shown on fig.3.8b-5 and c-5.

It is obvious that eq.2.59 is valid only for $\mathcal{E}(z) \in \langle 0, \mathcal{E}_{\frac{\pi}{2}}\rangle$ where the transmittance $\mathcal{T}(z)$ is a monotonic function of the electric field $\mathcal{E}(z)$ according to eq.2.58 (see fig.3.9). Using simple considerations it is possible to get a formula for the electric field calculation for a wider interval, so the eq.2.59 (using $\mathcal{T}(x,z) \Rightarrow \mathcal{T}(z)$) becomes:

$$\mathcal{E}(z) = \begin{cases} \dfrac{\arcsin\sqrt{\mathcal{T}(z)}}{\alpha_P} & \text{for } \mathcal{E}(z) \in \langle 0, \mathcal{E}_{\frac{\pi}{2}}\rangle, \quad \text{(a)} \\[2ex] \dfrac{\arcsin\left[-\sqrt{\mathcal{T}(z)}\right] + \pi}{\alpha_P} & \text{for } \mathcal{E}(z) \in \langle \mathcal{E}_{\frac{\pi}{2}}, \mathcal{E}_{\pi}\rangle, \quad \text{(b)} \\[2ex] \dfrac{\arcsin\sqrt{\mathcal{T}(z)} + \pi}{\alpha_P} & \text{for } \mathcal{E}(z) \in \langle \mathcal{E}_{\pi}, \mathcal{E}_{\frac{3}{2}\pi}\rangle. \quad \text{(c)} \end{cases} \tag{3.2}$$

Calculated electric fields for acquired intensities from fig.3.8c-4 and 5 are shown on fig.3.10.

[4]It is necessary to subtract corresponding "bcg" intensities because of a non zero intensity of the "background" images caused by a thermal noise of the camera or a residual reflectivity or scattering of the testing light on surface defects and sample surfaces caused by a misalignments of the setup, that is very difficult to avoid. It is also necessary to use different integration times t_i for both parallel and crossed polarizers modes to get sufficiently bright images and on the other hand do not overflow camera pixels.

[5]A space charge occurs at the blocking contact. The electric field forms dead layer ($\mathcal{E} = 0$ and that $\mathcal{I} = 0$ and $\mathcal{T} = 0$) close to the opposite contact and relatively high electric field develops close to the blocking contact.

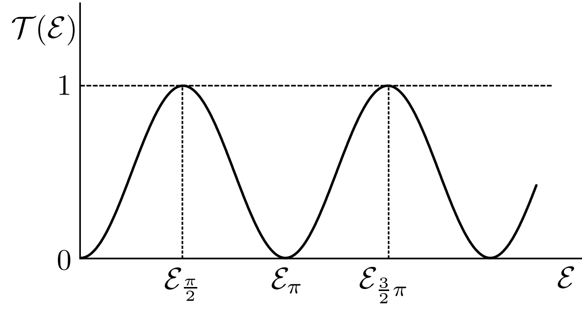

Figure 3.9: Dependence of the transmittance of the biased sample placed between two crossed polarizers on the applied electric field according to eq.2.58. Conditions: $\alpha_P \mathcal{E}_{\frac{\pi}{2}} = \pi/2$, $\alpha_P \mathcal{E}_{\pi} = \pi$ and $\alpha_P \mathcal{E}_{\frac{3}{2}\pi} = 3\pi/2$.

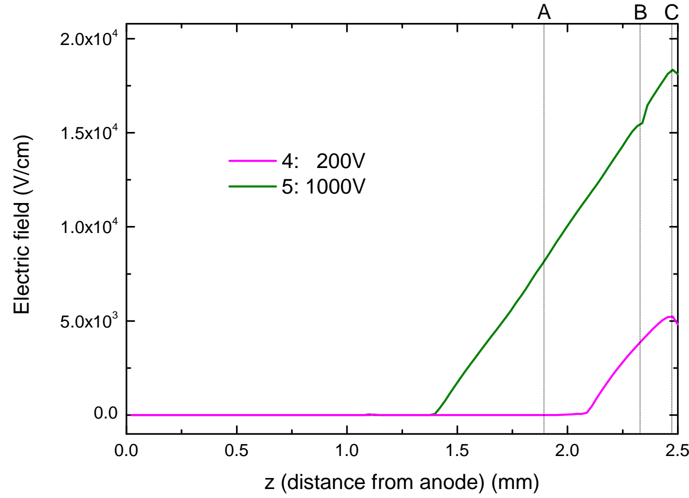

Figure 3.10: Calculated electric field.

3.2 Photoconductivity measurements

Fundamentals of photoconductivity measurements, especially photocurrent spectra and lux-Ampere characteristics, are briefly described in this chapter.

Incident radiation changes the bulk conductivity of semiconductors. This phenomenon is called photoconductivity[6] and it can be divided into two types: the intrinsic photoconductivity is associated with a band-to-band generation of mobile charge carriers (electrons and holes) by absorption of photons, while the extrinsic photoconductivity is associated with the presence of impurities, when the electrons (holes) related to the impurity energy level are excited to the conduction (valence) band and become the mobile charge carriers [98, chap. 7].

Typical behavior of a photocurrent spectrum of a direct bandgap semiconductor close to the absorption edge is shown on fig.3.11.

[6] The conductivity of semiconductors is usually increasing with an increasing incident irradiation intensity. The opposite effect (decreasing conductivity) is called "negative photoconductivity" [98, chap. 1].

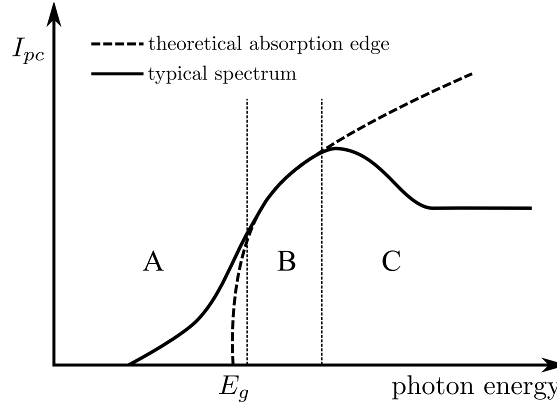

Figure 3.11: Photocurrent spectrum (direct transition): schematic drawing of the dependence of the photocurrent I_{pc} on photon energy close to the bandgap energy E_g. Dashed curve shows the theoretical absorption edge ($I_{pc} \sim \sqrt{E}$). The ealistic photocurrent spectrum (solid line) of CdTe and CdZnTe detector materials near the absorption edge can be divided into three parts: exponential increase (Urbach edge) below E_g (part A), square root dependence (part B) and the decrease of the photocurrent (part C) due to a surface recombination. The observed maximum of photocurrent is usually called the photocurrent peak or simply the photopeak.

3.2.1 Experimental setup

The electrical circuit used for photocurrent measurements is shown on fig.3.12. It consists of DC voltage power supply (sourcemeter `Keithley 2410`), detector sample, serial 100 MΩ resistor R_C and electrometer `Keithley 6514`. The sample was mounted inside of the closed-cycle cryostat `Leybold` (equipped with `SQ1` quartz glass windows). Tunable Titanium:Sapphire CW Laser (`Newport corp. 3900S`) pumped with 532 nm diode-pumped Nd: YAG laser was used as a well defined light source that can operate at high photon fluxes ($\Phi \sim 10^{11} - 10^{18}$ cm^{-2}s^{-1}). The range of used wavelengths was of 700 and 1000 nm. The laser intensity was controlled by a power meter `Ophir Vega` equipped with a silicon photo diode. The sample was illuminated through a semitransparent gold contact that was acting as a cathode parallel to the applied electric field.

All the measurements were performed at room temperature and in a mode of constant voltage on the sample U_S, when the sourcemeter output U_0 was set to a certain value to keep constant voltage on the sample U_S. The estimated error of the constant value U_S is less than 1%.

The voltage U_0 applied by the sourcemeter is divided to the sample (U_S) and the serial resistor (U_C) as

$$U_0 = U_S + U_C. \tag{3.3}$$

The electric current flowing through the circuit in the dark I_0 can be measured indirectly by measuring the voltage on the serial resistor with a known resistance R_C as

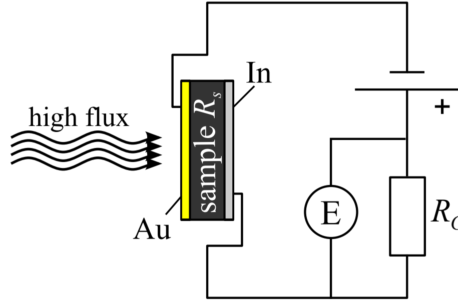

Figure 3.12: Schematics of the measuring circuit with the sample, serial resistor R_C and sourcemeter (`Keithley 2410`) used for photoconductivity measurements. Voltage on R_C was measured using `Keithley 6514` electrometer (E). The sample was illuminated using Titanium:Sapphire laser.

$$I_0 = \frac{U_C}{R_C}. \tag{3.4}$$

The electric current flowing through the circuit while the sample is illuminated I^* is increasing because the sample resistance R_S (conductivity) is decreasing (increasing) due to photogenerated carriers and the voltage U_S is decreasing. At this moment it is necessary to increase the voltage on the sourcemeter to keep the constant voltage on the sample. The current flowing through the circuit I^* is calculated as

$$I^* = \frac{U_C^*}{R_C}, \tag{3.5}$$

where U_C^* is the voltage on serial resistor while the sample is illuminated.

Finally, the photocurrent I_{pc} is the difference of both currents from eqs.3.5 and 3.4

$$I_{pc} = I^* - I_0 = \frac{U_C^* - U_C}{R_C} \tag{3.6}$$

and the photocurrent density j_{pc}

$$j_{pc} = \frac{U_C^* - U_C}{AR_C}, \tag{3.7}$$

where A is an illuminated area of the sample.

3.2.2 Lux-Ampere characteristics

Measurement of lux-Ampere characteristics is based on the measurement of photocurrent under different intensity (photon flux Φ) of irradiation at a particular wavelength of laser. Observed dependence can be written as

$$j_{pc} = b \cdot \Phi^\beta, \tag{3.8}$$

where b and β are constants. Using the linearization, eq.3.8 can be rewritten as

$$\log j_{pc} = \beta \cdot \log \Phi + const. \tag{3.9}$$

and it is called the lux-Ampere characteristic where β is its slope.

This dependence can be used for a qualitative estimation of the CCE (charge collection efficiency) of the detector. Linearity of the lux-Ampere characteristic (slope $\beta = 1$ in log-log scale) means that all the photogenerated charge is collected and CCE equals to 1. Sublinear lux-Ampere characteristics ($\beta < 1$) is a sign of the smaller CCE which means that not all of photogenerated charge carriers are collected because of the screening of the electric field due to a space charge accumulated at deep levels [75]. Thus photogenerated carriers can recombine in the region of the low electric field. This recombination is consistent with the Hall-Shockley-Read model.

3.3 Discharge current measurements

The so called *discharge current deep level transient spectroscopy* method which is based on a thermal emission of trapped charge carriers (see section 2.9) is introduced in this section. The method is based on a similar principle as PICTS [99], DLTS or I-DLTS [100].

It allows us to find an activation energy E_A of the thermal emission associated with the trap energy E_t, its type (electron or hole trap) and its capture cross-section $\sigma_{n(p)}$. This method exploits de-trapping processes during discharging of the metal-semiconductor-metal (M-S-M) structure. Band bending at the M-S interface that changes the type of the majority charge carriers is induced by applying the contact metals to samples with different work functions. The energies of the levels were calculated using time constants τ_i of the discharge current behavior at different temperatures.

3.3.1 Experimental setup

Before the measurement of the discharge current the sample was biased using sourcemeter `Keithley 2400`. After reaching the constant current, the sourcemeter was disconnected and the discharge current was measured by the electrometer `Keithley 6514`. The sample was mounted inside the cryostat. Schematic of the setup is shown on fig.3.13. Disconnection of the sourcemeter is represented with a two-position switch.

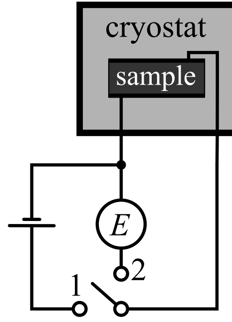

Figure 3.13: Experimental setup used for discharge current measurements. During the discharge current measurements the switch is set at the position '2'. 'E' indicates the electrometer `Keithley 6514`.

3.3.2 Analysis

After switching off the voltage the sample tends to achieve an equilibrium and the electric current due to the de-trapping of carriers from the deep level E_t can be measured by electrometer. The current decreases with time (see fig.3.14) and its dependence can be approximated by a double exponential (eq.3.10)

$$I(t) = I_0 + C_1 \exp\left(-\frac{t-t_0}{\tau^1_{e(h)}}\right) + C_2 \exp\left(-\frac{t-t_0}{\tau^2_{e(h)}}\right), \tag{3.10}$$

where de-trapping time constants $\tau^1_{e(h)}$ and $\tau^2_{e(h)}$ were obtained from double exponential fit of time evolution of discharge current measurement. Measurements were performed at different temperatures in the range of 280 K and 340 K.

Activation energy E_A and capture cross-section $\sigma_{n(p)}$ of the deep level can be calculated using standard approach of Arrhenius analysis described in section 2.9.2.

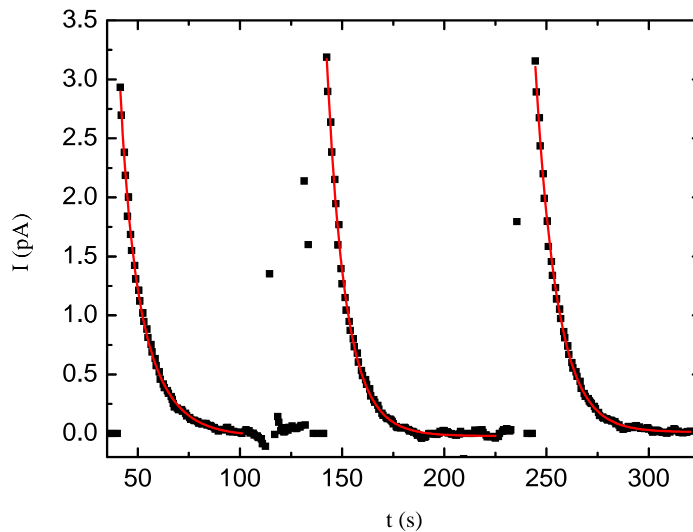

Figure 3.14: Discharge current measurements. Low resistivity CdZnTe sample ($\sim 3\times10^7\Omega$cm), T=300K, forward voltage 200 V. Red curves represent double-exponential fits of three consecutive measurements.

3.4 Samples

Three sets of CdTe and CdZnTe samples were used for the measurements. Samples were cut from monocrystalline parts of crystals using a wire saw. The sides of the samples were optically polished with final 0.05 μm grit and chemically etched in 1% Br–methanol solution for 1 minute. Contact metals (gold and indium) were deposited on large opposite sides by evaporation. Typical configuration of the sample is depicted on fig.3.15.

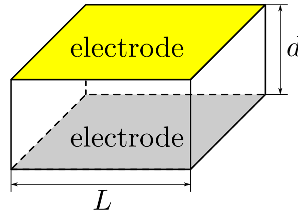

Figure 3.15: Planar sample configuration.

3.4.1 VGF CdTe:In - samples no.1 & 2

Samples no.1 and 2 were made of indium doped CdTe grown by VGF (Vertical Gradient Freeze) method in the Institute of Physics, Charles University in Prague. Two neighboring samples with the same crystallographic orientation cut from one grain were chosen because they were showing sufficient optical quality after optical polishing and sufficient Pockels effect. Optical polishing was made at Division of Optical Technology at Institute of Physics, Charles University.

Planar samples with dimensions approx. $5 \times 5 \times 1.65$ mm^3 were equipped with gold and indium contacts. The resistivity of the samples was $3-5\times10^9$ Ωcm. The crystal exhibits relatively good charge collection efficiency of electrons with a mobility-lifetime product $\mu\tau_e \sim 10^{-3}$ cm^2/V. Room temperature thermoelectric effect measurements have shown that samples are slightly n-type.

3.4.2 HPB CdZnTe - samples no.3 & 4

$Cd_{0.9}Zn_{0.1}Te$ planar detector samples with dimensions $5\times5\times2.5$ mm^3 were made of one grain of (111) oriented single crystal CZT grown by `eV products` company using High Pressure Bridgman method (HPB). The sample no.3 was equipped with indium and gold contacts, while the sample no.4 was equipped with both gold contacts. The studied CdZnTe samples were detector-grade with a mobility-lifetime product of electrons $\mu\tau_e \sim 1.5 \times 10^{-3}$ cm^2/V, resistivity 10^{10} Ωcm and with n-type conductivity.

3.4.3 VGF CdZnTe - sample no.5

Au/$Cd_{0.97}Zn_{0.03}Te$/Au sample was cut from (111) oriented single crystal grown by VGF method at Institute of Physics of Charles University. This crystal is non-detector grade but it is suitable for the polarization study.

The list of measured samples is shown in the table 3.2. The resistivity of the samples ρ was measured using a contactless method by the CoReMa system available at our department. Mobility-lifetime ($\mu\tau$) products were measured using alpha spectroscopy measurements. IR images of the samples used for Pockels effect measurements showing optical quality are shown on fig.3.16. We can see that the sample no.2 has the worst optical quality, while samples no.3 and 5 show good optical quality due to a good crystallographic quality.

Sample no.	Compound	Contact metals	d (mm)	A (mm^2)	ρ (Ωcm)	$(\mu\tau)_e$ (cm^{2}V^{-1})	Orien-tation†	Methods ‡ PE	DCM
1	CdTe:In	Au/In	1.65	5×5	$3-5\times10^9$	$\sim10^{-3}$	N/A	•	×
2	CdTe:In	Au/In	1.65	5×5	$3-5\times10^9$	$\sim10^{-3}$	N/A	•	×
3	$Cd_{0.9}Zn_{0.1}Te$	Au/In	2.5	5×5	$\sim10^{10}$	3×10^{-3}	(111)	•	•
4	$Cd_{0.9}Zn_{0.1}Te$	Au/Au	2.5	5×5	$\sim10^{10}$	3×10^{-3}	(111)	×	•
5	$Cd_{0.97}Zn_{0.03}Te$	Au/Au	2.5	6×6	2.7×10^7	N/A	(111)	•	•

Table 3.2: List of measured samples. †) crystallographic orientation of area A with contacts. ‡) Performed experimental methods: PE … Pockels effect, DCM … discharge current measurements.

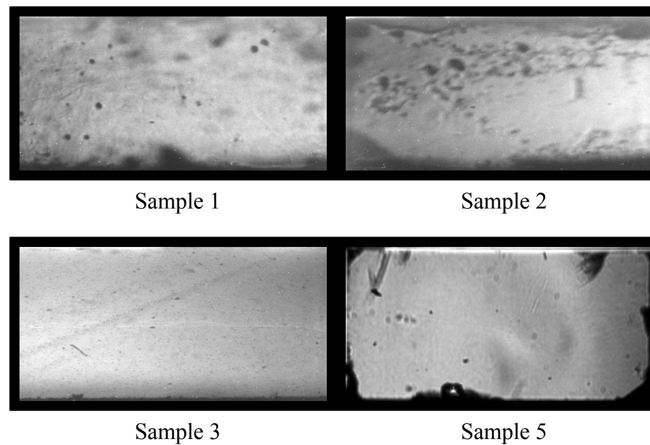

Figure 3.16: IR images of the samples showing optical quality taken by InGaAs camera.

3.5 Discussion: Pockels effect measurements

General factors affecting an electric field analysis using Pockels effect measurements are discussed in this section, while several aspects are discussed in chapter 4 on particular results.

At first, the main limiting factor for measurements is the optical quality of side surfaces of the samples and their perfect plane parallelism. Optical transmittance of measured samples was shown on fig.3.16. An influence of a bad optical quality of the sample on electric field profiles is apparent from fig.4.23.

Secondly, the crystallographic orientation plays an important role in strength of the Pockels effect. The geometric factor $\sqrt{3}/2$ from a sample parameter α_P defined by eq.2.57 is valid only if the electric field $\mathbf{E}$ is perpendicular to the plane (111) of the crystal (sample no.3 and 5). This mutual orientation is the most convenient for electric field measurements because the refractive index is independent on the direction of $\mathbf{k}$ vector if $\mathbf{k} \perp \mathbf{E}$ (eq.2.53) and the mutual phase shift $\Gamma_{(111)}$ of two perpendicular modes described in section 2.8.3 is

$$\Gamma_{(111)} = \frac{\sqrt{3}\pi}{\lambda_0} r_{41} \mathfrak{n}_0^3 \mathcal{E} L. \tag{3.11}$$

Generally, the value of the mutual phase shift Γ varies between zero and Γ_{max}, where

$$\Gamma_{max} = \frac{2\pi}{\lambda_0} r_{41} \mathfrak{n}_0^3 \mathcal{E} L, \tag{3.12}$$

depending on the mutual arrangement of vectors $\mathbf{E}$, $\mathbf{k}$, crystallographic orientation and the rotation of crossed polarizers (see more in ref. [92]). The geometric factor in α_p varies with this different phase shift Γ.

The crystallographic orientation of samples no.1 and 2 is unknown (but similar for both of them) so the geometric factor in α_p is unknown too. We have used the same α_p for electric field calculations as for "(111)"case and we have got the electric field profile with the absolute value differing from real value by its geometric factor[7]. In order to get the true absolute value of the electric field profiles $\mathcal{E}(z)$, it is possible to multiply them by normalizing factor $\mathcal{N}$ given by the following equation

$$U = \mathcal{N} \cdot \int_0^d \mathcal{E}(z) \mathrm{d}z, \tag{3.13}$$

where U is the applied voltage on the sample and d is the sample thickness.

[7]The electric field in certain point $\mathcal{E}$ depends linearly on the inverse sample parameter (α_P^{-1}) according to eq.2.59.

Macroscopic crystal and surface defects and crystallographic orientation in connection with quite difficult sample preparation are the main limiting factors of performing Pockels effect measurements on large sets of samples.

The third major factor affecting the accuracy of measurements is misalignment of the experimental setup during repeating measurements when the sample is unmounted and mounted again. Those measurements are not exactly repeatable in order to observe the completely same electric field distribution, but the main shape of the electric field profile remains always similar, and moreover we can monitor small changes of the electric field profiles measured under different conditions (such temperature, illumination intensity, etc.) during the same setting.

Sometimes it was necessary to recover contacts on the sample which brought the need to re-etch the sample surfaces and evaporate contact metals again. Reetching decreased optical quality of the samples (especially sample no.1) but the shape of the electric field profile remained the same. Graphs in chapter 4 depict mostly total measured data that show systematic fluctuations due to the bad optical quality of the samples, but those fluctuations have no influence on the evaluation of time constants of electric field evolution (sections 4.2.1 and 4.2.2). However, for example, the evaluation of the profile of a space charge requires the numerical differentiation of the electric field through the whole sample volume. In this case (see fig.4.6) it was necessary to avoid fluctuations of the electric field by "cutting"incorrect data close to the sample surfaces and use parabolic approximation that fit well the experimental data.

Despite the fact the measurements are affected by errors that can not be accurately classified, changes and tilting of the electric field profiles due to different conditions (i.e. time evolution, temperature, illumination intensity, etc.) are evident and the Pockels effect method allows us to study internal processes within the detector material.

Electric field distribution through detectors can be also measured using Transient Current Technique (TCT) [101]. This electrical method does not require good optical quality of detector samples but it is limited with calculation of linear electric field profiles in dark conditions only. TCT method is also available in our group at Institute of Physics of Charles University [102]. On the other hand, Pockels effect measurements allow us to study general profiles of the electric field under high flux conditions.

Chapter 4

Results I: Pockels effect measurements

Results acquired mostly by Pockels effect measurements are presented including the discussion in this chapter. Samples were studied at different conditions. All the measurements were performed at room temperature (unless otherwise indicated).

The chapter is divided into four main sections describing different experimental techniques exploiting Pockels effect. Section 4.1 describes fundamental aspects of the electric field measurements through the sample at different voltages in the dark. Second section 4.2 includes polarization study of the samples in the dark conditions. The following sections are focused on a high flux induced polarization. Section 4.3 deals with a behavior of the samples under high flux X-ray and laser irradiation. In order to understand internal processes in the samples, several electric field measurements were accompanied with photoconductivy measurements and numerical simulations. The last section 4.4 shows results acquired using a new method of IR spectral scanning of photo excited samples. This method was developed in order to find deep levels responsible for the photo induced polarization.

4.1 Basic measurements

General issues of electric field measurements demonstrated on the sample no.1 are discussed in this section.

4.1.1 Au/CdTe/In structure (Sample no.1)

At first we investigated the evolution of the electric field through the sample after application of the voltage in the dark (only low intensity testing light without excitation laser or X-ray beam). Time evolution of the electric field profile when gold was acting as a cathode for applied voltage 500 V is shown on fig.4.1. One

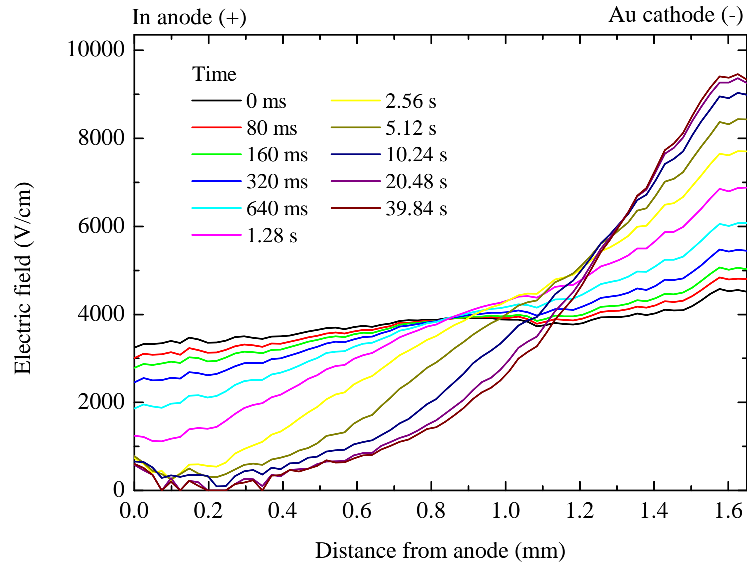

Figure 4.1: Time evolution of the electric field distribution through Au/CdTe/In sample after application of voltage 500 V. Au was acting as cathode. Temperature 286 K.

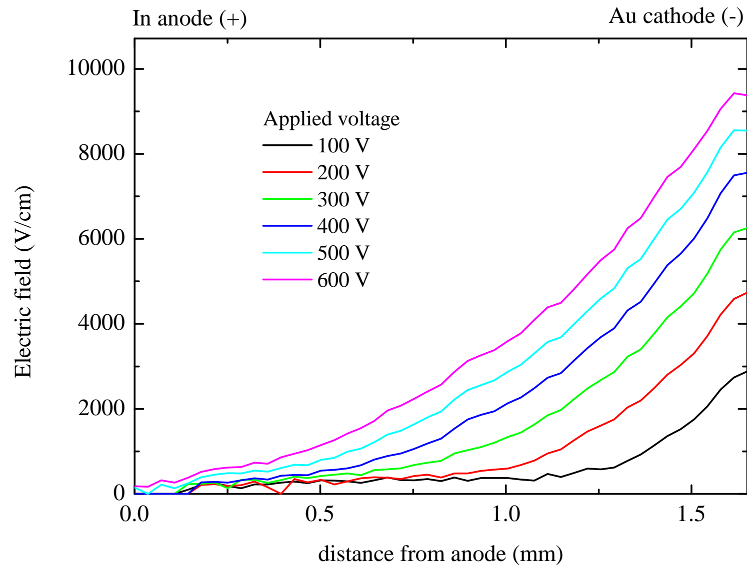

Figure 4.2: Electric field distribution through Au/CdTe/In sample at different applied voltage. Au was acting as cathode.

can observe that the electric field became steady within about 20 seconds. The redistribution of the electric field towards one of the electrodes and formation of a dead layer (zero electric field) below opposite electrode shown on fig.4.1 is a well known phenomenon called polarization in CdTe Schottky detectors described for the case of CdTe:Cl samples with a hole blocking In contacts by Cola et. al. [2]. All the measurements except of time dependent measurements were performed at steady state conditions.

Steady state electric field distribution through Au/CdTe/In sample at different applied voltages when Au was acting as an cathode is shown on fig.4.2 and

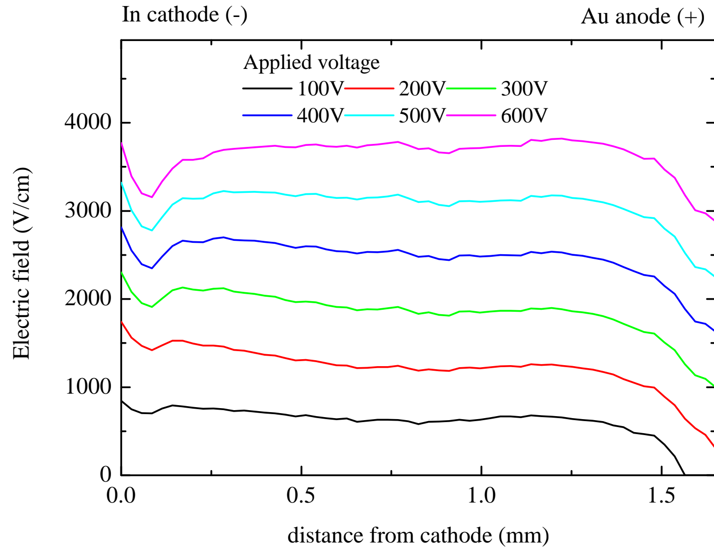

Figure 4.3: Electric field distribution through Au/CdTe/In sample at different applied voltage. Au was acting as anode.

when Au was acting as an anode od fig.4.3. One can see a significant increase of the electric field with the applied voltage and also a fundamental change in the shape of the electric field. While the electric field shows polarization effect if Au is acting as the cathode (fig.4.2), it remains nearly constant for opposite polarity (Au is acting as the anode, 4.3). This is due to the asymmetric band bending at contact metals and it is discussed later in the section 4.3.1.

If gold is acting as the cathode, the electric field is confined below it. With the increasing applied voltage the region of minimum electric field (dead layer) below the anode is decreasing. This corresponds to the presence of a positive space charge in the sample volume. Bands at the Au/CdTe interface are bent upwards. This is opposite to the case mostly investigated so far [2, 6].

Comparison between averaged measured electric fields at different voltages applied on the sample and theoretical values (applied voltage divided by sample thickness) presented on fig.4.4 shows quite good agreement. Worse agreement (lower values acquired from experimental data) for the case when the Au contact was acting as the cathode is caused by an accumulation of the electric field under the cathode (polarization) and bad transmittance of the sample very close to the cathode (shown on fig.4.5). So the average integrated value of the the electric field is slightly lower than the expected because the electric field tends to increase towards the cathode but it is impossible to measure it, so the higher part of the electric field integral is not measured in comparison with the opposite polarity when the electric field is nearly constant through the sample and the loss of its integral close to the electrodes is lower.

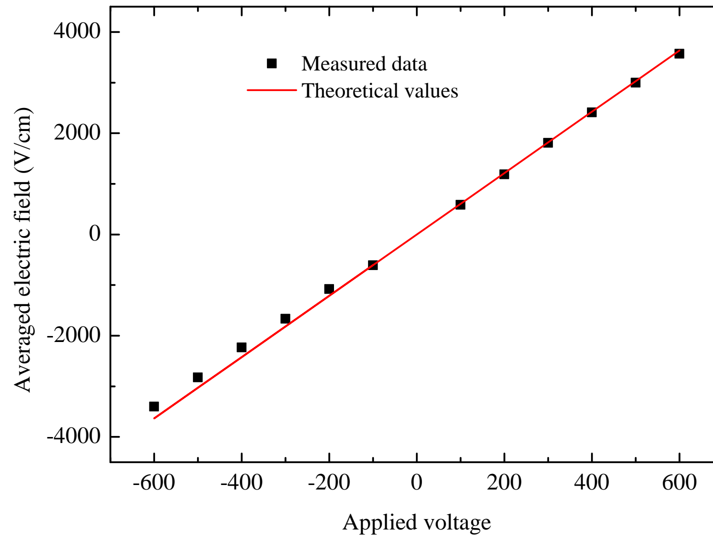

Figure 4.4: Linearity of averaged electric field distributions through Au/CdTe/In sample at different applied voltages.

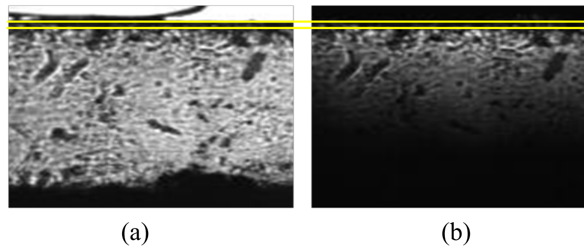

Figure 4.5: IR images acquired by InGaAs camera during the Pockels effect measurements. Image of the sample in parallel polarizers mode without voltage (a). Image of the sample in crossed polarizers mode with applied voltage 600 V (b). Au cathode is situated on the top of the sample. The part of the sample under Au cathode with a bad transmittance is bordered by two yellow lines.

4.2 Temporal and temperature evolution of the electric field

4.2.1 Au/CdTe/In structure (Sample no.1)

The time dependent measurement shown on fig.4.1 was repeated at different temperatures within the range of 286 and 316 K in order to obtain parameters of deep energy levels responsible for the polarization. The summary of the steady state electric field profiles (10 minutes after application of the voltage) acquired at different temperatures is presented in fig.4.6. The measured data were extrapolated using parabolic fit and set to zero for very low values of the electric field close to the anode (dead layer) in order to calculate the space charge density distribution (the need of this extrapolation is discussed in section 3.5).

The main feature of the temperature evolution is the decrease of the electric

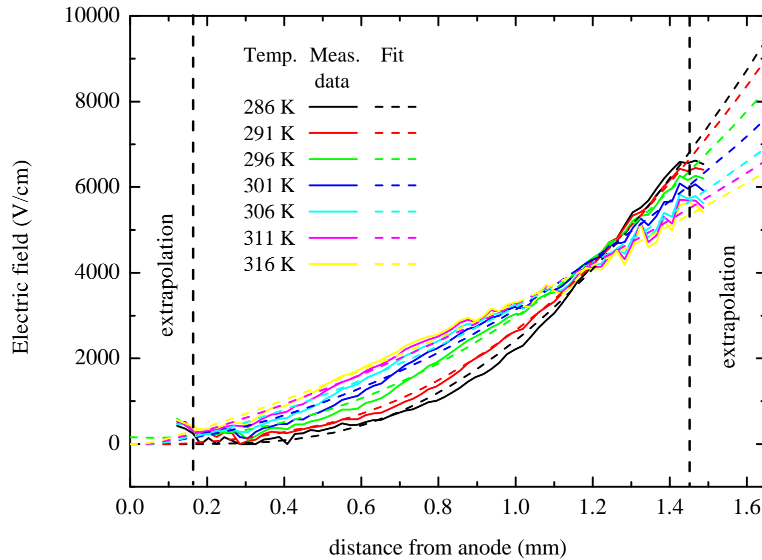

Figure 4.6: Temperature dependence of the steady state electric field profiles. Measured data were extrapolated using parabolic fit and set to zero for very low values of the electric field close to the anode (dead layer). Applied voltage 500 V.

field below the cathode and its increase in the central part of the sample. The distribution of the electric field just below the anode is practically independent on the temperature but the width of the dead layer is slightly decreasing with increasing temperature. Profiles of the distribution of the space charge shown on fig.4.7 were obtained by a numerical derivation of the profiles of the electric field by one-dimensional Poissons equation (eq.2.11) as

$$\frac{d\mathcal{E}}{dx} = -\frac{\rho}{\epsilon}, \tag{4.1}$$

where ρ is one-dimensional space charge density.

The space charge is positive in the most of the volume of the sample. With increasing temperature the positive space charge is decreasing below the cathode. Part of the positive space charge has moved to the middle of the sample. The total space charge in the sample is decreasing with an increasing temperature (see fig.4.8).

The temperature behavior of the space charge density in CdTe:In sample is different from that observed in CdTe:Cl samples (negative space charge, bands bent downward at the CdTe/In interface). While in the CdTe:Cl samples the polarization due to a space charge buildup is increasing with increasing temperature, in the CdTe:In samples it is decreasing.

This finding has an important practical consequences for the operation of radiation detectors. While in CdTe:Cl samples described above the polarization can be decreased by the decreasing of the temperature, in the case of behavior as observed in our CdTe:In detectors the decrease of the temperature can lead

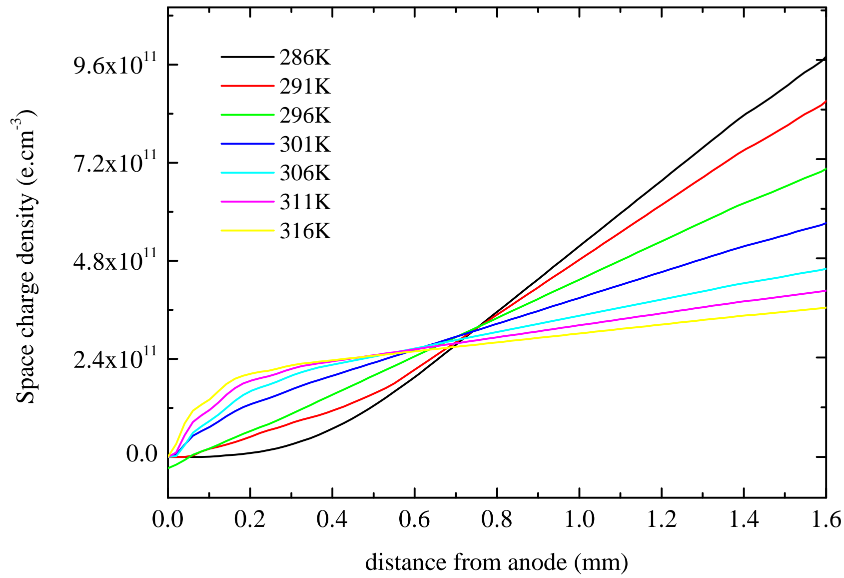

Figure 4.7: Profile of the space charge in dependence of the temperature after application of bias of 500 V obtained by numerical derivation of fitted data from fig.4.7

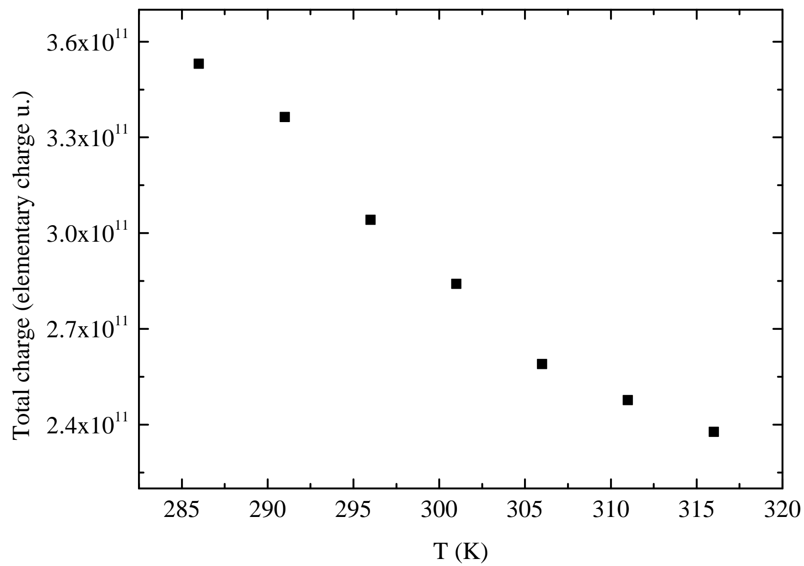

Figure 4.8: Temperature evolution of the total charge in units of elementary charge present in the sample

to a worsening of the polarization effect. On the contrary an increase of the temperature would be beneficial, but it would lead to an increase of the dark current and this way to a decrease of the signal-to-noise ratio.

We assume that the build-up of the space charge is caused by the de-trapping of electrons from deep levels after application of the bias. An example of the time evolution of the electric field close to the cathode is shown on fig.4.9. A double exponential (eq.3.10) best fits the acquired data. De-trapping time con-

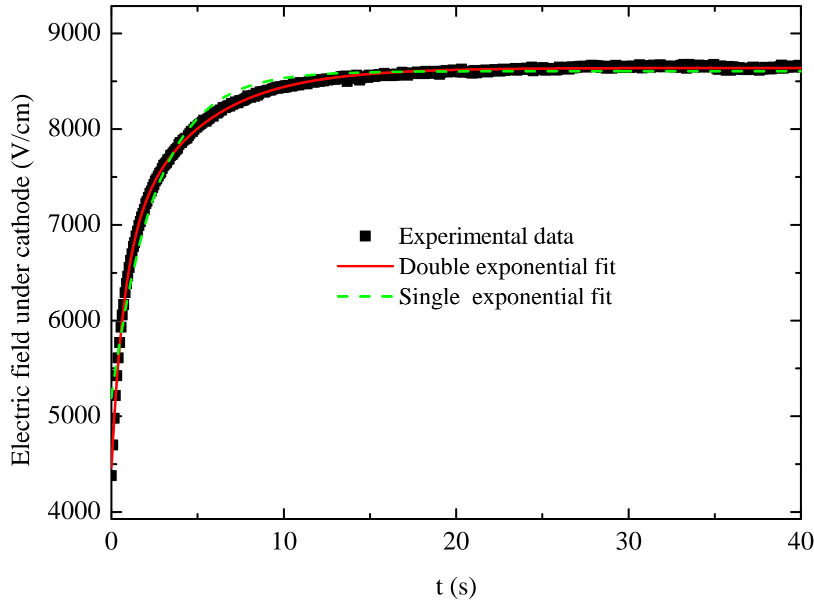

Figure 4.9: Experimental data of the time evolution of the electric field below the cathode and the double exponential fit at 291 K.

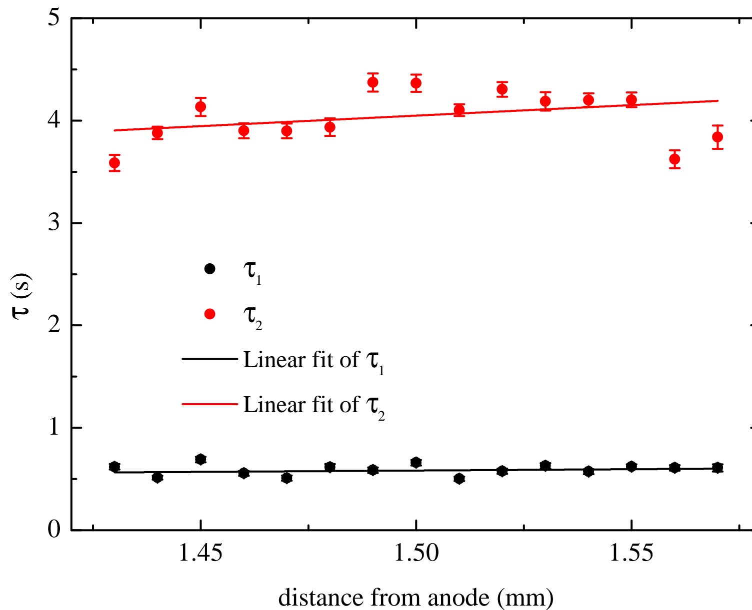

Figure 4.10: Evaluation of time constants τ_1 and τ_2 along the electric field profile at 288 K.

stants τ_{e1} and τ_{e2} acquired from the double exponential fit close to the cathode (fig.4.10) were averaged for each measured temperature[1] and they were ploted in the Arrhenius plot (see sec. 2.9.2) shown on fig.4.11.

We have observed two activation energies at 0.77 eV and 0.8 eV below the conduction band with electronic capture cross sections $\sigma_n = 6 \times 10^{-13}$ cm^2 and

[1] Only the time constants with a low standard error were averaged. There is a quite high error of time constants very close to the cathode caused by the bad transmittance and/or reflectivity just under the contact (see fig.4.5).

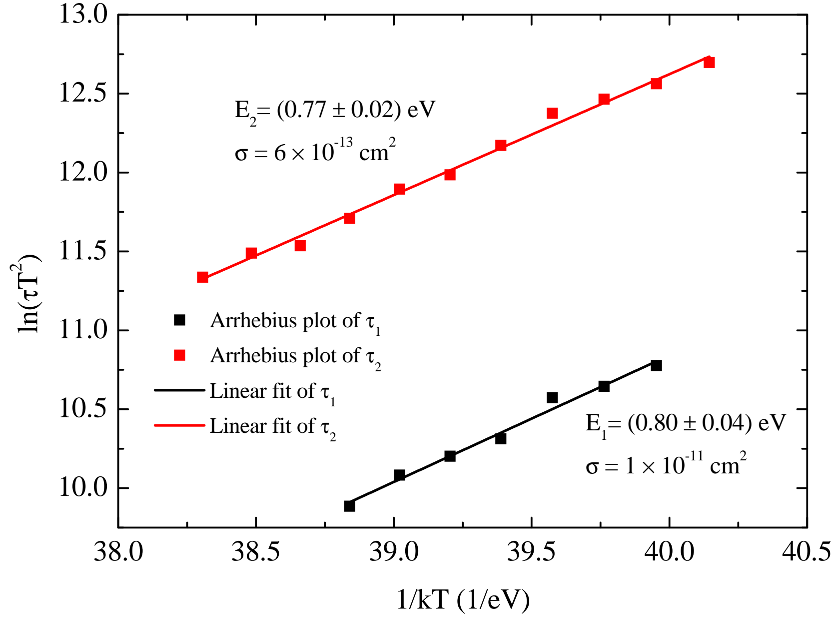

Figure 4.11: Arrhenius plot: evaluation of activation energies and capture-cross sections of deep donor levels.

$\sigma_n = 10^{-11}$ cm^2, respectively. Comparing this result with that obtained by Cola [2] on p-type CdTe:Cl sample with In electrode (bands bent downward, deep level at $E_v + 0.6$ eV) we conclude, that we observed the emission of electrons from levels which energetically are closely located in the energy gap to the energy measured by Cola because the sum of both energies is $\sim 1.4 - 1.5$ eV, which is close to the energy gap of CdTe $E_g \sim 1.46$ eV at 300K [103]. It is therefore possible that one of the energy levels E_i belongs to the transition of electrons from the same level as observed in ref. [2] for the case of emission of holes to the valence band. The scheme of emission of electrons from the deep level at -0.8 eV during the formation of the positive space charge region below the cathode after the application of the bias is presented on fig.4.12.

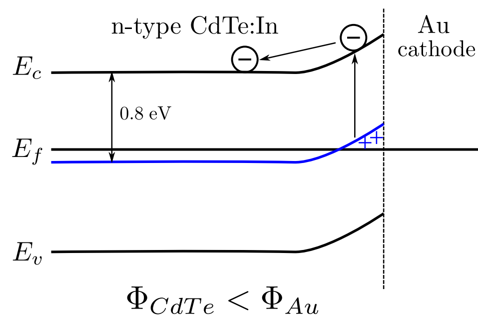

Figure 4.12: Scheme of emission of electrons from the deep level during a formation of a positive space charge region below the cathode after the application of the bias.

4.2.2 Polarization study in n-type CdZnTe (Sample no.5)

This section includes experimental results performed on the sample no.5. We have also presented these results in ref. [104].

Distribution and time stability of the electric field

Fig.4.13 shows the internal electric field profiles in the studied sample when the bias is 250 V and at temperature 300 K during 90 minutes after the application of the bias. We can see that few seconds after the biasing the region, where the electric field is not negligible shrinks to about 30% of the sample thickness at the cathode side. i.e most of the bias concentrates near the reverse biased contact of the structure. The electric field is confined below the cathode. This corresponds to the presence of a positive space charge in the sample volume. Bands at the Au/CZT interface are bent upwards. This is opposite to the case studied so far [2,6,11,94,95]. We also note that the electric field moves towards the cathode, where after about 25 minutes from applying the bias, the field is confined in a region of about 12% of the sample thickness. This results in the reduction of the depletion width L_d.

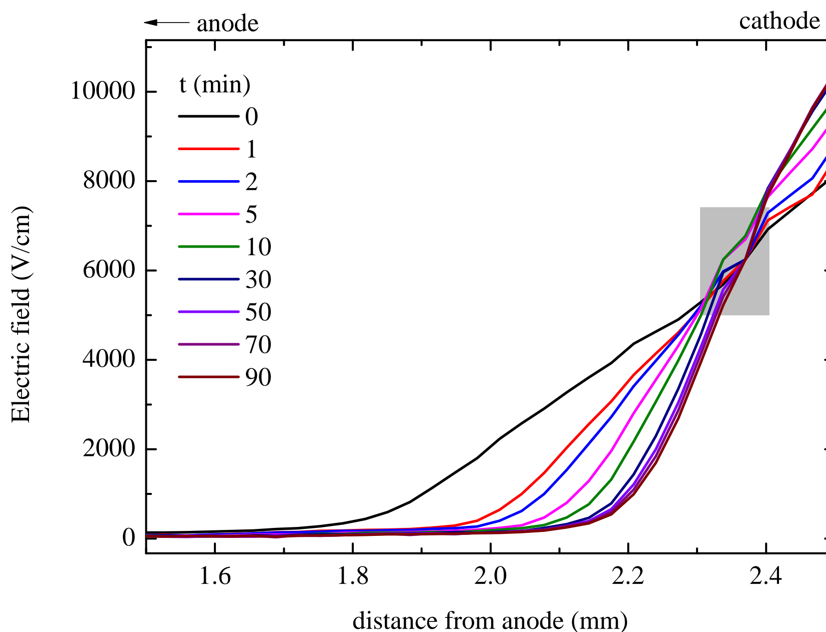

Figure 4.13: Distribution of the electric field with time in the sample at 250 V and 300 K. Only a part of the sample below the cathode is presented because the electric field is close to zero in the rest part. The noise of presented data within grey rectangle is caused by the reconstruction of the electric field associated with a maximum of the transmittance (see point A on fig.3.8c).

The time dependence of the accumulated space charge at the cathode due to the time changes of the ionization of the deep donor is obtained from eq.2.64 as

$$\Delta n_t^+(t) = \frac{\epsilon}{e}\left[\frac{d\mathcal{E}(x,t)}{dx}\right]_{\text{cathode}} . \tag{4.2}$$

Therefore, by making a derivative of the electric field curves in fig.4.13 at the cathode region, the time distribution of the space charge $e\Delta n_t^+(t)$ could be determined, as presented in fig.4.14. The exponential fit of $e\Delta n_t^+(t)$ is in good agreement with the experimental data. The final donor concentration is estimated from fitting[2] as $N_t = \Delta n_t^+(\infty) = 1.81 \times 10^{11}$ cm^{-3}. It could be seen from the figure that after about 25 minutes from application of the bias, almost ($\sim 94\%$) of the initially neutral deep donors are ionized.

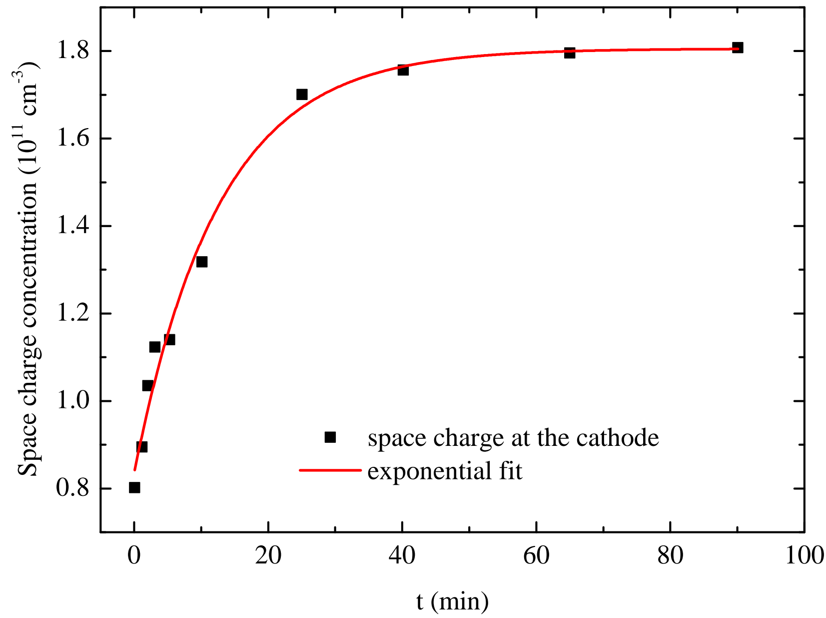

Figure 4.14: Time evolution of the space charge at the cathode at 300 K and 250 V.

Temperature dependence of the electric field

The time dependences of the Pockels effect measurements at 200 V were performed at different temperatures in the range of 298 K - 320 K. Fig.4.15 shows the time evolution of the calculated electric field $\mathcal{E}(0)$ just below the cathode at

[2] This calculation is valid only in the case if the deep level is fully ionized. Said presumption is correct as it is shown later on page 60 in this section.

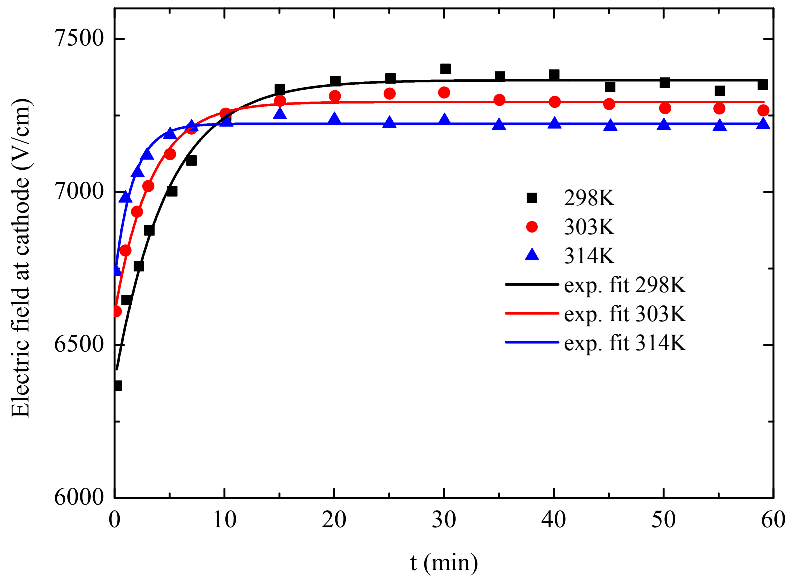

Figure 4.15: Time evolution of the electric field calculated at the cathode interface at 200 V and at different temperatures.

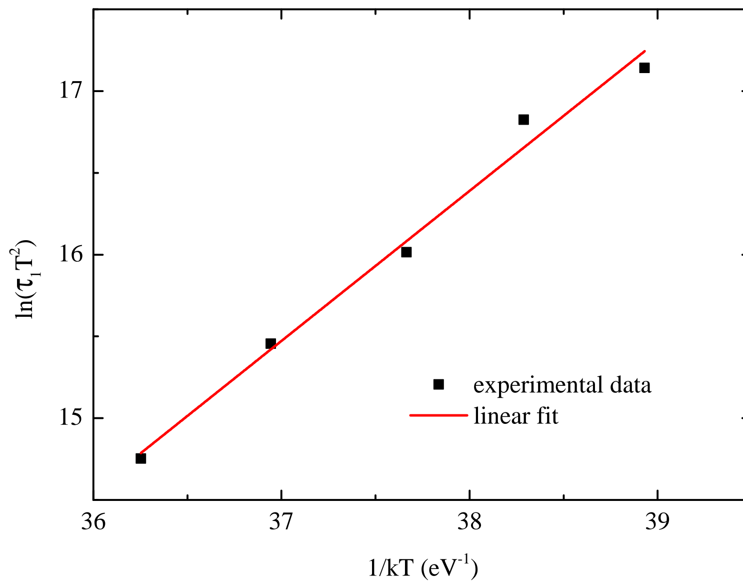

Figure 4.16: Arrhenius plot of the de-trapping time.

different temperatures. The exponential fits of these data give the temperature dependence of the de-trapping time τ_e. As expected from eq.2.60, de-trapping times are thermally activated and they are well described by an Arrhenius plot shown on fig.4.16.

The activation energy $E_A = (0.92 \pm 0.06)$ eV of the trap responsible for the polarization and its capture cross-section $\sigma_n = 3.5 \times 10^{-13}$ cm^2 were obtained from this Arrhenius plot.

It was reported in [2] that the deep level responsible for a polarization

mechanism has an energy $E_t = E_v + (0.62 \pm 0.02)$ eV in p-type CdTe samples. In this work (n-type CZT sample) we attribute the polarization to the deep level of energy $E_t = E_c - (0.92 \pm 0.06)$ eV. Noting that the sum of both energies nearly equals the bandgap of CZT ($\sim$1.54 eV) at room temperature, we deduce that the origin of this deep level could be the same in both types of samples. It can emit holes when the bands are bent downwards (CdTe:Cl samples with In contact) or electrons in the opposite case (CZT with Au contacts, when the bands are bent upwards).

Electric field - voltage dependence

The Pockels effect measurements were performed for different voltages applied on the sample (fig.4.17). Presented are the time dependences of the electric field just below the cathode at different values of the bias. We can see that the electric field quickly increases with time at the beginning, and reaches almost saturation after about 25 minutes. We attribute this behavior to the de-trapping of electrons that cause a change of the depletion width and consequently increase the electric field. After about 25 minutes from the application of the bias, almost all carriers are de-trapped in the depleted region. The deep donor level becomes almost fully ionized, which results in a nearly time independent depletion width.

The dependences of the electric field $\mathcal{E}(0)$ just below the cathode on $\sqrt{U}$ at different times are shown on fig.4.18. These are straight lines with time dependent slopes. This supports the model from eqs.2.68 and 2.69.

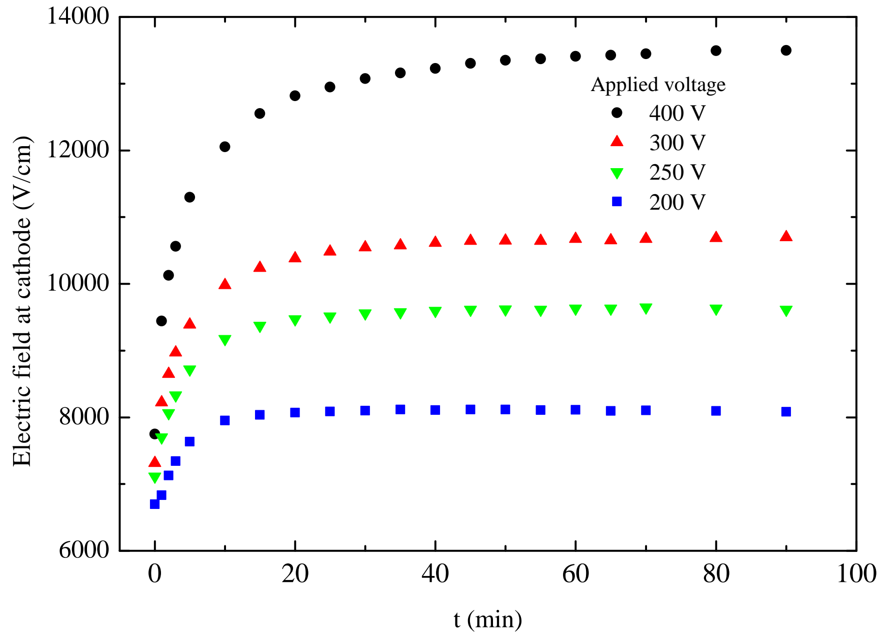

Figure 4.17: Time evolution of the electric field calculated just below the cathode at 300 K for different voltages.

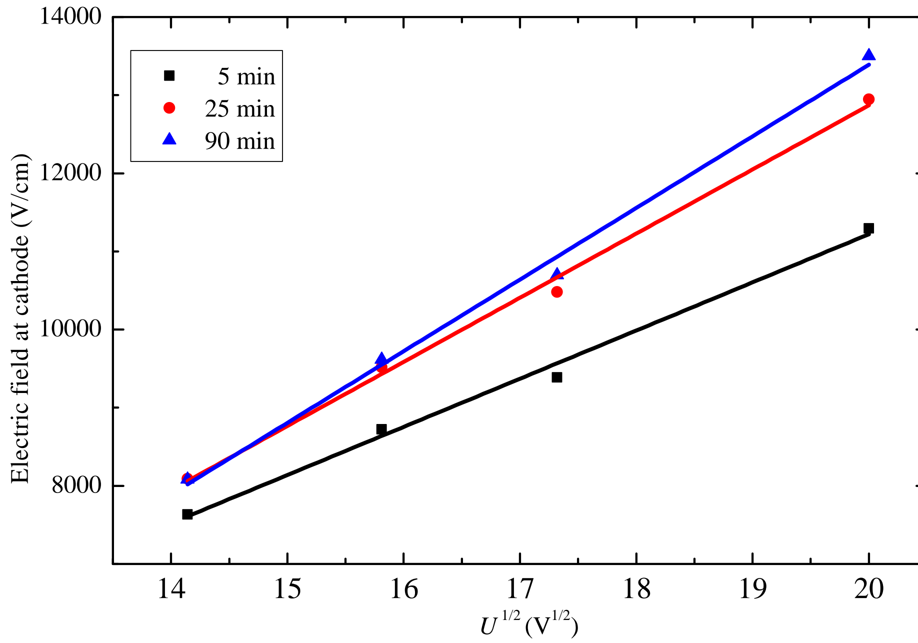

Figure 4.18: Plot of the electric field versus $\sqrt{U}$ at three different times from the data of fig.4.17

The total donor concentration N_t is calculated using the slopes at different times. The calculated values of N_t are almost time independent, with an average value of 2×10^{11} cm^{-3}. This value is in an excellent agreement with the value estimated from fig.4.14 and it is in general agreement with data reported earlier [105–107].

Electric field - transient current

The time dependence of the transient current of the studied sample was measured at 296 K with the applied voltage 100 V over a long time scale. The data fit well to an exponential function with two characteristic times of values $\tau_1 = 478.8$ s and $\tau_2 = 2.6 \times 10^4$ s as presented on fig.4.19. When using the τ_1 value and the value of the obtained capture cross-section $\sigma_n = 3.5 \times 10^{-13}$ cm^2 in eq.2.60, the deep level energy equals exactly to 0.92 eV, which is identical to the value obtained by the analysis of Pockels measurements earlier in this section. It is clear that the time τ_1 is associated with the de-trapping of electrons from the deep donor to the conduction band. Therefore, there is one component of the transient current that is correlated to the time dependence of the electric field at the cathode $E(0, t)$ through eq.2.73 and it is dominant in the shorter time range. The other time component of the transient current τ_2 that is dominant in the long time range is present due to some long time process. It could be caused by an electro migration of charged defects in the electric field. Such a long-time characteristic was observed also in [95].

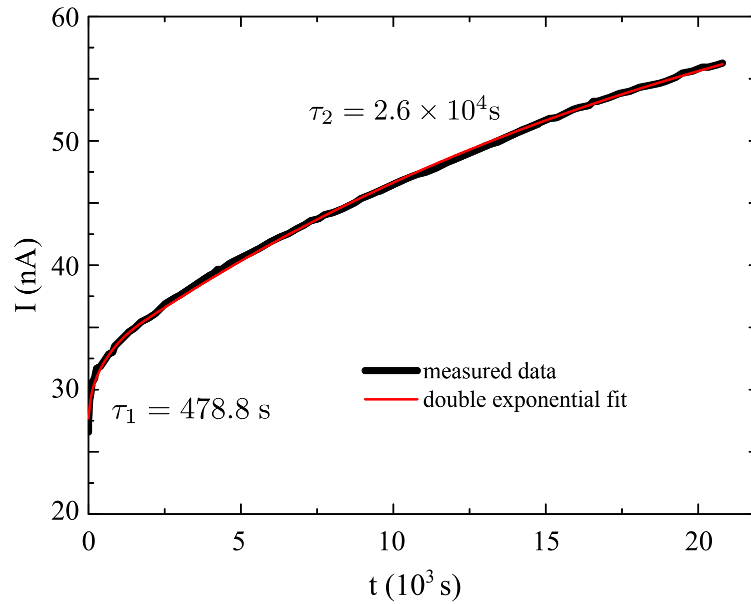

Figure 4.19: Time evolution of the current transient at 296 K and 100 V.

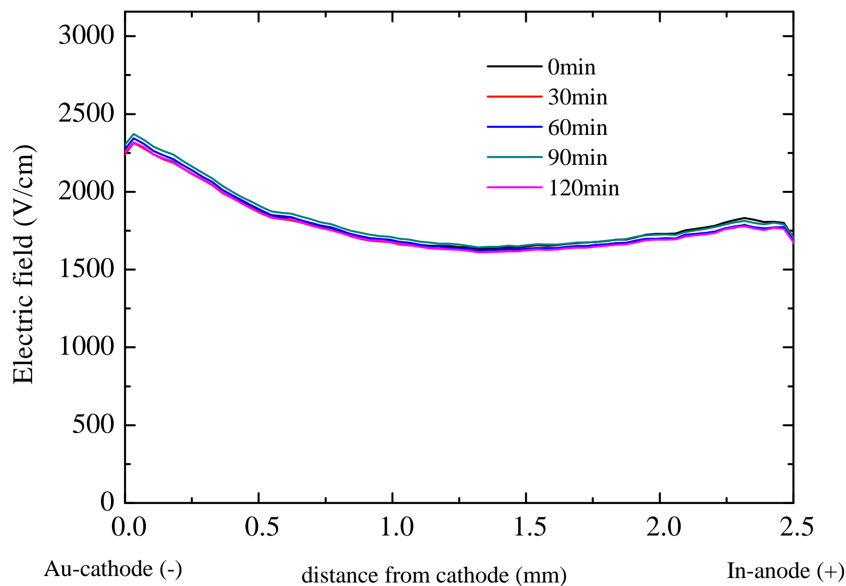

Figure 4.20: Time stability of the electric field in the sample no.3 in the dark. Applied voltage 500 V.

4.2.3 Au/CdTe/In structure (Samples no.3)

On the other hand, the electric field distribution through the sample no.1 (high resistivity CdZnTe) was nearly constant and stable in time after application of the bias in the dark (fig.4.20). This situation corresponds to nearly ohmic contacts because the polarization (time dependent electric field) in the dark conditions is associated with Schottky detectors.

4.2.4 Comparison of steady state electric field profiles (Samples no.1, 3 & 5)

In this section we compare electric field profiles measured on different samples in the dark. Fig.4.21 shows the comparison of the electric field profiles of biased samples no.1, 3 and 5 in the dark while gold was acting as the cathode.

We have estimated depletion widths $L_{d1} = 1.5$ mm and $L_{d5} = 0.4$ mm of samples no.1 and no.5, respectively. Sample no.3 is fully depleted. It was shown above in this section that samples no.1 and 3 showed time dependent polarization that can be described by a conventional model for Schottky barrier (see eq. 2.67) due to the band bending at Au/Cd(Zn)Te interface, while sample no.3 was stable due to a very low band bending ($\Phi_{Au} - \Phi_{CdZnTe} < 4k_BT \sim 100$ meV, [8]), when Ohmic contact conserves the density of the carriers in the equilibrium value.

According to eq. 2.67, the higher concentration of the deep level N_t in the sample no.5 leads to a shorter depletion length L_d than in the sample no.1.

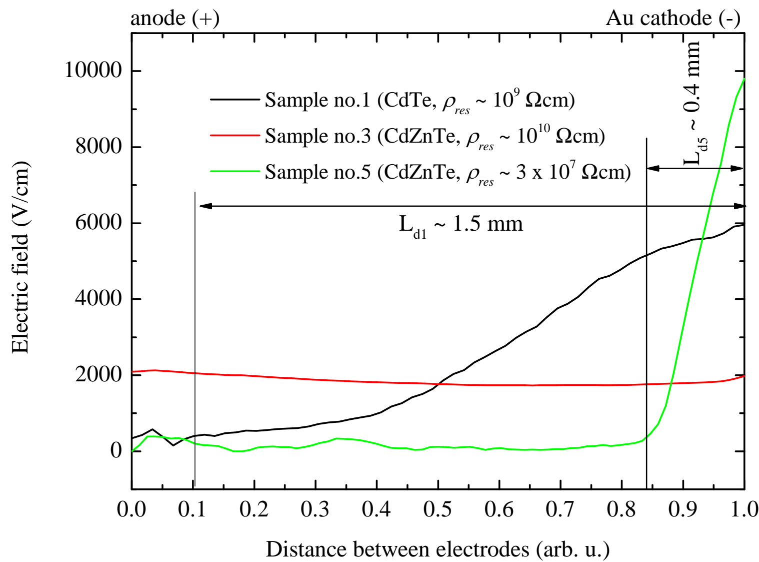

Figure 4.21: Electric field distribution through the samples with a different resistivity with estimated depletion widths. Gold was acting as cathode.

4.3 X-ray and laser irradiation

4.3.1 Au/CdTe/In structure (Samples no.1 & 2)

Electric field measurements performed on Au/CdTe/In sample under X-ray and laser irradiation are shown in this section and they have been presented in ref. [15]. Experimental setup is described in section 3.1.1, fig.3.6.

An X-ray tube with an Ag anode was used as the source of X-ray radiation. The Au electrode of the CdTe sample, acting as the cathode, was simultaneously

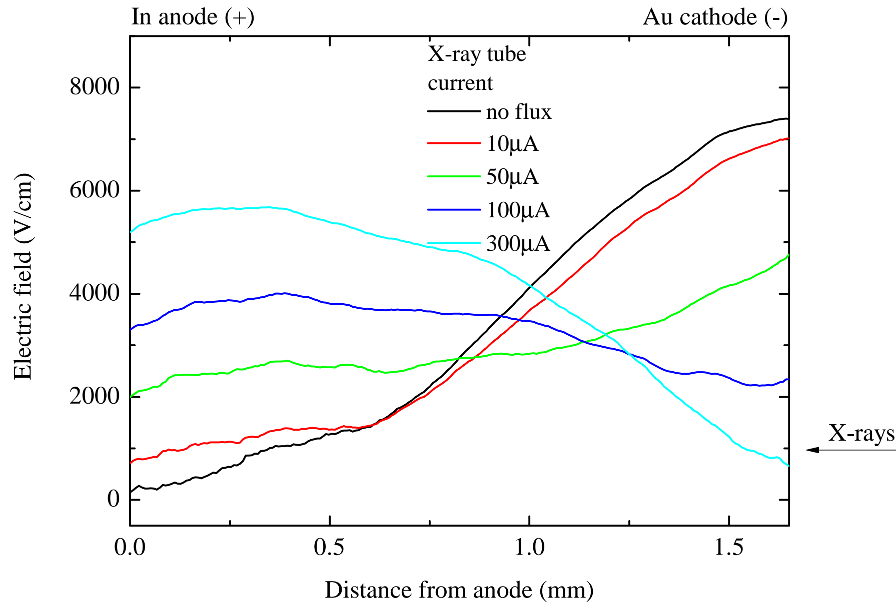

Figure 4.22: Electric field distribution through the sample under X-ray irradiation. An external voltage 500 V was applied. The electric field decreases from the cathode forming a dead layer below the anode when no X-ray flux was applied. The electric field profile approaches a constant value with an increasing X-ray flux. Further increase in radiation flux results in a formation of dead layer below the cathode.

irradiated with X-ray photons. X-ray photons were absorbed within a thin layer under the electrode according to ref. [34]. It means that holes recombined at the cathode and only electrons were contributing to photoelectric transport while they were drifting through the whole sample towards the anode. Similar radiation conditions were also acquired using the Ti:Sapphire laser tuned to the wavelength 754 nm, when the photons are also absorbed within a thin layer under the illuminated electrode due to high absorption coefficient.

The results of the measurement of steady-state electric field profiles for applied external voltage 500 V (average internal $\mathcal{E}$ = 2000 V/cm) are shown in fig.4.22. The steady-state without flux was achieved within one minute after applying the voltage, when most of the charge redistribution happened within the first 20 seconds. Then the electric field profile remained unchanged within 16 h 40 min of testing.

The electric field decreases from the cathode forming a dead layer below the anode, when no X-ray radiation was applied. This situation corresponds to a prevailing positive space charge accumulated in the sample. The profile of the electric field approaches a constant value with an increasing X-ray flux[3]. Further increase in radiation flux results finally in the formation of a dead layer below the cathode.

The results shown on fig.4.23 were obtained on neighboring sample no.2 with

[3] We call this situation as a "radiation induced depolarization".

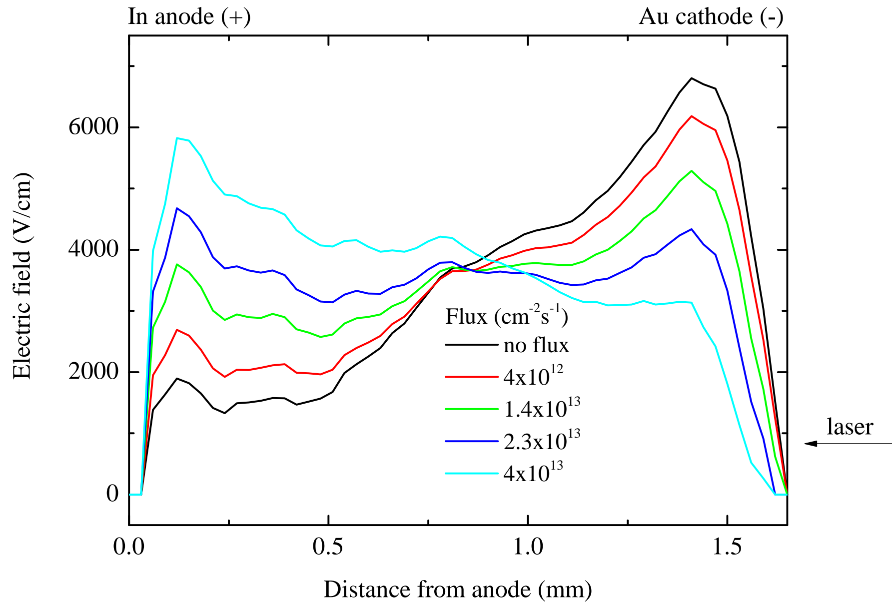

Figure 4.23: Electric field distribution through the sample under laser (754 nm) irradiation (sample no. 2, worse optical quality). An external voltage 500 V was applied. The profile of the evaluated electric field at the edges is influenced by a scattering of the testing light on the bad surface of the sample close to its edges.

semitransparent gold contact using 754 nm laser radiation instead of X-rays. A worse quality of the acquired electric field profiles is caused by a worse optical quality of the sample surfaces. One can see similar behavior of the electric field under laser and X-ray radiation. So it is possible to use a better defined laser radiation instead of X-rays for study of semiconductor detectors operating at high fluxes of X-ray radiation. It is possible to find similar conclusions in refs. [16,108]. Decrease of the electric field very close to the cathode (in the range of approx. 0 and 0.02 cm) is caused by a lower transmittance close to the sample surface and by a scattering of the testing light due to a worse optical quality of the sample and possible misalignment of the setup.

The difference of work functions between both metals and CdTe was used as an optimizing parameter of the model, looking for agreement with the experimental profiles in both polarities of the applied voltage. The chosen band profiles for $\Phi_{Au} - \Phi_{CdTe} = 150$ meV (bands bent upwards) and $\Phi_{In} - \Phi_{CdTe} = -50$ meV (bands bent downwards) are shown on fig.4.24 without applied voltage. The results of the simulation of the electric field for an applied voltage 500 V are presented in fig.4.25. Apparently, the chosen model very well fits the experimental data. The parameters of the deep level used in the simulation were as follows: energy $E_t = E_c - 0.5E_g$, concentration $N_T = 4 \times 10^{11}$ cm^{-3}, capture-cross section for electrons $\sigma_n = 5 \times 10^{-13}$ cm^2, and capture-cross section for holes $\sigma_p = 3 \times 10^{-14}$ cm^2. The inaccuracy of the experimental results is mostly caused by the optical properties of the sample surface.

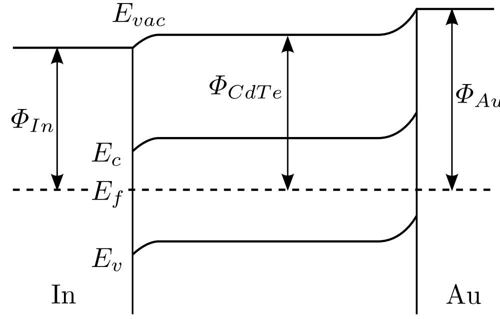

Figure 4.24: Band diagram of Au/CdTe/In structure with work functions Φ (energy difference between Fermi level E_f and vacuum level E_{vac})

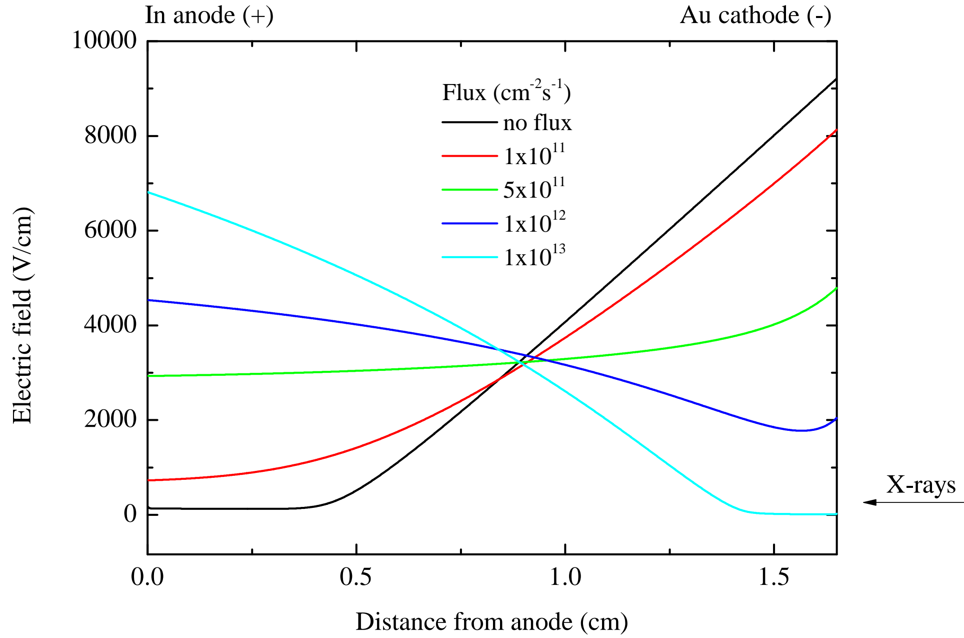

Figure 4.25: Electric field distribution through the sample under irradiation. The results of the simulation for $\Phi_{Au} - \Phi_{CdTe} = 150$ meV (bands bent upwards) and $\Phi_{In} - \Phi_{CdTe} = -50$ meV (bands bent downwards).

The sample is positively charged due to the band bending at the Au/CdTe interface (bands bent upwards) which prevails over the smaller band bending at the CdTe/In interface (bands bent downwards) without X-ray flux. The observed turn-over of the field with increasing radiation flux (fig.4.22) can be explained by the assumed compensation of this positive space charge with a negative space charge due to electrons trapped at the deep level. The prevailing capture of electrons and build-up of negative space charge under illumination is a result of the higher capture-cross section of electrons compared to holes chosen in the model. The profiles of space charge (for the electric field profiles shown on fig.4.25) calculated using the Gauss law shown on fig.4.26 clearly confirm the mechanism of the space charge compensation described above. This mechanism is also schematically illustrated on fig.4.27.

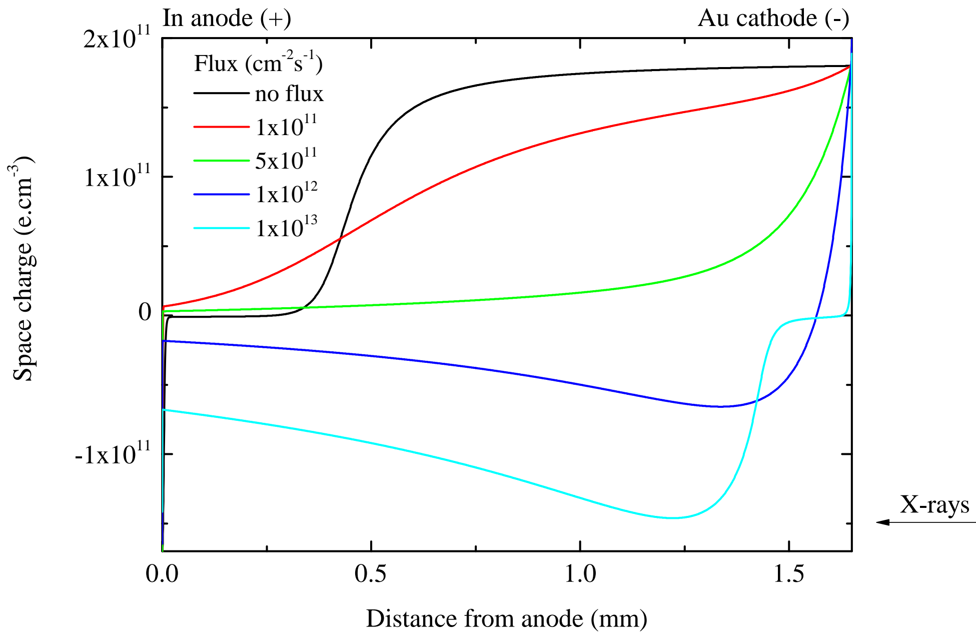

Figure 4.26: The calculated profiles of space charge for the electric field profiles in fig.4.25 clearly confirm the mechanism of space charge compensation.

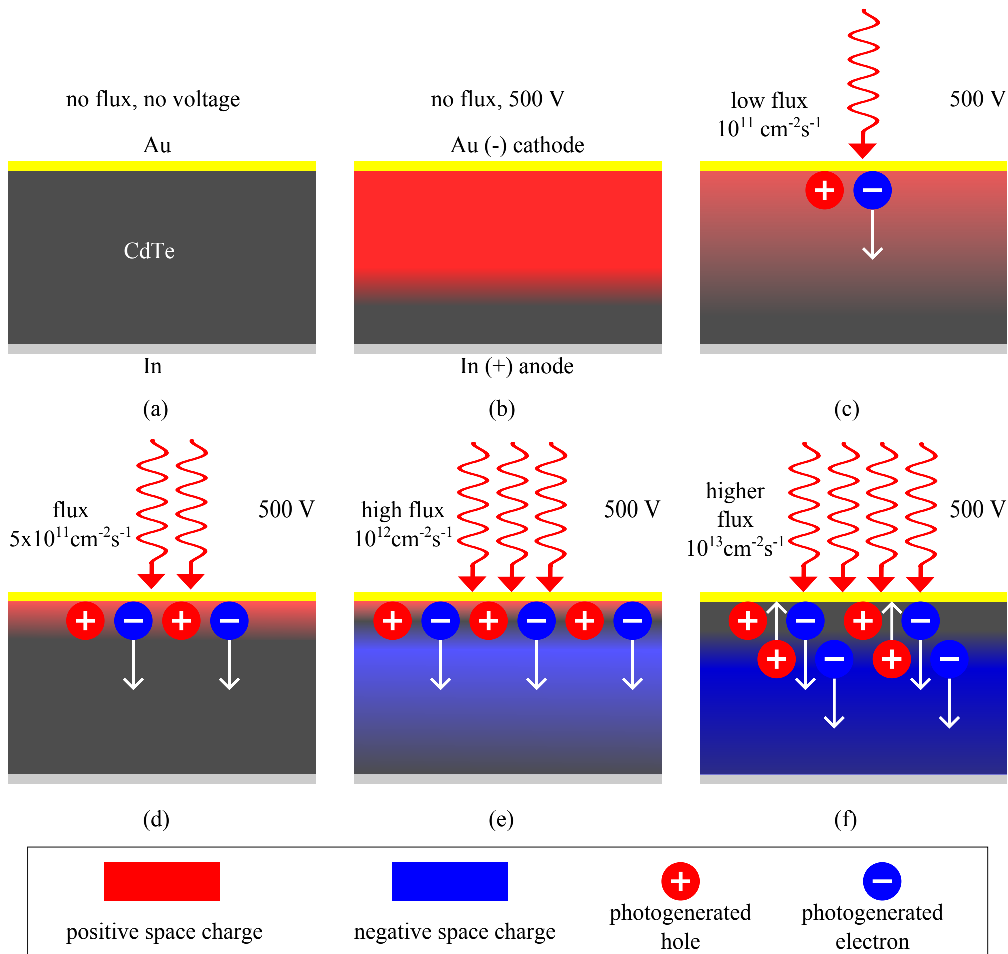

Figure 4.27: Internal processes corresponding to space charge profiles from fig.4.26.

With the used polarity of the external voltage the contacts are blocking the flow of both electrons and holes. The band bending at the In/CdTe interface is much smaller than assumed from the contact potential difference probably due to the dipoles formed at the interface due to a presence of a thin oxide layer between In and CdTe. This conclusion is based on the above described simulations of electric field profiles.

The demonstrated mechanism represents a promising way how to decrease the problems associated with electric field modification and reduced charge collection efficiency in CdTe X-ray detectors operated at high fluxes of X-ray photons. While at low-fluxes of high-energy photons an additional illumination can increase the noise to a level comparable or higher than the signal, at high fluxes the additional noise may be negligible compared to the signal.

4.3.2 Au/CdZnTe/In structure (Sample no.3)

Simultaneous Pockels effect and photoconductivity measurements were used to study the processes in Au/CdZnTe/In detector sample no.3 at steady state high flux conditions.

Experimental setup is described on fig.3.6. The electric field profiles of the sample biased at 500 V while the irradiated gold contact was acting as a cathode under different photon fluxes of tunable Ti:Sapphire laser set to a wavelength of 798 nm (fig.4.28) are comparable with electric field profiles for different radiation fluxes of a Ag target X-ray tube excitation (fig.4.29). This fact enables (as descri-

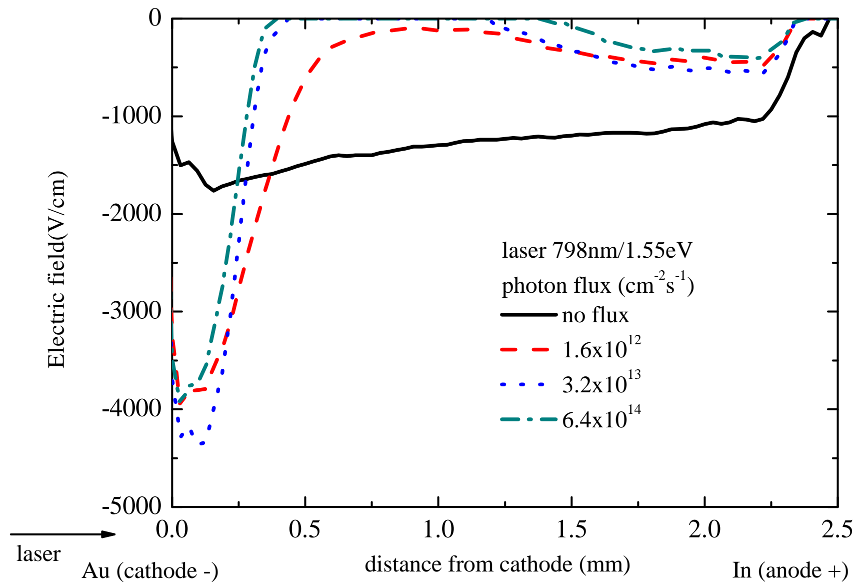

Figure 4.28: Electric field dependence on different photon fluxes. Laser wavelength/photon energy 798 nm/1.54 eV, applied voltage on sample was 500V.

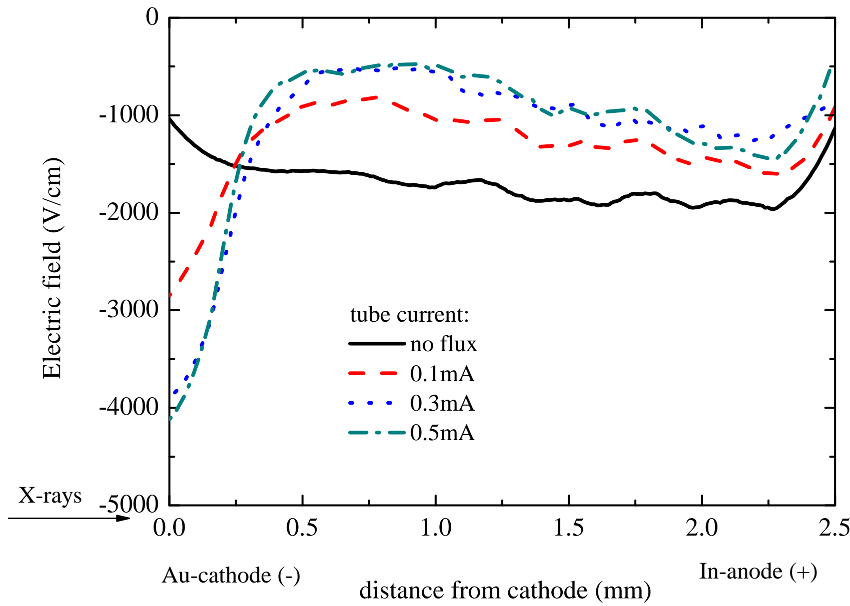

Figure 4.29: Electric field dependence on different X-ray tube current. Ag target X-ray tube operated at voltage 49.5 kV. Applied voltage on sample was 500V.

bed in section 4.3.1) to exploit monochromatic laser radiation instead of X-rays for study CZT detectors operating at high fluxes of X-ray radiation. The electric field profile at 'no flux' conditions is nearly constant[4]. Therefore, Au/CdZnTe and CdZnTe/In interfaces can be considered as nearly ohmic. This result is expected in the case of the Au/CdZnTe interface, when the work functions of Au and semi-insulating CdZnTe are comparable ($\sim$ 5.2 eV). The band bending at the In/CdZnTe interface is again apparently much smaller than assumed from work functions difference, probably due to the dipoles formed at the interface due to presence of thin oxide layer between In and CdZnTe.

The photoconductivity spectrum measured at room temperature is shown on fig.4.30. The voltage applied on the samples was 200 V and the photon flux of the laser at all wavelengths was constant (approx. 10^{15} cm^{-2}s^{-1}). The photocurrent density increases from lower photon energies (sub-band energy) to its maximum at 1.55 eV (wavelength 803 nm), due to the increasing absorption of CdZnTe. For lower photon energies the light is absorbed deeper in the sample and both types of photogenerated carriers participate in charge transport. At higher photon energies the incident light is absorbed in a thin (few μm) area below the surface, photogenerated holes immediately recombine at the cathode and only electrons drift through the whole sample towards the anode. The photocurrent at higher photon energies decreases due to surface recombination.

[4]There are slight differences between profiles shown on figs.4.28 and 4.29 caused by the same reasons as described in section 4.3.1 but the similarity is significant.

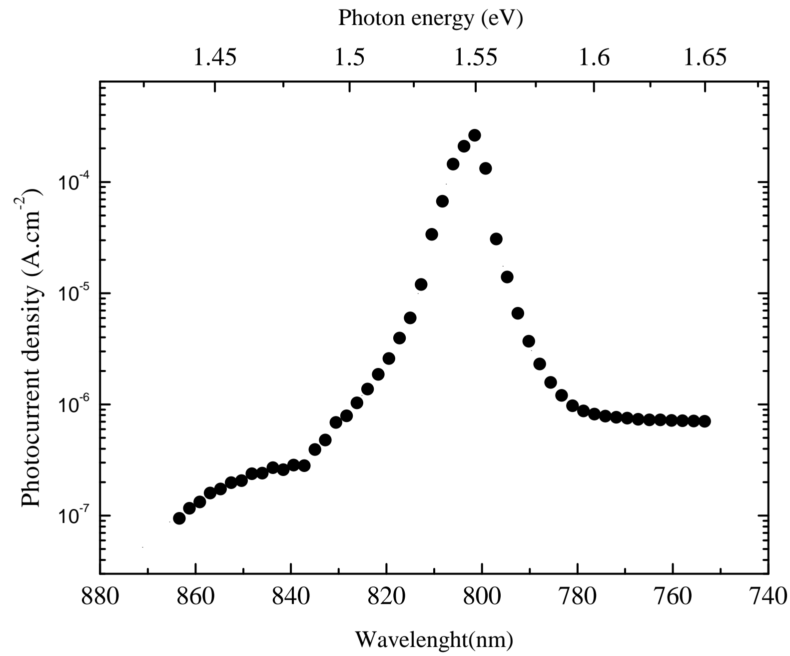

Figure 4.30: Photoconductivity spectrum measured using tunable Ti:sapphire laser at applied voltage 200V.

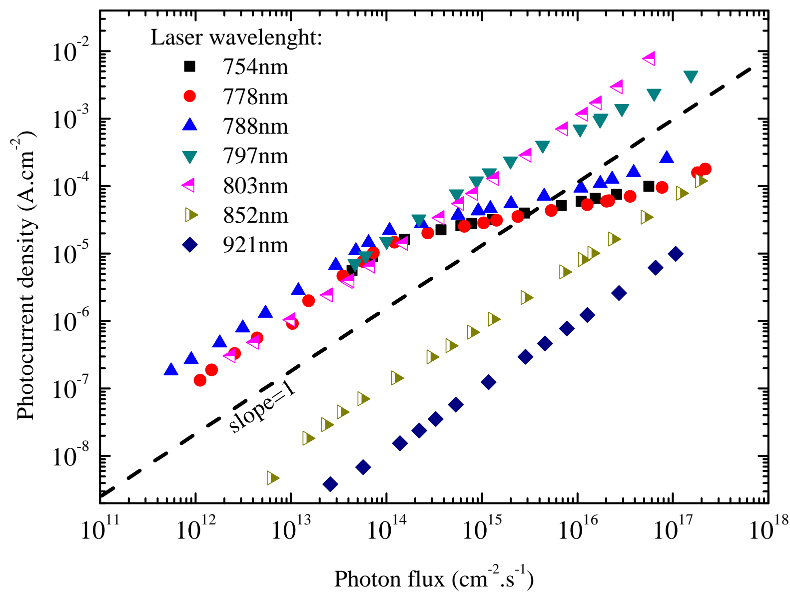

Figure 4.31: Measured lux-Ampere characteristics for different wavelengths of laser radiation. Applied voltage 500V.

Lux-Ampere characteristics measured at different laser wavelengths are shown on fig.4.31. Several characteristic features can be observed. At high absorption coefficients (lower wavelengths) and low flux the dependence is linear. With an increasing flux it starts to become sublinear. This behavior was explained in ref. [17]

by screening of the applied voltage by negative space charge accumulated at the deep level. Illumination with longer wavelength radiation firstly results in linearization of the dependence (wavelengths 797–803 nm). With a further increase of the wavelength the values of the photocurrent decrease and the dependence remains linear. Lower values of the photocurrent for sub-gap excitation radiation are caused by lower absorption.

For comparison, fig.4.32 shows the numerical simulation of lux-Ampere characteristics for various absorption coefficients, which agrees well with the measured data shown on fig.4.31. The parameters of the deep level used in all the simulations included in this section were: $E_t = 0.5E_g$, concentration $N_t = 8 \times 10^{11}$ cm^{-3}, capture-cross section for electrons $\sigma_n = 10^{-13}$ cm^2 and capture-cross section for holes $\sigma_p = 8 \times 10^{-11}$ cm^2.

Linearity of the lux-Ampere characteristic ($\beta = 1$ in log-log scale) means that all the photogenerated charge is collected ($CCE = 1$). Sublinear lux-Ampere characteristics ($\beta < 1$) is a sign of a smaller CCE.

The electric field distribution through the sample for the case of above-gap excitation is presented in fig.4.33. We tested the dependence of the electric field on different light intensities of the excitation laser set at the wavelength 754 nm. The applied voltage was 500V. There is only a small change of the electric field for photon fluxes up to 1.6×10^{13} cm^{-2}s^{-1}. In this case there is no significant screening of the applied voltage and the slopes β of lux-Ampere characteristic for lower fluxes shown in fig.4.31 for $\lambda = 788$ nm and fig.4.32 for $\alpha = 10000$ cm^{-1} are nearly equal to 1. This is consistent with a small accumulation of photogenerated charge (electrons) trapped at deep levels. For higher fluxes the electric field in fig.4.33 decreases from the anode forming a dead layer below the cathode. This

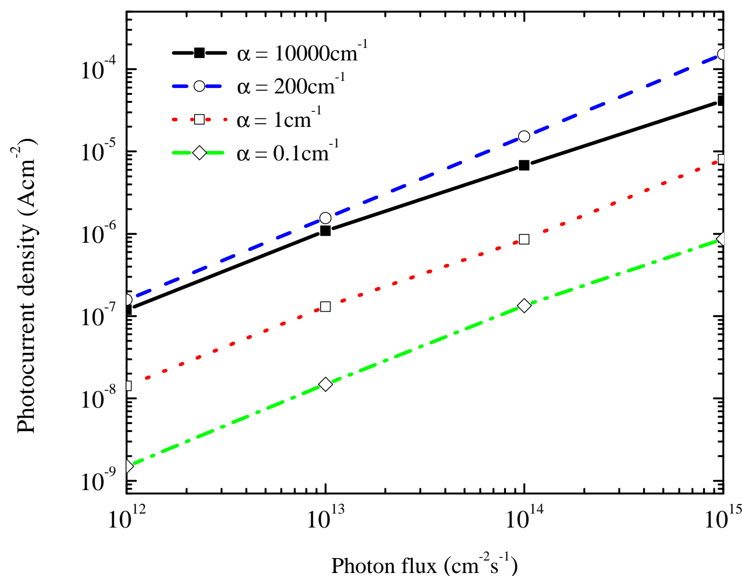

Figure 4.32: Numeric simulations of lux-Ampere characteristics for different absorption coefficients α based on Hall-Shockley-Read model, drift-diffusion and Poisson equations.

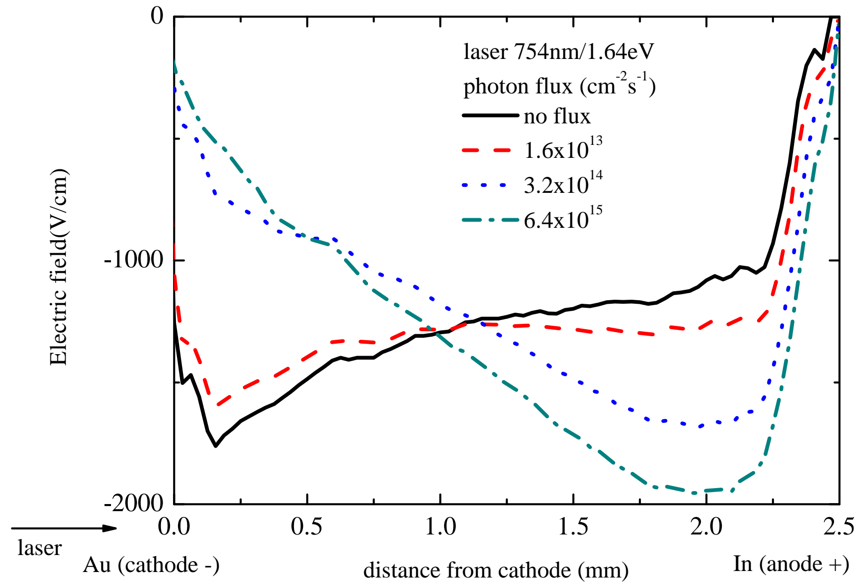

Figure 4.33: Distribution of the electric field through the sample for different photon flux at laser wavelength/photon energy 754 nm/1.64 eV, applied voltage on sample was 500V.

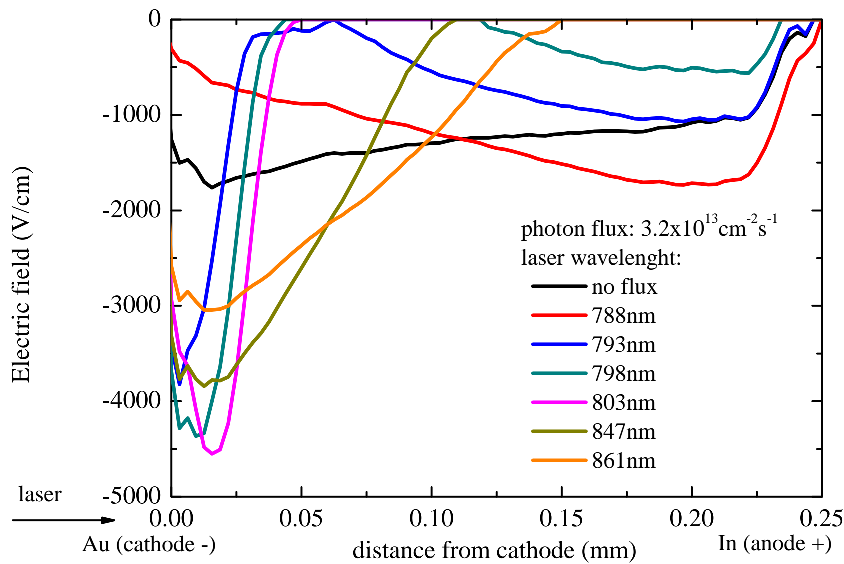

Figure 4.34: Electric field dependence on different excitation wavelengths of Ti:Sapphire laser. Constant photon flux $\Phi = 3.2 \times 10^{14}$ cm^{-2}s^{-1}, applied voltage on sample was 500V.

situation corresponds to a prevailing negative space charge accumulated in the sample. Thus the applied electric field is screened by a greater amount of negative charge accumulated at deep levels[5] and the slopes of lux-Ampere characteristics are lower than 1.

Electric field profiles for different laser wavelengths at a constant photon flux 3.2×10^{14} cm^{-2}s^{-1} measured by the Pockels effect are shown on fig.4.34. For

[5]This is a similar situation as described in section 4.3.1 for CdTe sample but with nearly constant electric field at initial 'no flux' condition

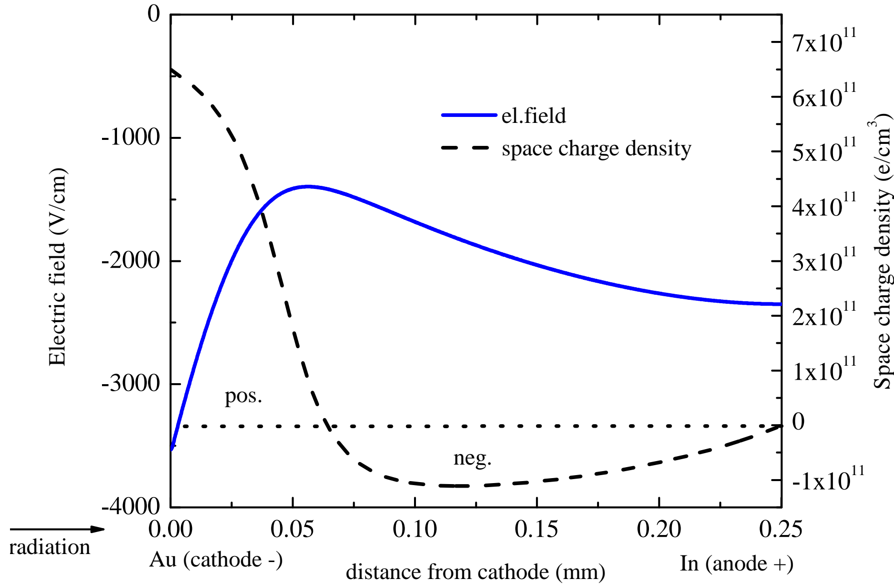

Figure 4.35: Numerical simulation of the distribution of the electric field and space charge density through the sample. Parameters: absorption coefficient $\alpha = 200$ cm^{-1}, photon flux $\Phi = 5 \times 10^{13}$ cm^{-2}s^{-1}. Applied voltage was 500V.

short excitation wavelength (788 nm), when the light is absorbed a few micrometers under the surface, the internal electric field is nearly constant, slightly decreasing under the cathode due to a presence of negative space charge at deep levels. There is a significant difference of electric field profiles for higher excitation wavelengths. The electric field is maximal near the cathode, then approaches its minimal value (pinch point) and is still decreased in the rest part of the sample. This situation corresponds to deeper penetration of the excitation laser light into the sample when both electrons and holes are generated in the thicker layer and both participate in the photoelectric transport. Theoretical models[6] of the electric field and space charge density distribution for the case of deeper light penetration (absorption constant $\alpha = 200$ cm^{-1}, photon flux $\Phi = 5 \times 10^{13}$ cm^{-2}s^{-1}) are shown on fig.4.35. There is a good qualitative agreement between theoretically modeled and experimentally acquired electric field distributions. The simulation of space charge density distribution points to the accumulation of positive space charge caused by holes trapped at the deep level during the drift to the cathode and a smaller amount of negative space charge caused by trapped electrons during the drift to the anode.

High values of slopes of lux-Ampere characteristics point to a high CCE of the detector. Comparing the results of lux-Ampere characteristics measured at a laser wavelength of 803 nm with the corresponding profile of the electric field it is evident, that the sample is strongly polarized (dead layer formed below the anode), but there is no apparent loss of charge in the steady-state measurement

[6]Based on the simulation described in section 2.6.

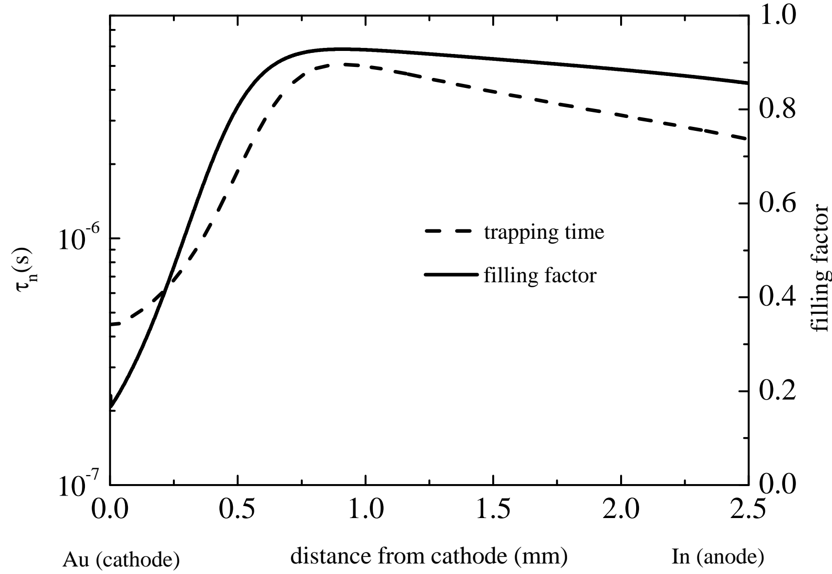

Figure 4.36: Simulation of the distribution of trapping time and filling factor through the sample. Parameters: absorption coefficient $\alpha = 200$ cm^{-1}, photon flux $\Phi = 1 \times 10^{14}$ cm^{-2}s^{-1}. Applied voltage was 500V.

up to very high fluxes (fig.4.31). This result is surprising, because such a strong weakening of the electric field should lead to a significant increase of the transit time resulting in charge losses. This discrepancy can be explained with the help of a theoretical simulation. The filling factor of the deep midgap level is shown on fig.4.36. According to this result this filling factor is quite high in the rear part of the sample, where the electric field is low. This area correlates with the region where the space charge is negative (fig.4.35). Electrons drifting to the anode were captured at the deep level and increase its occupation. The lower probability of electron capture results in an increase of electron life-time τ_n. So although the electrons are slowing down in a weak electric field, their life-time is long enough so that most of the electrons can reach the anode. These results were presented in ref. [109].

4.4 Laser excitation with IR spectral scanning

In order to find deep levels responsible for the polarization, we developed a new method that uses laser excitation of the sample and simultaneous tunable infrared illumination for spectral scanning. For the case when the cathode is illuminated by above band gap light as shown on fig.4.37a, deep level can be filled by a trapped photogenerated electrons traveling towards the anode as described in section 2.5. It is possible to use additional IR illumination with the wavelength tuned to the energy of transition of trapped electrons from the level into the conduction band to change the level occupation (see fig.4.37b). If those processes are associated

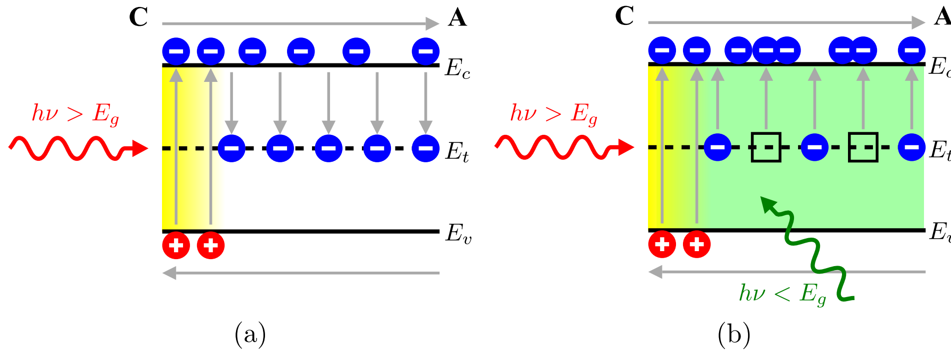

Figure 4.37: Principle of IR spectral scanning of the laser-excited sample for the case of above bandgap excitation ($h\nu > E_g$). The cathode (C) is illuminated by above band gap light (a), holes immediately recombine at the cathode and electrons can be trapped at the deep level E_t while traveling towards the anode (A). Additional IR illumination (b) with the wavelength tuned to the energy of transition of trapped electrons from the level into the conduction band can change the level occupation.

with the change of polarization of the detector, it is possible to study deep levels responsible for the polarization by measuring changes of the electric field profiles depending on the scanning light wavelength. The case of sub bandgap excitation wavelength is more complex and it will be discussed later in this section.

The cathode was illuminated with either 633 nm (1.96 eV) light from red diode laser or 954 nm (1.31 eV) light from tunable Ti:Sapphire laser to stimulate generation of carriers by an X-ray beam.

The 633 nm red laser acted as a source of electron-hole pairs generated just below the cathode due to a high absorption coefficient of the above bandgap light. The light with wavelength 954 nm generated by the Ti:Sapphire laser has below bandgap energy and therefore penetrated through the sample volume. The possibility of generating similar profiles of internal electric field by below bandgap laser light and by X-rays was demonstrated in the section 4.3.2.

IR spectral scanning measurements were performed only on samples no.1 and 3 because the sample no.5 showed negligible response of the electric field to the laser illumination.

4.4.1 Au/CdZnTe/In structure (Sample no.3)

Au/CdZnTe/In sample no.3 was simultaneously illuminated by infrared light (IR) from monochromator with a constant photon flux for wavelengths in the range of $0.85 - 2.3$ μm (corresponding photon energy $1.46 - 0.54$ eV) with equidistant steps 50 nm. This monochromatic light irradiated the side of the sample and it also penetrated through the sample volume. Scheme of this experiment is shown on fig.3.7.

The electric field through the sample shown on fig.4.38 is nearly constant without illumination. The band bending at both metal/CdZnTe interfaces is the-

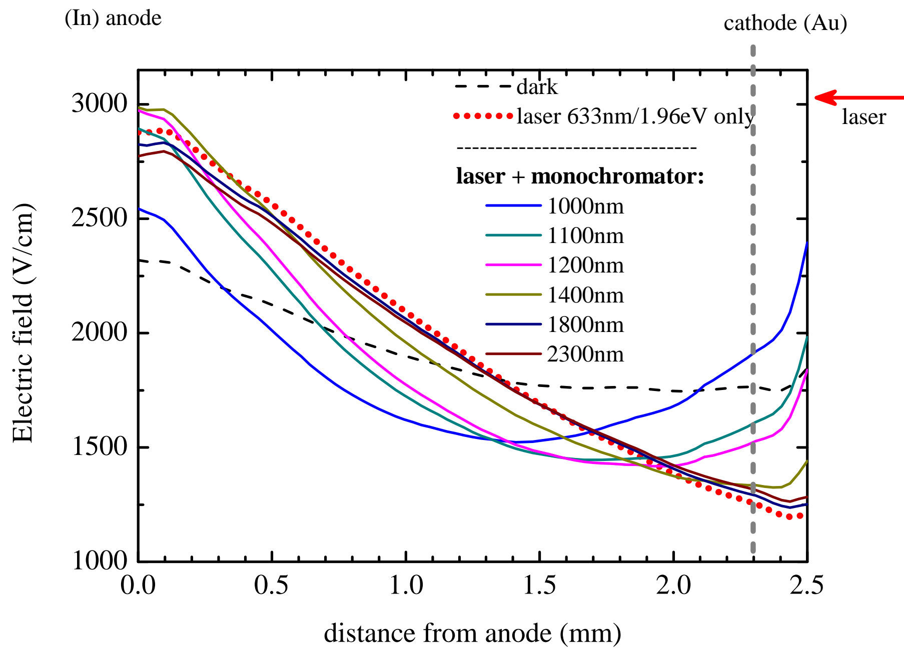

Figure 4.38: Profile of the electric field in the sample biased at 500V as a function of illumination with red laser (1.96 eV/633 nm) through the Au cathode and with red laser combined with IR light from the monochromator. The vertical dashed line indicates the position of a detailed profile shown on fig.4.40

refore negligible. The light from the above bandgap red laser light is absorbed just below the cathode and generates electron-hole pairs in the near-cathode region. Electrons drift in the applied electric field to the anode. On their way they can be captured at deep levels and create negative space charge. Holes practically immediately recombine on the cathode and do not contribute to the induced signal. If sub-bandgap light from infrared laser is used the sample volume is nearly homogeneously illuminated since the photon energy (1.31 eV) is just less than the bandgap energy ($\sim$ 1.54 eV at 300 K). In this case both electrons and holes drift to the electrodes and can be captured at deep traps. Depending on the parameters of the levels (concentrations, capture-cross sections) either positive or negative space charge prevails and can be detected by the Pockels effect.

In order to receive spectral information on energies where the space charge is accumulated, the sample was simultaneously illuminated with light from a monochromator with approximately the same intensity as that of the laser (photon flux $\Phi \sim 10^{13} - 10^{14}\ \ \mathrm{cm}^{-2}\mathrm{s}^{-1}$). The changes in the profile of the electric field dependent on the wavelength of the monochromator were observed. Fig.4.38 shows profiles of the electric field without any illumination, with illumination of 633 nm laser light, and finally with both the laser and monochromator illumination (Electric field profiles for only several wavelengths are shown for a better readability).

The electric field, which is nearly constant without illumination, decreases

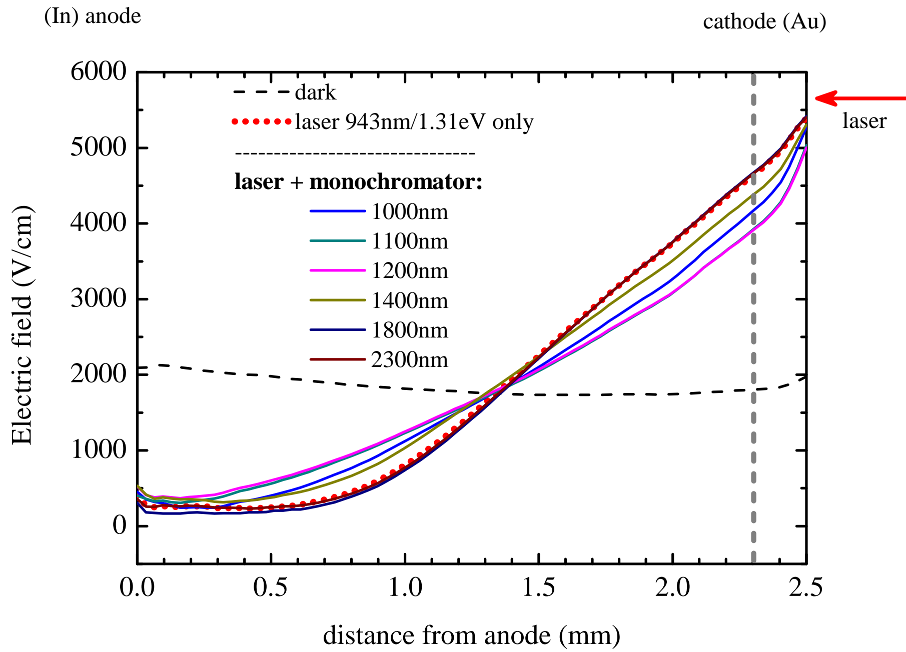

Figure 4.39: Profile of the electric field in the sample biased at 500V as a function of illumination with infrared laser (1.31 eV/943 nm) through the Au cathode and with infrared laser combined with IR light from the monochromator. The vertical dashed line indicates the position of a detailed profile shown on fig.4.40

below the cathode after red laser illumination. This decrease can be explained by the formation of negative space charge in the volume of the sample due to electron trapping as shown in previous sections. After application of infrared light from the monochromator the electric field has a tendency to increase below the cathode. The negative space charge in this part of the sample is also decreasing. This result can be explained by de-trapping of electrons from deep levels after IR illumination.

The results of the same experiment using the infrared Ti:Sapphire laser are presented on fig.4.39. Now the IR laser light penetrates through the whole sample. The processes of carrier emissions from deep levels and subsequent trapping and recombination finally lead to the deformation of the electric field which is opposite to that observed on fig.4.38. Now the electric field increases below the cathode. This corresponds to the presence of positive space charge in the sample volume due to IR laser illumination. When we additionally applied the IR light from the monochromator, the electric field has again a tendency to regain its profile, i.e. it is decreasing below the cathode when the energy of the IR light from the monochromator increases. The conclusion is that illumination of the sample with this IR light decreases the positive space charge in the volume. This result can be explained by de-trapping of holes from deep levels.

In order to investigate spectral information about the energies of deep levels where the space charge is localized the specific position close to the cathode at

$x = 2.3$ mm in the sample was chosen and depicted the dependence of the electric field $\mathcal{E}(x)$ on the energy of infrared light from the monochromator. The summary of the results is shown on fig.4.40.

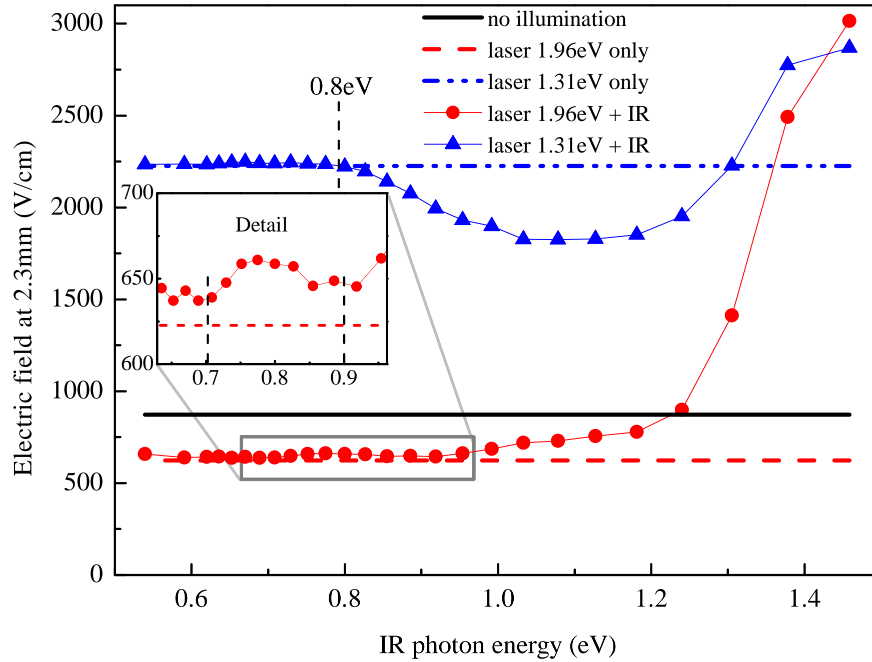

Figure 4.40: Dependence of electric field on illumination at position $x = 2.3$mm

The full circles on fig.4.40 represent the result of the combined application of the red laser and the monochromator. It is characterized by two thresholds (~ 0.7, ~ 0.9 eV) corresponding to de-trapping of electrons from these deep levels. The triangles show the profile of the electric field at position $x = 2.3$ mm for the case of simultaneous illumination with infrared laser with energy 943 nm and IR light from the monochromator. The decrease in the electric field starting at 0.8 eV corresponds to de-trapping of holes from this deep level. The scheme of energy levels in the bandgap that are effective in trapping and de-trapping is presented on fig.4.41. An error of found energy levels is estimated to be 0.05 eV. These results presented in ref. [110].

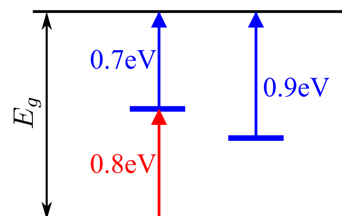

Figure 4.41: Scheme of energy levels in CdZnTe participating in the formation of space charge due to the trapping of photo-generated carriers.

The increase on both curves at $\sim$ 1.25 eV can be interpreted as a result of additional generation of electron-hole pairs by the monochromator when the energy is approaching the position of the main photoconductivity peak localized close to the bandgap energy ([111] and fig.4.30). The increase in positive space charge and thus the electric field below the cathode observed in the experiment can be explained by prevailing trapping of holes. This fact is not surprising due to a much smaller mobility of holes ($\sim$ 50 $cm^2V^{-1}s^{-1}$) compared with electrons ($\sim$ 700 $cm^2V^{-1}s^{-1}$) in CdTe at 300 K [112].

4.4.2 Au/CdTe/In structure (Sample no.1)

A similar study exploiting IR spectral scanning was performed on the sample no.1.

The distribution of the electric field in the sample without illumination is shown in fig.4.42 (black curve). This electric field is tilted and has its maximum just under the cathode. This is an effect of band bending at the CdTe/Au interface. Because higher electric field is near the cathode the space charge present in the sample is positive.

We applied a red laser excitation at the wavelength 633 nm (photon energy 1.96 eV). The sample was illuminated through the cathode. The electric field became more flat after this type of illumination (solid red line in fig.4.42). Photons with energy above the bandgap of the sample are absorbed within a thin layer under the cathode where electron-hole pairs are generated. Holes drift to the cathode and recombine quickly at the contact. Electrons drift through the whole sample volume to the anode and can be trapped at those deep levels which are empty due to the bands bent upwards at the CdTe/Au interface. This way the positive space charge is partially compensated by electron trapping, as shown earlier on fig.4.26, and the electric field becomes more constant in the sample.

Applying additional IR spectral scanning (fig.4.42 - dashed lines) we can determine energy levels responsible for laser induced space charge accumulation. Changes in the occupation of these levels result in change of magnitude and distribution of the space charge which finally modifies the profile of the electric field. The spectral dependence of the electric field in two positions x close to the cathode is shown on fig.4.43.

We have evaluated deep levels at energies $E_1 = 0.69$ eV and $E_3 = 0.84$ eV in spectral positions, where the electric field increases after application of the additional infrared light (the slope of the E-field profile changes). This represents a step back to the original state (no illumination), where the positive space charge in the sample caused a higher value of the electric field under the cathode. We interpret the increase of the electric field with the additional IR-illumination at energies E_1 and E_3 as a result of optical excitation of electrons trapped at these

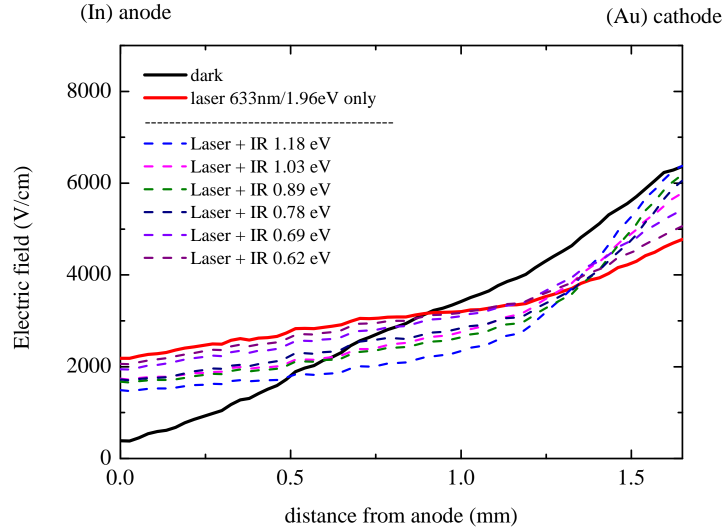

Figure 4.42: Electric field profile under 1.96eV laser illumination with IR spectral scanning.

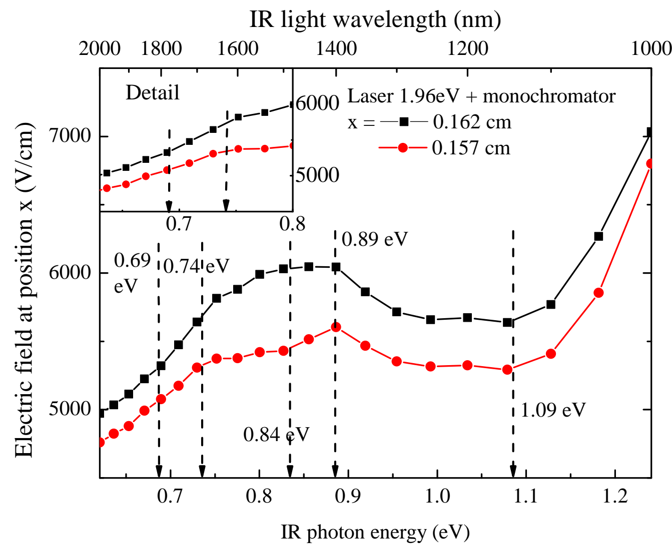

Figure 4.43: Spectral dependence of the electric field on IR scanning at the distance x from the anode. Laser 633nm/1.96eV.

deep levels to the conduction band. This way the positive space charge present in the sample due to band bending starts again to increase and influences the profile of the electric field.

Other two changes of the electric field from fig.4.43 happen at energies at $E_2 \sim 0.74 - 0.75$ eV and $E_4 = 0.89$ eV. At these energies the electric field starts to decrease. This represents an opposite effect to the one described above. We assume that this process is associated with a transition of electrons from the valence band to deep levels and a formation of a negative space charge. We note that the sum of $E_1 + E_4 = 1.58$ eV equals to $E_2 + E_3 = 1.58$ eV. Therefore we assume that E_1 and E_4 represent transitions between the conduction and valence

bands[7] of one deep level located approximately ~ 0.69 eV from the conduction band. A similar argumentation applies for E_2 and E_3 localizing the deep level at ~ 0.84 eV below the conduction band.

In the next step we replaced the red laser with an infrared laser at energy 1.31 eV. Sub-bandgap illumination can penetrate the whole sample and we can assume a homogeneous interaction of IR photons in the sample in contrast to the illumination with an above-bandgap red laser. While the red laser generates free carriers in a similar way as low energy X-ray photons or alpha-particles (just under the electrode), the IR laser radiation forms free carriers in the whole sample volume, i.e. comparable with the influence of high energy X-ray photons.

The electric field after illumination with the 1.31 eV IR laser is shown on fig.4.44. Without the illumination the field is tilted due to the positive space charge induced by the band bending at the metal/semiconductor interface as before. With the infrared laser illumination the electric field tilts even more, leaving the sample more polarized. We interpret this fact as a result of trapping of holes at deep levels. With additional monochromator light we can investigate the deep levels which accumulate the space charge causing the polarization. Spectral dependence of the electric field in points near the cathode is shown on fig.4.45. Evaluation of these profiles reveals the same energies of deep level energies as with illumination with the laser at 1.94 eV.

In both measurements with the red and infrared laser there is another deep level visible at $E_5 = 1.09$ eV. The energy scheme of the found deep levels is shown on fig.4.46.

Comparing figs.4.41 and 4.46 we conclude that deep levels responsible for the radiation induced polarization at energies ~ 0.7 eV and $\sim 0.84 - 0.9$ eV are present in both studied samples (no.1: CdTe:In and no.3: CdZnTe). The origin of these energy levels is discussed in more detail in chapter 6.

[7]Estimated error of level energies is 0.05 eV based on the reading of the changes of the electric field profiles from figs. 4.45 and 4.43. Therefore the sum of energies of complementary levels may slightly differ from E_g.

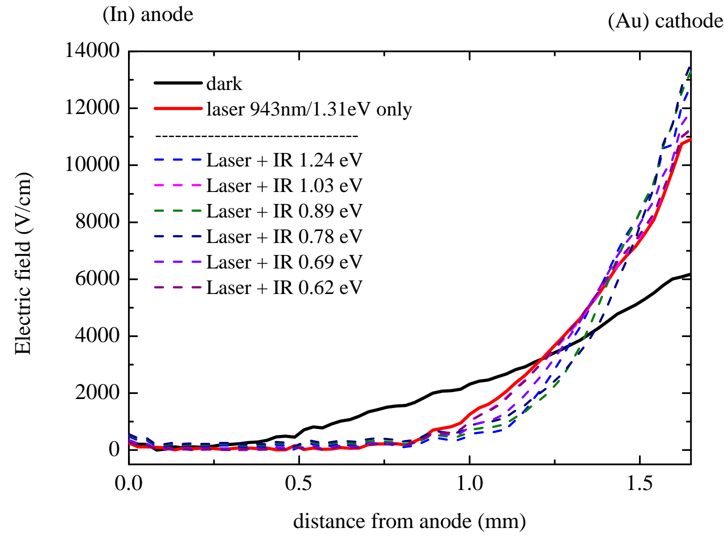

Figure 4.44: Electric field profile under 1.31eV laser illumination with IR spectral scanning.

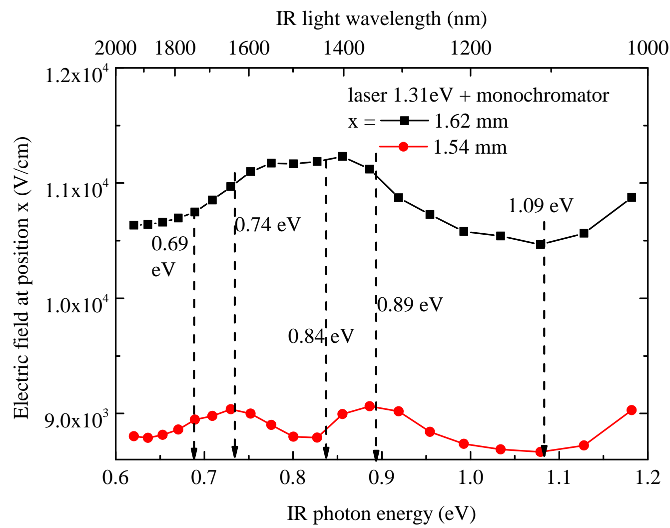

Figure 4.45: Spectral dependence of the electric field on IR scanning at the distance x from the anode. Laser 943nm/1.31eV.

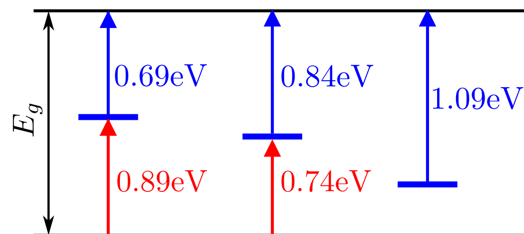

Figure 4.46: Scheme of energy levels in CdZnTe participating in the formation of space charge due to the trapping of photo-generated carriers.

Chapter 5

Results II: Discharge current measurements

We have applied an additional method to study the deep levels in CdTe and CdZnTe samples. This discharge current method requires a presence of a Schottky barrier. We have used this method to study the samples no.1, 3, 4 and 5, where we are able to prepare the barrier. In the case of the sample no.1 the measured data were very scattered and the results could not be analyzed. Therefore we present only the results of measurements performed on samples no.3, 4 and 5 in this chapter.

5.1 N-type CdZnTe (sample no.5)

The profile of the electric field received from analysis of Pockels effect measurements at room temperature and applied voltage of 250 V is presented on fig.4.13. It can be clearly seen that the field is concentrated below the cathode, which corresponds to the presence of positive space charge in the sample. The electric field is slowly changing its profile in time and this dependence is also temperature dependent (see sec. 4.2.2).

The value of work function of Au (Φ_{Au}) is approximately 5.3 eV and the work function in semi-insulating CdTe and CdZnTe ranges from 5.1-5.5 eV in dependence on the position of the Fermi level in the near-midgap region. Therefore the band bending at the interface of Au and the n-type CdZnTe with resistivity $10^7 - 10^8$ Ωcm can be estimated to approx. 200 meV (bands bent upwards).

The corresponding band diagram of the studied sample with Au contacts is presented on fig.5.1 (without an applied voltage). Immediately after application of the voltage the bands start to tilt. Electrons are de-trapped from near midgap levels (sec.4.2.2). At the same time holes are injected from the cathode and trapped at deep levels. Therefore the total positive space charge is formed by

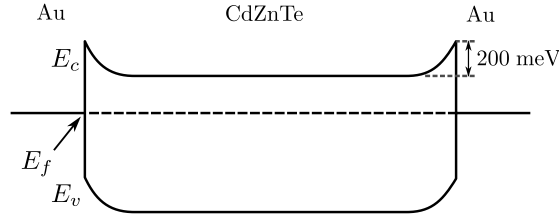

Figure 5.1: Band diagram of the sample no.5 without applied voltage.

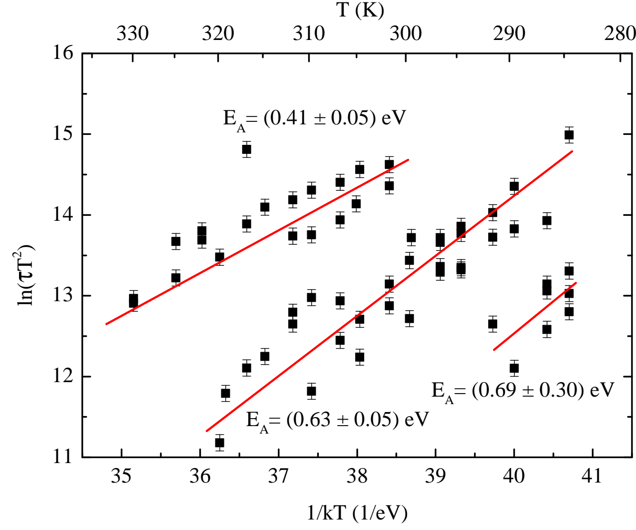

Figure 5.2: Arrhenius plot with the evaluation of parameters of deep acceptor levels. Sample no.5.

combination of these two processes. After switching off the voltage the sample tends to achieve equilibrium and the positive space charge decreases. The electric current can be measured by the electrometer. The current decreases with time and the current dependence $I(t)$ can be approximated by a double exponential (see eq.3.10). We have observed, that this process is thermally activated. Time constants τ_1 and τ_2 were obtained from double exponential fit of time evolution of discharge current measurement and at different temperatures in the range of 280K and 340K. The observed decrease of the positive space charge can in principle be explained by opposite processes to those leading to its formation - trapping of electrons and de-trapping of holes. We interpret the time and temperature evolution of the discharge current by de-trapping of holes at deep levels, because this process is thermally activated while trapping of electrons is not.

Using standard approach of Arrhenius analysis described in section 2.9.2 we have received an Arrhenius plot (fig.5.2) and observed three deep hole traps E_t active in the studied temperature range and their capture cross-sections. Errors of E_t were calculated as errors of linear fits. Statistical errors of fitted time constants vary between 5% and 10% (see error bars in fig.5.2). These levels calculated from the edge of the valence band are responsible for initial formation of positive space charge by hole trapping immediately after application of the voltage (fig.4.13).

In comparison with other publications [2, 51] cadmium vacancies (V_{Cd}) may be responsible for levels

$$E_{t1} = E_v + 0.41(\pm 0.05) \text{ eV } (\sigma = 10^{-19} - 10^{-21} \text{ cm}^2),$$
$$E_{t2} = E_v + 0.63(\pm 0.05) \text{ eV } (\sigma = 10^{-15} - 10^{-17} \text{ cm}^2).$$

The error of evaluated energy of the level

$$E_{t3} = E_v + 0.7(\pm 0.3) \text{ eV } (\sigma = 10^{-13} - 10^{-15} \text{ cm}^2)$$

is too high and it is therefore not comparable with other results. These results were presented in ref. [113]

5.2 Semiinsulating CdZnTe (samples no.3 & 4)

We have compared results of Discharge Current measurements acquired on two neighboring semi-insulating CdZnTe samples with different contact metals. Sample no.3 was equipped with gold and indium contacts. In this case, Indium bends band downwards and gold upwards (fig.5.3a), so both types of carriers are injected after the application of bias and it was impossible to distinguish if activation energy E_A is calculated from the conduction or the valence band. On the other hand, sample no.4 was equipped with both gold contacts bending bands upwards (fig.5.3b) so we expected injections of holes and therefore activation energy is calculated from the valence band only.

Arrhenius plots with the evaluation of activation energy E_A of samples no.3 and 4 are shown on figs.5.4 and 5.5, respectively.

We can see that the level with activation energy about 0.4 eV (with capture cross-section ranging between $10^{-18} - 10^{-21}$ cm^2) appears in both cases, so it should be the same level, it is calculated from the valence band and its origin is probably cadmium vacancy (as well as for the sample no.5 in the previous section). Further level with activation 0.51 eV appears only in the case of sample no.3 and it should be an electron trap calculated from the conduction band. Shallow level 0.18 eV is observed in the sample no.4 and it is calculated from the valence band.

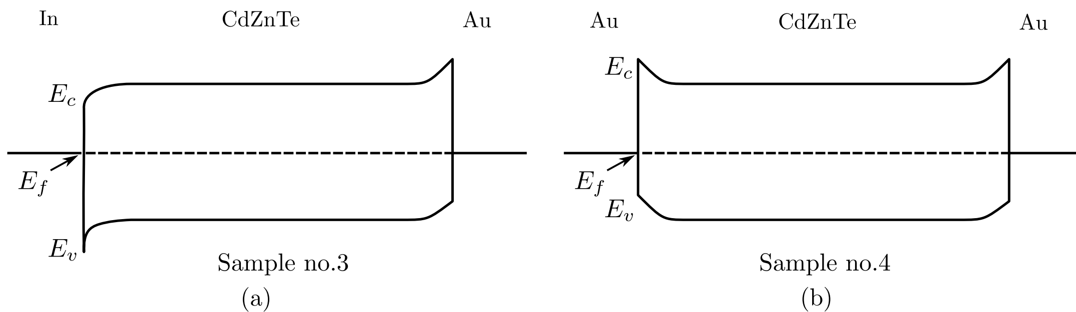

Figure 5.3: Band diagram of the samples no.3 and 4 without applied voltage.

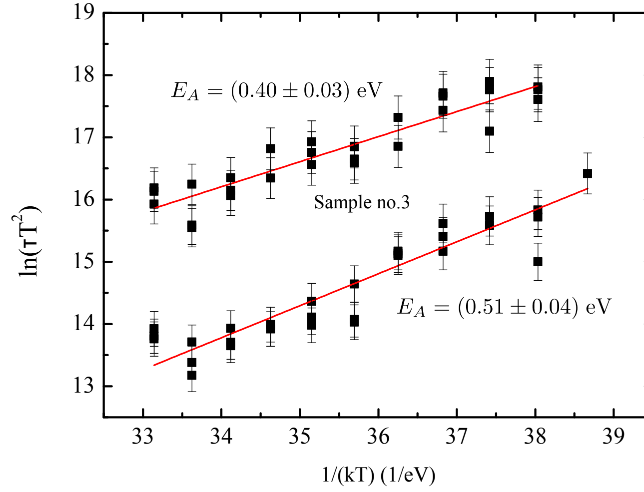

Figure 5.4: Arrhenius plot with the evaluation of activation energy E_A. Sample no.3.

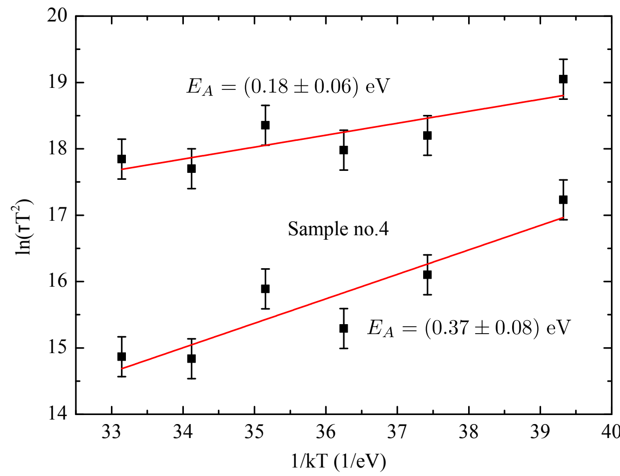

Figure 5.5: Arrhenius plot with the evaluation of activation energy E_A. Sample no.4.

Finally we got the following energy levels:

Sample no.3: $E_{t1} = E_v + 0.40(\pm 0.03)$ eV $(\sigma = 10^{-18} - 10^{-20}\ \mathrm{cm}^2)$,
$E_{t2} = E_c - 0.51(\pm 0.04)$ eV $(\sigma = 10^{-19} - 10^{-21}\ \mathrm{cm}^2)$,

Sample no.4: $E_{t1} = E_v + 0.37(\pm 0.08)$ eV $(\sigma = 10^{-19} - 10^{-21}\ \mathrm{cm}^2)$,
$E_{t3} = E_v + 0.18(\pm 0.05)$ eV $(\sigma = 10^{-23} - 10^{-25}\ \mathrm{cm}^2)$.

5.3 Discussion: capture cross-sections

Extremely low values of evaluated capture cross-sections can be explained by strong re-trapping effect. Commonly assumed existence of a recombination level with energy E_r, capture cross-section σ_r and concentration N_t in the material does not allow re-trapping of thermally emitted carriers at the studied deep level E_t $(\sigma_t,\ N_t)$ if $\sigma_t N_t \ll \sigma_r N_r$. It means that all recombination processes happen at

the recombination level E_r, that cannot be detected by methods based on thermal emission, because it does not emit any carriers.

On the other hand, if an influence of the recombination level is negligible when $\sigma_t N_t \gg \sigma_r N_r$, the evaluated values of capture cross-section of the deep level E_t can be orders of magnitude lower than the realistic value. This situation is reflected in the Arrhenius plot, where all the measured data are systematically shifted towards higher values (fig.5.6). According to eqs.2.72 used for the evaluation of level activation energy and cross-section, we can see that the values of cross-sections can be affected by strong re-trapping, while activation energies not. This topic is described in detail in ref. [114].

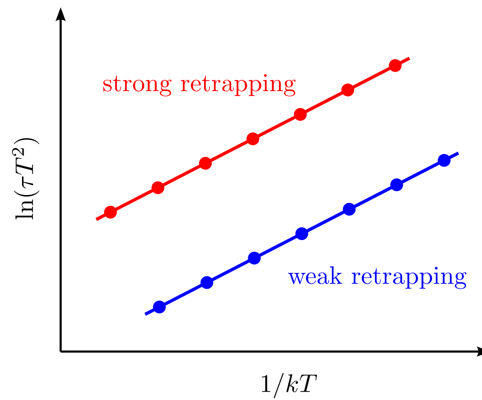

Figure 5.6: Schematic Arrhenius plot of one deep level E_t for cases of weak and strong retrapping.

Chapter 6

Results III: Summary of observed energy levels

Time and temperature dependent (PTD, sections 4.2.1 and 4.2.2) and IR spectral scanning (PIR, section 4.4.1) Pockels effect measurements were performed in order to receive information about energy levels responsible for the polarization. Energy levels and their parameters observed by PTD, PIR and discharge current measurements (DCM) are presented in table 6.1 and depicted on fig. 6.1.

The origin of those levels is under the discussion and it is still not clear. Although the determination of origins of energy levels is out of the scope of this thesis and it requires a complex analysis of large number of samples with different growth, doping and annealing conditions, comparing with the literature it is possible to estimate defects responsible for found levels and the role of those levels in polarization of detectors. Moreover, different spectroscopy methods can show slightly different activation energies of the same energy levels, because thermal transitions are possible due to the assistance of phonons (DCM and PTD), while optical transitions not (PIR). We can concentrate mostly on native (all the samples) and indium (CdTe:In sample no. 1) related defects. Extremely low values of evaluated capture cross-sections acquired from DCM measurements can be explained by strong re-trapping effect discussed in section 5.3.

Acceptor level F is probably related to ionized cadmium vacancy V_{Cd}^{-}, observed by Huang et al. (ref. [57]) on different samples (undoped CdTe, CdTe:Al and $Cd_{0.9}Zn_{0.1}Te$). An origin of donor level I that is doubly ionized interstitial cadmium Cd_{I}^{2+} according to the ref. [115]. Levels G, H and M with activation energies around $E_v + 0.4$ eV are associated with doubly charged V_{Cd}^{2-} [51, 65, 115]. All the levels mentioned above are not responsible for the polarization.

On the other hand, based on our findings, all the deep levels A-E, J-L, N and O are related with polarization. Observed activations energies of deep levels are affected by relatively high variance and some of them have mutually complementary energies.

Levels B, L, N and O are probably related to the level $E_v + 0.62(\pm 0.02)$ eV observed by Cola et al. [2] using PTD method performed on CdTe:Cl. It is unclear if this level is associated with V_{Cd} [2] or Cd_I [51].

Levels A, J, and K are probably related to the level $E_v + 0.76$ eV observed by Castaldini et al. in various samples (CdTe:Cl, undoped CdTe and $Cd_{0.8}Zn_{0.2}Te$). They concluded that this level has a donor-like character and it is associated with complex of doubly ionized cadmium vacancy V_{Cd}^{2-} and it pins the Fermi level close to the midgap [116, 117].

Deep donor level E is common to CdTe samples as it was seen in a number of investigations. Castaldini et al. [51] has presented a deep level at energies 1.1 eV below the bandgap to be a positively charged tellurium vacancy V_{Te}^{+}. Other authors [118] attribute this energy level to dislocations induced by Te secondary defects (inclusions/precipitates).

It is evident that native defects, especially cadmium vacancies, act as dominant defects responsible for the polarization in (CdZn)Te detectors.

Sample no.	level	E_t(eV)	$\sigma_{n(p)}$(cm^2)	Method†	Note‡
1	A	$E_c - 0.77(\pm 0.02)$	6×10^{-13}	PTD	P $\bullet$
1	B	$E_c - 0.8(\pm 0.04)$	10^{-11}	PTD	P $\circ$
1	C	$E_c - 0.69(\pm 0.05)$		PIR	P $\bullet$
1	D	$E_c - 0.84(\pm 0.05)$		PIR	P $\circ$
1	E	$E_c - 1.09(\pm 0.05)$		PIR	P
4	F	$E_v + 0.18(\pm 0.05)$	10^{-24}	DCM	
4	G	$E_v + 0.37(\pm 0.08)$	10^{-20}	DCM	$\diamond$
3	H	$E_v + 0.4(\pm 0.03)$	10^{-19}	DCM	$\diamond$
3	I	$E_c - 0.51(\pm 0.04)$	10^{-20}	DCM	
3	J	$E_c - 0.70(\pm 0.05)$		PIR	P $\bullet$ +
3	K	$E_v + 0.80(\pm 0.05)$		PIR	P $\bullet$ +
3	L	$E_c - 0.90(\pm 0.05)$		PIR	P $\circ$
5	M	$E_v + 0.41(\pm 0.05)$	10^{-20}	DCM	$\diamond$
5	N	$E_v + 0.63(\pm 0.05)$	10^{-16}	DCM	P $\triangleleft$ $*$
5	O	$E_c - 0.92(\pm 0.06)$	3.5×10^{-13}	PTD	P $\triangleleft$ $*$

Table 6.1: Summary of energy levels.
†) PTD ... Pockels effect-time and temperature dependence, PIR ... Pockels effect-IR spectral scanning, DCM ... Discharge current measurements.
‡) P ... levels responsible for polarization, $\bullet$, $\circ$, $\diamond$, and $\triangleleft$ ... same levels, + and $*$ ... complementary levels.

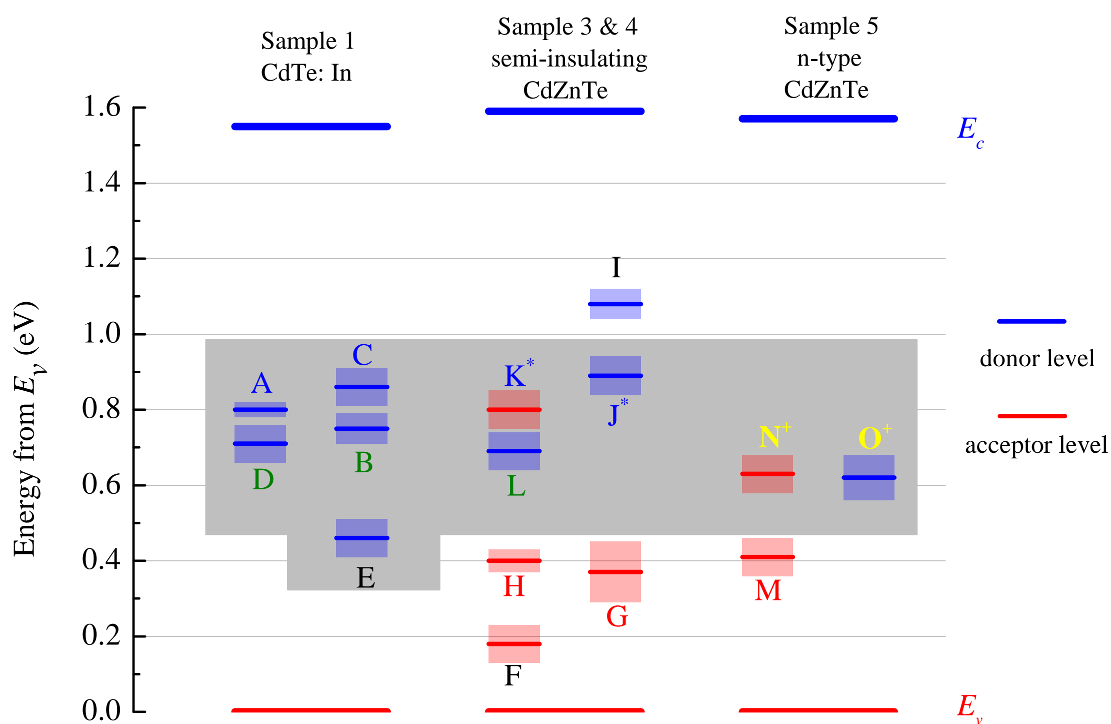

Figure 6.1: Summary of energy levels. Same color (except of black) of letters of levels designation means highly probably the levels with the same origin, + and ∗ ... complementary levels. Gray filled area indicates levels responsible for the polarization.

Chapter 7

Summary and conclusions

In order to study the polarization phenomenon in (CdZn)Te detectors, the setup for Pockels effect measurements was assembled at Institute of Physics of Charles University. It allows to study internal electric field profiles in detectors under variable illumination conditions using tunable Ti:Sapphire laser and different temperatures. It has been proven that it is possible to use laser radiation instead of X-rays to study electric field distribution under high radiation fluxes (sections 4.3.1 and 4.3.2).

A new method of deep level spectroscopy was developed during the work on this thesis. It is based on modified setup of Pockels effect measurement exploiting infra red spectral scanning. We also implemented temperature dependent measurement of discharged currents to study trapping of electric charge at deep levels.

Three sets of n-type conductivity samples with different resistivity equipped with gold and/or indium contact metals have been studied (table 3.2). We have investigated an influence of contact metals and high flux excitation on polarization and we have found deep levels responsible for that.

We have observed that gold bends band upwards at metal-semiconductor interface for n-type material with resistivity $\leq 10^9$ Ωcm and it forms Schottky barrier, while there is almost no band bending in the case of high resistivity ($\sim 10^{10}$ Ωcm) and gold acts as nearly Ohmic contact. Band bending leads to a time dependent polarization of the detector in dark conditions due to the accumulation of electrically injected charge carriers trapped at deep levels forming positive space charge under gold cathode. The observed band bending at Au/(CdZn)Te interface corresponds well with the model based on difference of work functions (section 2.2). On the other hand, the observed band banding between indium and CdTe is much lower than supposed probably due to the dipoles formed at the interface due to a presence of a thin oxide layer between indium and CdTe (section 4.3.1).

Based on the electric field measurements performed uder X-ray and laser excitation supported with numerical simulations we have found that high flux

low energy X-rays and above gap laser illumination lead to an accumulation of negative space charge at deep levels when irradiated contact acts as a cathode (this corresponds to shallow penetration of radiation), while sub gap laser illumination leads to an accumulation of positive space charge (deep penetration of radiation into the sample and it should correspond to high energy X-rays). This accumulated space charge can lead to the radiation induced polarization from a certain intensity of excitation. Space charge accumulated at deep levels due to high flux conditions has comparable concentration as a space charge present due to the band bending at M-S interface and those space charges can interact and it leads to the so called radiation induced depolarization (sections 4.3.1 and 4.4.1). This phenomenon could be possibly exploited in the next generation detectors by using additional illumination (for example light-emitting diodes) in order to suppress radiation induced polarization under high flux X-ray conditions.

We have observed that energy levels responsible for the polarization in studied detectors are located close to the midgap (between approx. $E_v + 0.45$ eV and $E_v + 0.95$ eV) and they are probably related to native crystal defects, especially cadmium vacancies.

We can conclude, that although the deep levels are responsible for the polarization that can be undesirable during the detector operation, they play an important role in the compensation processes in high resistivity (CdZn)Te detector materials. So it is necessary to pay attention to the polarization effect during the development of "high flux" detector devices and control the polarization itself.

References

[1] Grill, R., Franc, J., Höschl, P., Belas, E, Turkevych, I., Turjanska, L. and Moravec, P., *Semiinsulating CdTe*, Nucl. Instr. Meth. A. 487 (2002), p. 40.

[2] Cola, A. and Farella, I., *The polarization mechanism in CdTe Schottky detectors*, Appl. Phys. Lett. 94 (2009), p. 102113.

[3] Yao, H. W., James, R. B. and Erikson, E. C., *Optical characterization of the internal electric field distribution under bias of (CdZn)Te radiation detectors*, Proc. SPIE. 3115 (1997), p. 62.

[4] Bolotnikov, A. E., Camarda, G. S., Cui, Y., Hossain, A., Yang., G., Yao, H. W. andJames, R. B., *Internal Electric-Field-Lines Distribution in CdZnTe Detectors Measured Using X-Ray Mapping*, IEEE T. Nucl. Sci. 56 (2009), p. 791.

[5] Cola, A., Farella, I., Mancini, A. M. and Donati, A., *Electric field properties of CdTe nuclear detectors*, IEEE Trans. Nucl. Sci. 54 (2007), p. 868.

[6] Toyama, H., *Analysis of polarization phenomenon and deep acceptor in CdTe radiation detector*, IEEE Nuclear Science Symposium Conference Record (2006), p. 3694.

[7] Farella, I., Montagna, G., Mancini, A. M. and Cola, A., *Study of Instability Phenomena in CdTe Diode-like Detectors*, IEEE Trans. Nucl. Sci. 56 (2009), p. 1736.

[8] Grill, R., Belas, E., Franc, J., Bugár, M., Uxa, Š., Moravec, P. and Höschl, P., *Polarization study of defect structure of CdTe radiation detectors*, IEEE Trans. Nucl. Sci. 58 (2011), p. 3172.

[9] Matsumuto, C., Takahashi, T., Takizawa, K., Ohno, R., Ozaki, T., Mori, K., *Performance of a new schottky CdTe detector for Hard X-ray spectroscopy*, IEEE Trans. Nucl. Sci. 45 (1998), p. 428.

[10] Okada, K., Sakurai, Y. and Suematsu, H., *Characteristics of both carriers with polarization in diode-type CdTe x-ray detectors*, Appl. Phys. Lett. 90 6 (2007), p. 063504.

[11] Bell, R. O., Entine G., and Serreze, H. B., *Time-dependent polarization of CdTe gamma-ray detectors*, Nucl. Instrum. Methods. 117 (1974), p. 267.

[12] Sellin, P. J., Prekas, G., Franc, J., and Grill, R., *Electric field distributions in CdZnTe due to reduced temperature and x-ray irradiation*, Appl. Phys. Lett. 96 13 (2010), p. 133509.

[13] Washington, A. L., Teague, L. C., Duff M. C., Burger A., Groza M. and Buliga, V., *Wavelength dependence on the space charge collection in CdZnTe detectors*, J. Appl. Phys. 111 (2013), p. 113715.

[14] Cola, A. and Farella, I., *Electric Field and Current Transport Mechanisms in Schottky CdTe X-ray Detectors under Perturbing Optical Radiation*, Sensors 13 (2013), p. 9414.

[15] Franc, J., Dědič, V., Sellin, P. J., Grill, R. and Veeramani, P., *Radiation induced control of electric field in Au/CdTe/In structures* Appl. Phys. Lett. 98 (2011), p. 232115.

[16] Prokesh, M., Bale, D. S. and Szeles, C., *Fast high-flux Response of CdZnTe X-ray detectors by optical manipulation of deep level occupations*, IEEE Trans. Nucl. Sci. 57 (2010), p. 2397.

[17] Bale, D. S. and Szeles, C., *Nature of polarization in wide-bandgap semiconductor detectors under high-flux irradiation: Application to semi-insulating* $Cd_{1-x}Zn_xTe$, Phys. Rev. B. 77 (2008), p. 035205.

[18] Fiederle, M., Feltgen, T., Meinhardt, J., Rogalla, M. and Benz, K. W, *State of the art of (Cd, Zn)Te as gamma detector*, Journal of Crystal Growth 197 (1999), p. 635.

[19] Bruder, M., Schwarz, H. J., Schmitt, R., Maier, H., Möller, M. O., *Vertical Bridgman growth of* $Cd_{1-y}Zn_yTe$ *and characterization of substrates for use in* $Hg_{1-x}Cd_xTe$ *liquids phase epitaxy*, Journal of Crystal Growth 101 (1990), p. 266.

[20] Doty, F. P., Schetzina, J. F., Butler, J. F. and Bowers, K. A., *Properties of CdZnTe crystals grown by a high pressure Bridgman method*, J. Vac. Sci. Technol. B 10 (1992), p. 1418.

[21] Butler, J. F., Apotovsky, B., Niemela, A. and Sipila, H., *Sub-keV resolution detection with* $Cd_{1-x}Zn_xTe$ *detectors*, X-Ray Detector Physics, Applications, Proceedings of the SPIE, Vol. 2009 SPIE, Bellingham, WA (1993), p. 121.

[22] Horodyský, P., *Optical properties of* $Cd_{1-x}Zn_xTe$*: Doctoral thesis*, Institute of Physics of Charles University, Prague 2006.

[23] Green, M. A., Emery, K., Hishikawa, Y., Warta, W. and Dunlop, E. D., *Solar cell efficiency tables (version 42)*, Progress in Photovoltaics: Research and Application 21 (2013), p. 827.

[24] Palmer, D. W., *www.semiconductors.co.uk, 2008.03*, [online]. [cit. 2014-03-04]. Available at: `http://www.semiconductors.co.uk/propiivi5410.htm#CdS,CdSe,CdTe`,

[25] Keifer, J. E. and Yariv, A., *Electrooptic Characteristics of CdTe at 3.39 and* 10.6μ, Appl. Phys. Lett. 15 (1969), p. 26.

[26] McLellan, E. J. and Figueira, J. F., *Ultrafast Pockels cells for the infrared*, Rev. Sci. Instrum. 50 (1979), p. 1213.

[27] EV Products & Kromek comp.: *Semiconductor Detector Material Properties*, EV PRODUCTS & KROMEK COMP. [online]. [cit. 2013-11-22]. Available at: `http://evproducts.com/pdf/material_prop.pdf`,

[28] Hecht, K., *Zum Mechanismus des lichtelektrischen Primärstromes in isolierenden Kristallen*, Zeitschrift für Physik. 77 (3-4) (1932), p. 235.

[29] Luke, P. N., *Single-Polarity Charge Sensing in Ionization Detectors Using Coplanar Electrodes*, Applied Physics Letters 65 1994), p. 2884.

[30] Barrett, H. H., Eskin, J. D. and Barber, H. B., *Charge - transport in arrays of semiconductor gamma-ray detectors*, Physical Review Letters 75 1 (1995), p. 156.

[31] Shor, A., Eisen, Y. and Mardor, I., *Optimum spectroscopic performance from CZT gamma- and X-ray detectors with pad and strip segmentation*, Nuclear Instruments & Methods in Physics Research Section a-Accelerators Spectrometers Detectors and Associated Equipment 428 1 (1999), p. 182.

[32] Knoll, G. F., *Radiation detection and measurement*, 4th ed. Hoboken, N.J.: John Wiley, xxvi, 830 p. (2010) ISBN 04-701-3148-9.

[33] Friedman, D. J., Lindau, I., and Spicer, W. E., *Noble-Metal CdTe Interface Formation*, Physical Review B. 37(2) (1988), p. 731.

[34] Szeles, C., *CdZnTe and CdTe materials for X-ray and gamma ray radiation detector applications*, Phys. Stat. Sol.(b) 241, No. 3 (2004), p. 783.

[35] Berding, M. A., *Annealing conditions for intrinsic CdTe*, Applied Physics Letters 74 4 (1999), p. 552.

[36] Wei, S.H. and Zhang, S. B., *Chemical trends of defect formation and doping limit in II-VI semiconductors: The case of CdTe*, Physical Review B. 66 15 (2002), p. 155211.

[37] Neumark, G.F., *Defects in wide band gap II-VI crystals*, Mater. Sci. Eng. R21 (1997), p. 1.

[38] Allachen, K., Tapiero, M., Guellil, Z., Zielinger, J. P. and Launay, J. C., *Photoconductivity studies in vanadium-doped CdTe and* $Cd_{1-x}Zn_xTe$, Journal of Crystal Growth 185 (1998), p. 1142.

[39] Hage-Ali, M. and Siffert, P., *Growth Methods of CdTe Nuclear Detector Materials, in Semiconductors for room temperature nuclear detector applications*, ed. T.E. Schlesinger and R.B. James (Academic Press: New York) Vol. 43 (1995), p. 219.

[40] Franc, J., Fielderle, M., Babentsov, V., Fauler, A., Benz, K. W. and James, R. B., *Defect structure of Sn-doped CdTe*, Journal of Electronic Materials 32 7 (2003), p. 772.

[41] Neumark, G. F., *Are Impurities the Cause of Self-Compensation in Large-Band-Gap Semiconductors*, Journal of Applied Physics 51 6 (1980), p. 3383.

[42] Elhadidy, H., *Development of room temperature CdTe gamma ray detectors for security and medical applications: Doctoral thesis*, Institute of Physics of Charles University, Prague 2008.

[43] Babentsov, V., Corregidor, V., Castaño, J. L., Fiederle, M., Feltgen, T., Benz, K.W. and Diéguez, E., *Compensation of CdTe by Doping With Gallium*, Crystal Research and Technology 36 (6) (2001), p. 535.

[44] Shcherbak, L., Feichouk, P., Fochouk, P. and Panchouk, O., *Self-compensation studies in Cd-saturated In-doped CdTe*, Journal of Crystal Growth 161 1-4 (1996), p. 219.

[45] Hofmann, D. M., Omling, P., Grimmeiss, H. G. Meyer, B. K., Benz, K. W. and Sinerius, D., *Identification of the Chlorine-A center in CdTe*, Physical Review B. 45 11 (1992), p. 6247.

[46] Francou, J. M., Saminadayar, K. and Pautrat, J. L., *Shallow Donors in CdTe*, Physical Review B. 41 17 (1990), p. 12035.

[47] Stadler, W., Hofmann, D. M., Meyer, B. K., Krauserehberg, R., Polity, A., Abgarjan, T., Salk, M., Benz, K. W. and Azoulay, M., *Compensation Models in Chlorine Doped CdTe Based on Position Annihilation and Photoluminescence Spectroscopy*, Acta Physica Polonica A. 88 5 (1995), p. 921.

[48] Tovstyuk, K. D., Deybuk, V. G., Melnichuk, S. V. and Tovstyuk, N. K., *3d-Impurity Levels in CdTe and ZnSe*, Physica Status Solidi B-Basic Research 130 2 (1985), p. K153.

[49] Molva, E., Saminadayar, K., Pautrat, J. L. and Ligeon, E., *Photo-Luminescence Studies in N, P, Arsenic Implanted Cadmium Telluride*, Solid State Communications. 48 11 (1983), p. 955.

[50] Molva, E., Pautrat, J. L., Saminadayar, K., Milchberg, G. and Magnea, N., *Acceptor States in CdTe and Comparison with ZnTe - General Trends*, Physical Review B. 30 6 (1984), p. 3344.

[51] Castaldini, A., Cavallini, A., Fraboni, B., Fernandez, P., and Piqueras, J., *Deep energy levels in CdTe and CdZnTe*, J. Appl. Phys. 83 (1998), p. 2121.

[52] Soundararajan, R., Lynn, K. G., Awadallah, S., Szeles, C. and Wei, S. H., *Study of defect levels in CdTe using thermoelectric effect spectroscopy*, Journal of Electronic Materials 35 6 (2006), p. 1333.

[53] Babii, P. I., Slynko, V. V., Gnatenko, Y. P., Bukivskii, P. N., Ilashchuk, M. I. and Parfenyuk, O. A., *Isoelectronic Substitutional Sc and Ti Impurities in CdTe*, Soviet Physics Semiconductors-USSR 24 8 (1990), p. 904.

[54] Molva, E., Chamonal, J. P. and Pautrat, J. L., *Shallow Acceptors in Cadmium Telluride*, Physica Status Solidi B-Basic Research 109 2 (1982), p. 635.

[55] Sarem, A., Orlowski, B. A. and Kuzminski, S., *Surface Photovoltage Spectroscopy of* $Cd_{0.97}Fe_{0.03}Se$ *and* $Cd_{0.97}Fe_{0.03}Te$ *Crystals*, Acta Physica Polonica A. 79 2-3 (1991), p. 183.

[56] Moravec, P., Hage-Ali, M., Chibani, L. and Siffert, P., *Deep Levels in Semiinsulating CdTe*, Materials Science and Engineering B-Solid State Materials for Advanced Technology. 16 1-3 (1993), p. 223.

[57] Huang, Z. C., Eissler, E. and Wie, C. R., *Role of Cadmium Vacancy-Related Defects in CdTe Nuclear-Detectors*, Nuclear Instruments & Methods in Physics Research Section B-Beam Interactions with Materials and Atoms. 100 4 (1995), p. 507.

[58] Isett, L. C. and Raychaudhuri, P. K., *Deep Levels in N-CdTe*, Journal of Applied Physics. 55 10 (1984), p. 3605.

[59] Ye, C. P. and Chen, J. H., *Studies of Defects in N-Type CdTe by Charge Transient Spectroscopy*, Journal of Applied Physics 67 5 (1990), p. 2475.

[60] Ido, T., Heurtel, A., Triboulet, R. and Marfaing, Y., *Deep Level Structure and Compensation Mechanism in in-Doped CdTe Crystals*, Journal of Physics and Chemistry of Solids 48 9 (1987), p. 781.

[61] Debbag, F., Bastide, G. and Rouzeyre, M., *Thermal Ionization and Photoionisation Properties of Deep Traps in N-Type CdTe*, Solid State Communications. 67 1 (1988), p. 1.

[62] Jantsch, W., G. Brunthaler and Hendorfer, G., *Constant photo-EPR: A new method for DEEP level charachterization*, Materials Science Forum. 10-12 (1986), p. 515.

[63] Toney, J. E., Brunett, B. A., Schlesinger, T. E., Cross, E., Doty, F. P. and James, R. B. *Optical and Electrical Characterization of Copper- and Chlorine-Doped Cadmium Zinc Telluride*, Proceedings of Material Research Society 487 (1998), p. 59.

[64] Fiederle, M., Ebling, D., Eiche, C., Hofmann, D. M., Salk, M., Stadler, W., Benz, K. W., and Meyer, B. K., *Comparison of CdTe,* $Cd_{0.9}Zn_{0.1}Te$ *and* $CdTe_{0.9}Se_{0.1}$ *Crystals - Application for Gamma-Ray and X-Ray-Detectors*, Journal of Crystal Growth 138 1-4 (1994), p. 529.

[65] Szeles, C., Shan, Y. Y., Lynn, K. G. and Moodenbaugh, A.R., *Trapping properties of cadmium vacancies in* $Cd_{1-x}Zn_xTe$, Physical Review B. 55 11 (1997), p. 6945.

[66] Chang, Y. C. and James, R. B., *Theoretical studies of Cd vacancies and vacancychlorine complexes in CdTe and* $Cd_{1-x}Zn_xTe$, Proceedings of SPIE 3768 (1999), p. 381.

[67] Krsmanovic, N., Hunt, A. W., Lynn, K. G., Flint, P. J. and Glass, H. L., *Studies of deep trapping levels in undoped and Sn-doped Cd1-xZnxTe by thermoelectric effect spectroscopy and thermally stimulated current*, Proceedings of SPIE 4141 (2000), p. 11.

[68] Christmann, P., Meyer, B. K., Kreissl, J., Schwarz, R. and Benz, K.W., *Vanadium in CdTe: An electron-paramagnetic-resonance study*, Physical Review B. 53 7 (1996), p. 3634.

[69] Krsmanovic, N., Lynn, K. G., Weber, M. H., Tjossem, R., Gessmann, T., Szeles, C., Eissler, E. E., Flint, J. P. and Glass, H. L., *Electrical compensation in CdTe and* $Cd_{0.9}Zn_{0.1}Te$ *by intrinsic defects*, Physical Review B. 62 24 (2000), p. R16279.

[70] Caldas, M. J., Fazzio, A. and Zunger, A., *A Universal Trend in the Binding-Energies of Deep Impurities in Semiconductors*, Applied Physics Letters 45 6 (1984), p. 671.

[71] Zerrai, A. and Bremond, G., *Properties of the titanium related level in* $Cd_{0.96}Zn_{0.04}Te$ *crystals*, Journal of Applied Physics 84 10 (1998), p. 5554.

[72] Kremer, R. E. and Leigh, W. B., *Deep Levels in CdTe*, Journal of Crystal Growth 86 1-4 (1988), p. 490.

[73] Zerrai, A., Marrakchi, G. and Bremond, G., *Electrical and optical characteristics of deep levels in vanadium-doped* $Cd_{0.96}Zn_{0.04}Te$ *materials by photoinduced current, capacitance and photocapacitance transient spectroscopies*, Journal of Applied Physics 87 9 (2000), p. 4293.

[74] Hendorfer, G., Brunthaler, G., Jantsch, W., Reisinger, J. and Sitter H., *Photo-EPR and DLTS of CdTe-Co*, Journal of Crystal Growth 86 1-4 (1988), p. 497.

[75] Franc, J., Grill, R., Kubát, J., Hlídek, P., Belas, E., Moravec, P. and Höschl, P., *Influence of space charge on lux-ampere characteristics of high-resistivity CdTe*, Journal of Electronic Materials 35 5 (2006), p. 988.

[76] Godlewski, M. and Baranowski, J. M., *Electron-Paramagnetic-Res Measurements of Chromium Impurity Photo-Ionization Transitions in CdTe*, Physica Status Solidi B-Basic Research 97 1 (1980), p. 281.

[77] Corbel, C., Baroux, L., Kiessling, F. M., Gelysykes, C. and Triboulet, R., *Positron Trapping at Native Vacancies in CdTe Crystals - in Doping Effect*, Materials Science and Engineering B-Solid State Materials for Advanced Technology 16 1-3 (1993), p. 134.

[78] Lischka, K., Brunthaler, G. and Jantsch, W., *Deep Donor Levels Due to Isolated Fe in CdTe*, Journal of Crystal Growth 72 1-2 (1985), p. 355.

[79] De Antonis, P., Morton, E. J. and Podd, F. J. W., *Infra-red microscopy of Cd(Zn)Te radiation detectors revealing their internal electric field structure under bias*, IEEE Trans. Nucl. Sci. 43 (1996), p. 1487.

[80] Zumbiehl, A., Hage-Ali, M., Fourgeres, P., Koebel, J. M., Regal, R., Siffert, P. *Electric field distribution in CdTe and* $Cd_{1-x}Zn_x$ *Te nuclear detectors*, J. Cryst. Growth 197 (1999), p. 650.

[81] Khusainov, K., Antonova, Y. A., Lysenlko, V. V., Makhkamov, R. K., Morozov, V. Z., Ilves, A. G. and Arlt, R. D. *Energy resolution of large-area CdTe p-i-n detectors with charge loss corrections*, Nucl. Instrum. Method. Phys. Res. A. 458 (2001), p. 242.

[82] Cola, A., Farella, I., Auricchio, N. and Caroli, E., *Investigation of the electric field distribution in X-ray detectors by Pockels effect*, J. Opt. A Pure Appl. Opt. 8 (2006), p. 467.

[83] Hall, R. N., *Electron-Hole Recombination in Germanium*, Phys. Rev. 87 (1952), p. 387.

[84] Shockley, W. and Read, W. T., *Statistics of the Recombinations of Holes and Electrons*, Phys. Rev. 87 (1952), p. 835.

[85] Sachtler, W. M. H., Dorgelo, G. J. H. and Holscher A. A., *The work function of gold*, Surf. Sci. 5 2 (1966), p. 221.

[86] Franc, J., James, R. B., Grill, R., Dědič, V., Belas, E., Praus, P., Prekas, G. and Sellin, P. J., *Influence of Contacts on Electric Field in an Au/(CdZn)Te/Au Detector: A Simulation*, IEEE Trans. Nucl. Sci. 57 (2010), p. 2349.

[87] Saleh, B. E. A., *Fundamentals of photonics*, 2nd ed. New York: John Wiley, 1991, xviii, 966 p. ISBN 04-718-3965-5.

[88] Bylsma, R. B., Bridenbaugh, P. R., Olson, D. H., and Glass, A. M., *Photorefractive properties of doped cadmium telluride*, Appl. Phys. Lett. 51 2 (1987), p. 889.

[89] Hlídek, P., Bok, J., Franc, J. and Grill, R., *Refractive index of CdTe: Spectral and temperature dependence*, J. Appl. Phys. 90 (2001), p. 1672.

[90] Malý, P., *Optika*, Prague: Karolinum, 2008, 361 p. ISBN 978-80-246-1342-0.

[91] Narasimhamurty, T. S., *Photoelastic and Electro-optic Properties of Crystals*, New York: Plenum Press, 1981. ISBN 978-147-5700-275.

[92] Namba, S., *Electro-Optical Effect of Zincblende*, J. Opt. Soc. Am. 51 1 (1961), p. 76.

[93] Marfaing, Y., *Carrier effective masses in CdTe, CdZnTe and CdTeSe*, in Properties of Narrow-Gap Cadmium-Based Compounds, P. Capper, Ed. London: INSPEC (1994), p. 537.

[94] Malm, H., L., Martini, M., *Polarization phenomena in CdTe nuclear radiation detectors*, IEEE Trans. Nucl. Sci. 21 (1974), p. 322.

[95] Siffert, P., Berger, J., Scharager, C., Cornet, A., Stuck, R., Bell R., O., Serreze, H. B. and Wald, F., V., *Polarization in cadmium telluride nuclear radiation detectors*, IEEE Trans. Nucl. Sci. 23 (1976), p. 159.

[96] Principato, F., Gerardi, G., Turturici, A. A. and Abbene, L., *Time-dependent current-voltage characteristics of Al/p-CdTe/Pt x-ray detectors*, Journal of Applied Physics 112 9 (2012), p. 094506.

[97] Elhadidy, H., Šikula, J. and Franc, J., *Symmetrical current–voltage characteristic of a metal–semiconductor–metal structure of Schottky contacts and parameter retrieval of a CdTe structure*, Semicond. Sci. Technol. 27 (2012), p. 015006.

[98] Joshi, N., *Photoconductivity: art, science, and technology*, New York: M. Dekker, c1990, x, 309 p. Optical engineering (Marcel Dekker, Inc.), v. 25. ISBN 08-247-8321-2.

[99] Hurtes Ch, Boulou, M. and Bois D, *Deep-level spectroscopy in high-resistivity materials*, Appl. Phys. Lett. 32 (1978), p. 821.

[100] Li, Z., *Systematic modeling and comparisons of capacitance and current based microscopic defect analysis techniques for measurements of high-resistivity silicon detectors after irradiation*, Nucl. Instr. and Meth. in Phys. Res. A. 403 (1998), p. 399.

[101] Fink, J., Kruger, H., Lodomez, P. and Wermes, N., *Characterization of charge collection in CdTe and CZT using the transient current technique*, Nucl. Inst. and Meth. 560 2 (2006), p. 435.

[102] Uxa, Š., Belas, E., Grill, R., Praus, P. and James, R. B., *Determination of electric-field profile in CdTe and CdZnTe detectors using transient-current technique*, IEEE Trans. Nucl. Sci. 59 (2012), p. 2402.

[103] Franc, J., Hlídek, P., Moravec, P., Belas, E., Höschl, P., Turjanska, L. and Varghova, R., *Determination of energy gap in* $Cd_{1-x}Zn_xTe$ ($x = 0 - 0.06$), Semicond. Sci. Technol. 15 (2000), p. 561.

[104] Elhadidy, H., Dědič, V., Franc, J. and Grill, R., *Study of polarization phenomena in n-type CdZnTe*, J. Phys. D: Appl. Phys. 47 (2014), p. 055104.

[105] Kubát, J., Elhadidy, H., Franc, J., Grill, R., Belas, E., Höschl, P. and Praus, P., *Evaluation of the Concentration of Deep Levels in Semi-Insulating CdTe by Photoconductivity and TEES*, IEEE Trans. Nucl. Sci. 56 (2009), p. 1706.

[106] Franc, J., Elhadidy, H., Babentsov, V., Fauler, A. and Fiederle, M., *Comparative study of vertical gradient freeze grown CdTe with variable Sn concentration*, J. of Materials Research. 21 (4) (2006), p. 1025.

[107] Franc, J., Hlídek, P., Belas, E., Kubát, J., Elhadidy, H. and Fesh, R., *Deep-level photoluminescence in semi-insulating CdTe(In) and CdTe(Sn)*, Nucl. Instrum. Methods Phys. Res. A. 591 (2008), p. 196.

[108] Siffert, P. M., Berger, J., Scharager, C., Cornet, A., Stuck, R., Bell, R.O., Serreze, H.B. and Wald, F.V., *Polarization in cadmium telluride nuclear radiation detectors*, IEEE Trans. Nucl. Sci. 23 (1976), p. 159.

[109] Dědič, V., Franc, J., Sellin, P. J., Grill, R., and Perumal, V., *Study on electric field in Au/CdZnTe/In detectors under high fluxes of X-ray and laser irradiation*, Journal of Instrumentation 7 (2012), p. 02011.

[110] Franc, J., Dědič, V., Zázvorka, J., Hakl, M., Grill, R. and Sellin, P. J. *Flux-dependent electric field changes in semi-insulating CdZnTe*, J. Phys. D: Appl. Phys. 46 (2013), p. 235306.

[111] Echeverria R., Vincent A. B. and Joshi N. V., *Photoquenching effect and its consequence in p type gallium arsenide*, Solid State Commun. 52 (1984), p. 901.

[112] Sellin, P. J., Davies, A. W., Lohstroh, A., Özsan, M. E. and Parkin, J., *Drift mobility and mobility-lifetime products in CdTe:Cl grown by the travelling heater method*, IEEE Trans. Nucl. Sci. 52 (2005), p. 3074.

[113] Dědič, V., Franc, J., Elhadidy, H., Grill, R., Belas, E., Moravec, P., Zázvorka, J. and Höschl, P., *Study of deep levels in high resistivity CdZnTe by discharge current measurement*, Journal of Instrumentation 8 (2013), p. 01008.

[114] Grill, R., Franc, J., Elhadidy, H., Belas, E., Uxa, Š., Bugár, M., Moravec, P. and Höschl, P., *Theory of Deep Level Spectroscopy in Semi-Insulating CdTe*, IEEE Trans. Nucl. Sci. 59 5 (2012), p. 2383.

[115] Hage-Ali, M. and Siffert, P., *Status of semi-insulating cadmium telluride for nuclear radiation detectors*, Nucl. Inst. and Methods in Phys. Res. A. 322 (1992), p. 313.

[116] Castaldini A., Cavallini A., Fraboni B., Fernandez P. and Piqueras J., *Midgap traps related to compensation processes in CdTe alloys*, Phys. Rev. B. 56 (1997), p. 14897.

[117] Cavallini A., Fraboni B. and Dusi W., *Compensation processes in CdTe-based compounds*, IEEE Symp. Conf. Record Nucl. Sci. 7 (2004), p. 4247.

[118] Kim, K. H., Choi, J. H., Bolotnikov, A.E., Camarda, G. S., Hossain, A., Yang, G., Cui, Y. and James, R.B., *New insight into the 1.1-eV trap level in CdTe-based semiconductor*, J. Korean Physical Society 62 (2013), p. 623.

[119] Mohr, P. J., Taylor, B. N. and Newell, D.B., *CODATA Recommended Values of the Fundamental Physical Constants: 2010*, J. Phys. Chem. Ref. Data 41, (2012), p. 043109.

Appendix

A.1 List of tables

1.1 Several material properties of CdZnTe and CdTe 3
1.2 Several semiconductor material properties at 300 K 5
1.3 Overview of energy levels in (CdZn)Te 7

2.1 Indices reduction in r_{ijk} 22

3.1 Description and conditions of measured intensity distributions... 36
3.2 List of measured samples. 45

6.1 Summary of energy levels 88

A.2 List of figures

1.1 Absorption coefficient α of CdTe 3
1.2 Three levels compensation model 7

2.1 The scheme of energy band structure used in the HSR model. 10
2.2 Band scheme of the M-S interface of CdZnTe/Au 13
2.3 Absorption of the incident radiation 15
2.4 Two cases of the light penetration in a biased sample 16
2.5 Illustration of processes in the sample after irradiation 16
2.6 Scheme of a planar detector sample 17
2.7 Typical distribution of the electric field within a polarized detector 19
2.8 Sample acting as dynamic wave retarder 20
2.9 Rotational index ellipsoid 25
2.10 Spatial arrangement of vectors **E**, **a** and **k** 27
2.11 Schematics of the direction of the linearly polarized light 27

3.1 Experimental setup for Pockels effect measurements 32
3.2 Sample holder 33
3.3 Transmission spectrum of bandpass filter 34
3.4 `X-Control` program window 34
3.5 Linearity of the sensitivity of InGaAs camera 35
3.6 Advanced setup 1 36
3.7 Advanced setup 2 36
3.8 Outline of data analysis 37
3.9 Dependence of the transmittance of the biased sample 39

3.10 Calculated electric field . . . 39
3.11 Photocurrent spectrum . . . 40
3.12 Schematics of the measuring circuit . . . 41
3.13 Experimental setup used for discharge current measurements . . . 43
3.14 Discharge current measurements . . . 43
3.15 Planar sample configuration . . . 44
3.16 IR images of the samples . . . 45

4.1 Time evolution of the electric field . . . 49
4.2 Electric field distribution through Au/CdTe/In sample, cathode: Au . . . 49
4.3 Electric field distribution through Au/CdTe/In sample, cathode: In . . . 50
4.4 Linearity of averaged electric field distributions . . . 51
4.5 IR images acquired by InGaAs camera . . . 51
4.6 Temperature dependence of the steady state electric field . . . 52
4.7 Profile of the space charge . . . 53
4.8 Temperature evolution of the total charge . . . 53
4.9 Experimental data of the time evolution of the electric field . . . 54
4.10 Evaluation of time constants τ_1 and τ_2 . . . 54
4.11 Arrhenius plot . . . 55
4.12 Scheme of emission of electrons from the deep level . . . 55
4.13 Distribution of the electric field with time . . . 56
4.14 Time evolution of the space charge at the cathode . . . 57
4.15 Time evolution of the electric field calculated at the cathode . . . 58
4.16 Arrhenius plot of the de-trapping time . . . 58
4.17 Time evolution of the electric field calculated just below the cathode . . . 59
4.18 Plot of the electric field versus $\sqrt{U}$ . . . 60
4.19 Time evolution of the current transient . . . 61
4.20 Time stability of the electric field (sample no.3) . . . 61
4.21 Electric field through the samples with a different resistivity . . . 62
4.22 Electric field distribution through the sample under X-ray irradiation . . . 63
4.23 Electric field distribution through the sample under laser irradiation . . . 64
4.24 Band diagram of Au/CdTe/In structure with work functions Φ . . . 65
4.25 The results of the simulation (electric field) . . . 65
4.26 The results of the simulation (space charge) . . . 66
4.27 Internal processes . . . 66
4.28 Electric field dependence on different photon fluxes (798 nm) . . . 67
4.29 Electric field dependence on different X-ray tube current . . . 68
4.30 Measured photoconductivity spectrum . . . 69
4.31 Measured lux-Ampere characteristics . . . 69
4.32 Numeric simulations of lux-Ampere characteristics . . . 70
4.33 Electric field dependence on different photon fluxes (754 nm) . . . 71
4.34 Electric field dependence on different excitation wavelengths . . . 71
4.35 Numerical simulation of the electric field and space charge . . . 72
4.36 Simulation of the distribution of trapping time and filling factor . . . 73
4.37 Principle of IR spectral scanning of the laser-excited sample . . . 74
4.38 Profile of the electric field. Red laser + IR spectral scanning . . . 75
4.39 Profile of the electric field. Infrared laser + IR spectral scanning . . . 76
4.40 Dependence of electric field on illumination at position $x = 2.3$mm . . . 77
4.41 Scheme of energy levels in CdZnTe . . . 77

4.42 Electric field profile under 1.96eV laser illumination with IR spectral scanning . . 79
4.43 Spectral dependence of the electric field on IR scanning 79
4.44 Electric field profile under 1.31eV laser illumination with IR spectral scanning . . 81
4.45 Spectral dependence of the electric field on IR scanning 81
4.46 Scheme of energy levels in CdZnTe 81

5.1 Band diagram of the sample no.5 83
5.2 Arrhenius plot. Sample no.5 83
5.3 Band diagram of the samples no.3 & 4 84
5.4 Arrhenius plot. Sample no.3 85
5.5 Arrhenius plot. Sample no.4 85
5.6 Arrhenius plot - weak and strong re-trapping 86

6.1 Summary of energy levels 89

A.3 List of abbreviations

A.3.1 Physical constants

This is a list of physical constants used in this thesis (according to [119]).

Symbol	**Name**	**Value**
e	elementary charge	$1.602\ 176\ 565(35) \times 10^{-19}$ C
ϵ_0	vacuum permittivity	$8.854\ 187\ 817 \times 10^{-12}$ $\mathrm{F \cdot m^{-1}}$
h	Planck constant	$6.626\ 069\ 57(29) \times 10^{-34}$ $\mathrm{J \cdot s}$
k_B	Boltzmann constant	$1.380\ \ 6488(13) \times 10^{-23}$ $\mathrm{J \cdot K^{-1}}$
m_e	electron mass	$9.109\ 382\ 91(40) \times 10^{-31}$ kg

A.3.2 Physical quantities and other symbols

This is a list of the most frequently used symbols. Other symbols that appear only once (chap. 1 and 2) are specified in corresponding paragraphs.

Latin symbols

Symbol	**Name**	**Unit**
A	area	mm^2
$\mathbf{a} = [a_1, a_2, a_3]$	polarization vector	
CCE	charge collection efficiency	
(CdZn)Te	CdTe and/or CdZnTe	
CZT	CdZnTe	
d	sample thickness	mm

Symbol	Name	Unit
E	photon energy	eV
E_A	activation energy	eV
E_c	conduction band energy	eV
E_f	Fermi level energy	eV
E_t	deep level energy	eV
E_v	valence band energy	eV
E_{vac}	vacuum level energy	eV
$\mathcal{E}$	electric field intensity	$\mathrm{V \cdot cm^{-1}}$
$\mathbf{E} = [\mathcal{E}_1, \mathcal{E}_2, \mathcal{E}_3]$	vector of electric field intensity	$\mathrm{V \cdot cm^{-1}}$
$\mathcal{G}$	carriers generation rate	$\mathrm{cm^{-3} \cdot s^{-1}}$
I	electric current	A
I_{pc}	photocurrent	A
IR	infrared	A
$\mathbf{j} = [j_1, j_2, j_3]$	vector of electric current density	$\mathrm{A \cdot cm^2}$
j_{pc}	photocurrent density	$\mathrm{A \cdot cm^2}$
$\mathbf{k} = [k_1, k_2, k_3]$	wave vector	$\mathrm{m^{-1}}$
L	optical path length (sample width)	mm
L_d	depletion width	mm
$m^*_{e(h)}$	effective mass of electrons (holes)	m_e
$\mathfrak{n}$	refractive index	
n	concentration of free electrons	$\mathrm{cm^{-3}}$
$N_{c(v)}$	effective density of states of electrons (holes)	$\mathrm{cm^{-3}}$
n_t	concentration of electrons at deep level	$\mathrm{cm^{-3}}$
N_t	total deep level concentration	$\mathrm{cm^{-3}}$
NIR	near infrared	
p	concentration of free holes	$\mathrm{cm^{-3}}$
p_t	concentration of holes at deep level	$\mathrm{cm^{-3}}$
Q	electric charge	C
r	Pockels (electrooptic) coefficient	$\mathrm{m \cdot V^{-1}}$
$\mathbf{r}$	directional vector	m
$\mathcal{R}$	carrier recombination rate	$\mathrm{cm^{-3} \cdot s^{-1}}$
R	resistance	Ω
t	time	s

Symbol	Name	Unit
T	temperature	K
$\mathcal{T}$	transmittance	
U	voltage	V
v_{th}^{e}	thermal velocity of electrons	m·s^{-1}
v_{th}^{h}	thermal velocity of holes	m·s^{-1}
Z	atomic number	

Greek symbols

Symbol	Name	Unit
α	absorption coefficient	cm^{-1}
α_i	direction cosine	
α_P	sample parameter (see eq.2.57)	
$\varGamma$	wave phase shift	
$\epsilon = \epsilon_r \epsilon_0$	permittivity	F · m^{-1}
ϵ_r	relative permittivity	
η	dielectric impermeability	
λ	wavelength	nm
$\mu_{n(p)}$	electron (hole) mobility	cm^{2}·V^{-1}·s^{-1}
ν	photon frequency	s^{-1}
ρ	resistivity	Ω·cm
ϱ	space charge density	C·m^{-3}
σ_n	electron capture cross-section	cm^{2}
σ_p	hole capture cross-section	cm^{2}
$\tau_{e(h)}$	electron (hole) de-trapping time	s
$\tau_{n(p)}$	electron (hole) life time	s
φ	electric potential	V
$\varPhi$	photon flux	cm^{-2}·s^{-1}
$\varPhi_{Cd(Zn)Te}, \varPhi_{Au}, \varPhi_{In}$	work function of Cd(Zn)Te, Au and In	eV